UNSUPERVISED MULTI-SCALE CHANGE DETECTION FROM SAR IMAGERY FOR MONITORING NATURAL AND ANTHROPOGENIC DISASTERS

By

Olaniyi A. Ajadi, B.Sc., M.Sc.

A Dissertation Submitted in Partial Fulfillment of the Requirements
for the Degree of

Doctor of Philosophy
In
Geophysics

University of Alaska Fairbanks
August 2017

APPROVED:

Dr. Franz Meyer, Committee Chair
Dr. Peter Webley, Committee Member
Dr. Carl Tape, Committee Member
Dr. Catherine Cahill, Committee Member
Dr. Paul McCarthy, Chair
Department of Geosciences
Dr. Paul Layer, Dean
College of Natural Science and Mathematics
Dr. Michael Castellini, Dean of the Graduate School

Abstract

Radar remote sensing can play a critical role in operational monitoring of natural and anthropogenic disasters. Despite its all-weather capabilities, and its high performance in mapping, and monitoring of change, the application of radar remote sensing in operational monitoring activities has been limited. This has largely been due to: (1) the historically high costs associated with obtaining radar data; (2) slow data processing, and delivery procedures; and (3) the limited temporal sampling that was provided by spaceborne radar-based satellites. Recent advances in the capabilities of spaceborne Synthetic Aperture Radar (SAR) sensors have developed an environment that now allows for SAR to make significant contributions to disaster monitoring. New SAR processing strategies that can take full advantage of these new sensor capabilities are currently being developed.

Hence, with this PhD dissertation, I aim to: (i) investigate unsupervised change detection techniques that can reliably extract signatures from time series of SAR images, and provide the necessary flexibility for application to a variety of natural, and anthropogenic hazard situations; (ii) investigate effective methods to reduce the effects of speckle and other noise on change detection performance; (iii) automate change detection algorithms using probabilistic Bayesian inferencing; and (iv) ensure that the developed technology is applicable to current, and future SAR sensors to maximize temporal sampling of a hazardous event. This is achieved by developing new algorithms that rely on image amplitude information only, the sole image parameter that is available for every single SAR acquisition.

The motivation and implementation of the change detection concept are described in detail in Chapter 3. In the same chapter, I demonstrated the technique's performance using synthetic data as well as a real-data application to map wildfire progression. I applied Radiometric Terrain

Correction (RTC) to the data to increase the sampling frequency, while the developed multiscale-driven approach reliably identified changes embedded in largely stationary background scenes. With this technique, I was able to identify the extent of burn scars with high accuracy.

I further applied the application of the change detection technology to oil spill mapping. The analysis highlights that the approach described in Chapter 3 can be applied to this drastically different change detection problem with only little modification. While the core of the change detection technique remained unchanged, I made modifications to the pre-processing step to enable change detection from scenes of continuously varying background. I introduced the Lipschitz regularity (LR) transformation as a technique to normalize the typically dynamic ocean surface, facilitating high performance oil spill detection independent of environmental conditions during image acquisition. For instance, I showed that LR processing reduces the sensitivity of change detection performance to variations in surface winds, which is a known limitation in oil spill detection from SAR.

Finally, I applied the change detection technique to aufeis flood mapping along the Sagavanirktok River. Due to the complex nature of aufeis flooded areas, I substituted the resolution-preserving speckle filter used in Chapter 3 with curvelet filters. In addition to validating the performance of the change detection results, I also provide evidence of the wealth of information that can be extracted about aufeis flooding events once a time series of change detection information was extracted from SAR imagery.

A summary of the developed change detection techniques is conducted and suggested future work is presented in Chapter 6.

Table of Contents

Page

List of Figures

Page

List of Tables

Page

Acknowledgements

I give all glory to God Almighty, father of wisdom, and knowledge. I wish to express my sincere appreciation to my supervisor Dr. Franz Meyer, for his guidance, support, encouragement, valuable discussions, and thorough comments. He has been the most influential person in my PhD study, and a source of inspiration. I am forever grateful for all the time, hard work, and energy he has put into securing me a strong financial support throughout my PhD. Also, I express my greatest gratitude to him for all the career opportunities through many conferences. Thank you for being a positive influence in my life.

My gratitude to my committee members, Dr. Carl Tape, Dr. Peter Webley, and Dr. Catherine Cahill, knows no bounds. I thank them for their patience, and effort in providing me the knowledge during my voyage at the Geophysical Institute. I would like to thank Dr. Sang-Ho Yun for offering me an internship at the NASA Jet Propulsion Laboratory (JPL). I truly appreciate your work ethics, energy, and support throughout my time at JPL. I would like to thank Pete Hickman for all his assistance, Dr. Marivi Tello for research collaboration, and Dr. Catherine Hanks for the career opportunities through the Imperial Barrel Program.

I would like to thank my colleagues (David McAlpin, Heming Liao, Oliver Dammann, Wenyu Gong, and Alex Sacco) in the Geophysical Institute for their help, support, and understanding. I would like to thank my close friends Nilesh Dixit, Ibrahim Ilhan, and Celso Alvizuri for all the fun memories in Alaska. This dissertation will not be complete without appreciating Ibukun Okubanjo, and Rotimi Okubanjo for all the fun adventures, and good memories. You guys made my time in Alaska go by fast.

Lastly my deepest gratitude goes to my parents, the rest of my family, and the Okubanjo's for their unconditional love, encouragement, and support over the years.

Chapter 1 Introduction

The focus of this dissertation is to develop an amplitude-based change detection technique that is applicable to any incoming Synthetic Aperture Radar (SAR) dataset, while preserving the geometric details in an image, and is easily transferable for monitoring, and mapping the extent of disasters of different types, including flooding, oil spills, wildfires, and more. For purposes of this dissertation, we define disasters as extreme events that occur on the Earth's surface, and that threaten human life or health, cause environmental damage, and/or incur significant economic harm. We also consider disasters that result from natural causes or anthropogenic activities.

For the past decade, the impact of disasters on the global environment has increased, causing global economic damage (Gelsdorf, 2011). It is therefore necessary to monitor disasters, and provide near real-time information about their development, and progression (Lillesand et al., 2014). In order to manage disasters efficiently, a disaster management flowchart made up of two stages is often followed (Figure 1.1) (Bello and Aina, 2014). The first stage consists of disaster prevention and preparedness, which takes place before a disaster occurs. Disaster prevention involves infrastructure improvement and disaster assessments, while disaster preparedness involves community outreach, emergency response plans, as well as training and exercises (Bello and Aina, 2014). The second stage consists of disaster response, rehabilitation, and recovery, which takes place after a disaster has occurred. Disaster response includes evacuation, property preservation, emergency relief, and lifesaving, while disaster rehabilitation and recovery involves debris management, health services support, and economic recovery (Bello and Aina, 2014). The work presented in this dissertation mostly is in support of this second stage of disaster management.

Data acquired from spaceborne sensors have undergone numerous developments (e.g. increase in spatial, spectral, radiometric, and temporal resolution) to the extent where they provide key observations required to understand, monitor, and gain insight on disasters from the local to the global scale. Nowadays, the availability of satellite images covering a crisis situation have increased substantially due to high temporal resolution compared to what we used to have years ago. Data derived from satellite images have been used over the past decade by decision makers during natural disasters for disaster preparedness, and warning (McEntire, 2014). A wide range of optical and microwave sensors have proven useful in monitoring a disaster. Both of these sensor types are sensitive to different changes in an area of interest as a result of their different imaging characteristics (Dekker, 1998).

Passive optical sensors measure the amount of reflected or emitted light energy in the visual, near-infrared, and infrared part of the spectrum, and can be used to characterize the Earth surface and its change. Popular optical sensors and sensor systems used in disaster management include the medium-resolution United States Geological Survey (USGS) Land Remote-Sensing Satellite (LandSAT), Systeme Pour l'Observation de la Terre (SPOT), and European Space Agency (ESA) Sentinel-2 systems, as well as the high-resolution sensors from Digital Globe, which include IKONOS, Quickbird, and Worldview. Optical satellite imagery has successfully been used to monitor a range of natural disasters (Ahtonen et al., 2004; Brakenridge and Anderson, 2006; Lillesand et al., 2014; Van der Sande et al., 2003). Optical sensors are often preferred for mapping natural disasters when available, because of their easy interpretability (Martinis, 2010). However, they are limited due their sensitivity to cloud cover, and their dependence on solar illumination, making them less suitable for use in rapid monitoring (Tello Alonso, 2011).

SAR data have increasingly been preferred to optical sensor data for monitoring disasters (Lillesand et al., 2014; McEntire, 2014; Tello Alonso, 2011). In 1978, the first civilian SAR, Seasat, sensor was launched by the National Aeronautics and Space Administration (Barrick and Swift, 1980). Seasat successfully demonstrated the capabilities of SAR for providing weather- and solar illumination-independent images of the Earth surface over its three-month operational phase and generated extensive interest in SAR as an effective tool for Earth observation (Walter, 1990). Therefore, several SAR missions were prepared and launched in the subsequent years, including the ESA Environmental Remote Sensing (ERS) satellites, ERS-1 and -2, the Environmental Satellite (Envisat), and the Canadian-launched and Canadian Space Agency (CSA) operated Radar Satellite (RADARSAT). More recently, a range of SAR-based satellites with high-resolution capabilities (between 3 m to 18 m spatial resolution, and between 10 to 24 days' temporal resolution) were developed, and launched successfully. Examples includes the Advanced Land Observation Satellite (ALOS) Phased-Array L-band SAR (PALSAR) by JAXA, RADARSAT-2 by CSA, TerraSAR-X by the German Aerospace Center, as well as Sentinel-1A and B by ESA.

In contrast to passive optical systems, SAR sensors offer various advantages related to the active nature of the sensor, and to the use of microwave frequencies. They are characterized by all-weather acquisition capabilities, and can operate regardless of smoke or cloud cover, or solar illumination. Moreover, modern SAR sensors provide high spatial resolution data across large swaths (e.g. 100 km by 150 km), rivalling the capabilities of passive optical sensors. However, the interpretation of SAR images for monitoring applications is often not an easy task. For example, SAR images are mostly acquired at oblique angles giving rise to geometric distortions that make the interpretation of SAR images less straightforward (Ajadi et al., 2016; Dekker,

1998). Also, SAR data is subject to speckle noise, giving the images a grainy complexion, and making the extraction of information from SAR images more difficult (Lillesand et al., 2014).

In remote sensing applications, SAR images have been very useful for change detection studies (Chen et al., 2012; Wulder et al., 2006). Change detection is described as the process of classifying differences that occurred in the state of an object between two images acquired over the same geographical area but at different acquisition dates (Lu et al., 2004; Singh, 1989).

In the past, researchers have made various contributions to the development of methods that identify changes in multi-temporal SAR data. These methods are usually classified into two groups: bi-temporal change detection, and image time series change detection, as stated in Cui and Datcu (2012). Change detection can be performed in two ways, namely unsupervised (Bruzzone and Prieto, 2000), and supervised (Huo et al., 2010). In unsupervised change detection, a change map is generated by comparing objects in two images with a similarity metric. The change map then undergoes thresholding to classify each pixel into changed, and unchanged classes (Bruzzone and Prieto, 2000; Otsu, 1975). In supervised change detection, training samples are selected from the available dataset, and are used to train a classifier, which is then used to classify an image into changed, and unchanged classes (Huo et al., 2010).

With the increasing availability of multiple SAR sensors, and multi-temporal SAR remote sensing datasets, this thesis develops an unsupervised automatic change detection technique that is highly flexible in monitoring disasters. The technique uses a pre-processing step to increase the sampling frequency, and correct for terrain undulations. A resolution-preserving speckle filter was used to preserve the geometric details in the image whilst suppressing the noise. A multi-scale framework was used to decompose an image into different resolution levels. The different resolution levels allow the algorithm to analyze an image with different signal to noise ratios. To

automate the classification operations required in the multi-scale change detection approach, a probabilistic Bayesian inferencing, with expectation maximization (EM) algorithm, was employed. Finally, measurement level fusion was used to fuse the probability maps generated from each decomposed image. It is worth stating that, for different change detection situations, the core of the change detection technique stays the same but the pre-processing step is modified.

In this dissertation, the motivation, concept, and details of the proposed change detection method are extensively described. To demonstrate its flexibility, and performance, the proposed technique is applied to three different disaster scenarios that pose different challenges to change detection techniques. These analyze hazard applications include fire scar mapping, oil spill detection, and flood tracking. It will be shown that the change detection approach can be applied to all of these diverse situations with only slight adaptions to the workflow.

Fire scar mapping is important for monitoring the hazards associated with wildfire progression, determining ecological impacts of a burn, assessing the effects of fires on natural resources, and studying the variability in fire regimes over time (Joyce et al., 2009). The specific challenges associated with fire scar mapping from SAR imagery include the development of a robust method that can reliably delineate fire scars across a range of diverse landscapes; the complex scattering response of SAR; and the high level of speckle noise contained.

Oil spill detection is important in giving an early warning of oil pollution that could lead to environmental hazards (Brekke and Solberg, 2005). Detecting oil spills early can help decision makers manage the pollution event properly (Krohling and Campanharo, 2011). Identifying oil spills reliably using SAR images is challenging due to the inhomogeneous properties of the sea surface, making it difficult to discriminate between oil spills, low-wind areas, and look-alikes.

We have developed a technique to mitigate this issue by applying Lipschitz Regularity (Tello et al., 2007) to the data, and adding it to the change detection algorithm.

With the increase in global warming, flood tracking is of great importance (Hirabayashi et al., 2013). Locating, and tracking floods helps to assess the risk it poses on infrastructure and human life. Flood tracking also helps civil protection officials in effective, and accurate decision making in prioritizing aid efforts (Pulvirenti et al., 2011). The challenges associated with flood mapping include the development of a method that is easily transferable to different geographical conditions, free of prior assumptions, and accomplished automatically without setting manual thresholds.

This dissertation is structured as follows: Chapter 2 provides an overview of the basics of SAR with a focus on system geometry, and data acquisition principles. System, and object properties influencing SAR backscatter are also discussed. A summary of the interactions of microwave signals with water surface, and freshwater ice is also given. In Chapter 3 the motivation, concepts, and implementation details of the developed change detection concept are extensively described along with an application of the developed technique to fire scar mapping highlighting its performance, and capabilities for these hazard events. Chapter 4 presents an application of the developed data analysis concept to the mapping of oil spills. Adaptions to the change detection workflow that were implemented to address challenges associated with the dynamic nature of ocean surfaces are described. To evaluate the performance of the developed technique extensive cross-comparisons with other state-of-the-art techniques are presented. Chapter 5 showcases an application of the change detection concept to the mapping of aufeis floods on the North Slope of Alaska. In addition to showing the performance of the method, this chapter also shows the amount of information that can be extracted from SAR data to study the

nature, and progression of this flood event. Chapter 6 gives a concluding evaluation of the proposed methods and summarizes a set of suggested future investigations. The manuscripts presented in this dissertation was written and revised by Olaniyi Ajadi with contributions from all coauthors. All authors have read and approved the final manuscripts.

1.1. References

Ahtonen, P., Euro, M., Hallikainen, M., Solbø, S., Johansen, B.,, and Solheim, I., 2004, SAR and optical based algorithms for estimation of water bodies: Technical report, FloodMan Project.

Ajadi, O. A., Meyer, F. J., and Webley, P. W., 2016, Change Detection in Synthetic Aperture Radar Images Using a Multiscale-Driven Approach: Remote Sensing, v. 8, no. 6, p. 482.

Barrick, D. E., and Swift, C. T., 1980, The Seasat microwave instruments in historical perspective: IEEE Journal of Oceanic Engineering, v. 5, no. 2, p. 74-79.

Bello, O. M., and Aina, Y. A., 2014, Satellite remote sensing as a tool in disaster management and sustainable development: towards a synergistic approach: Procedia-Social and Behavioral Sciences, v. 120, p. 365-373.

Brakenridge, R., and Anderson, E., 2006, MODIS-based flood detection, mapping and measurement: the potential for operational hydrological applications, Transboundary floods: reducing risks through flood management, Springer, p. 1-12.

Brekke, C., and Solberg, A. H., 2005, Oil spill detection by satellite remote sensing: Remote Sensing of Environment, v. 95, no. 1, p. 1-13.

Bruzzone, L., and Prieto, D. F., 2000, Automatic analysis of the difference image for unsupervised change detection: IEEE Transactions on Geoscience and Remote Sensing, v. 38, no. 3, p. 1171-1182.

Chen, G., Hay, G. J., Carvalho, L. M., and Wulder, M. A., 2012, Object-based change detection: International Journal of Remote Sensing, v. 33, no. 14, p. 4434-4457.

Cui, S., and Datcu, M., 2012, Statistical wavelet subband modeling for multi-temporal SAR change detection: IEEE Journal of Selected Topics in Applied Earth Observations and Remote Sensing, v. 5, no. 4, p. 1095-1109.

Dekker, R., 1998, Speckle filtering in satellite SAR change detection imagery: International Journal of Remote Sensing, v. 19, no. 6, p. 1133-1146.

Gelsdorf, K., 2011, Global challenges and their impact on international humanitarian action, Office for the Coordination of Humanitarian Affairs (OCHA).

Hirabayashi, Y., Mahendran, R., Koirala, S., Konoshima, L., Yamazaki, D., Watanabe, S., Kim, H., and Kanae, S., 2013, Global flood risk under climate change: Nature Climate Change, v. 3, no. 9, p. 816-821.

Huo, C., Zhou, Z., Lu, H., Pan, C., and Chen, K., 2010, Fast object-level change detection for VHR images: IEEE Geoscience and Remote Sensing Letters, v. 7, no. 1, p. 118-122.

Joyce, K. E., Belliss, S. E., Samsonov, S. V., McNeill, S. J., and Glassey, P. J., 2009, A review of the status of satellite remote sensing and image processing techniques for mapping natural hazards and disasters: Progress in Physical Geography, v. 33, no. 2, p. 183-207.

Krohling, R. A., and Campanharo, V. C., 2011, Fuzzy TOPSIS for group decision making: A observation for accidents with oil spill in the sea: Expert Systems with Applications, v. 38, no. 4, p. 4190-4197.

Lillesand, T., Kiefer, R. W., and Chipman, J., 2014, Remote sensing and image interpretation, John Wiley & Sons.

Lu, D., Mausel, P., Brondizio, E., and Moran, E., 2004, Change detection techniques: International Journal of Remote Sensing, v. 25, no. 12, p. 2365-2401.

Martinis, S., 2010, Automatic near real-time flood detection in high resolution X-band synthetic aperture radar satellite data using context-based classification on irregular graphs (Doctoral dissertation, Ludwig-Maximilians-University of Munich).

McEntire, D. A., 2014, Disaster response and recovery: Strategies and tactics for resilience, John Wiley & Sons.

Otsu, N., 1975, A threshold selection method from gray-level histograms: Automatica, v. 11, no. 285-296, p. 23-27.

Pulvirenti, L., Pierdicca, N., Chini, M., and Guerriero, L., 2011, An algorithm for operational flood mapping from Synthetic Aperture Radar (SAR) data using fuzzy logic: Natural Hazards and Earth System Sciences, v. 11, no. 2, p. 529.

Singh, A., 1989, Review article digital change detection techniques using remotely-sensed data: International Journal of Remote Sensing, v. 10, no. 6, p. 989-1003.

Tello Alonso, M. V., 2011, Post-processing methods for ocean monitoring in SAR images (Doctoral dissertation, Universitat Politècnica de Catalunya).

Tello, M., Lopez-Martinez, C., Mallorqui, J. J., Danisi, A., Di Martino, G., Iodice, A., Ruello, G., and Riccio, D., 2007, Characterization of local regularity in SAR imagery by means of multiscale techniques: application to oil spill detection, *in* Proceedings Geoscience and Remote Sensing Symposium. IGARSS 2007. IEEE International, p. 5228-5231.

Van der Sande, C., De Jong, S., and De Roo, A., 2003, A segmentation and classification approach of IKONOS-2 imagery for land cover mapping to assist flood risk and flood damage assessment: International Journal of Applied Earth Observation and Geoinformation, v. 4, no. 3, p. 217-229.

Walter, L. S., 1990, The uses of satellite technology in disaster management: Disasters, v. 14, no. 1, p. 20-35.

Wulder, M. A., White, J. C., and Coops, N. C., 2006, Identifying and Describing Forest Disturbance and Spatial Pattern, Understanding Forest Disturbance and Spatial Pattern: Remote Sensing and GIS Approaches, CRC Press, p. 31-61.

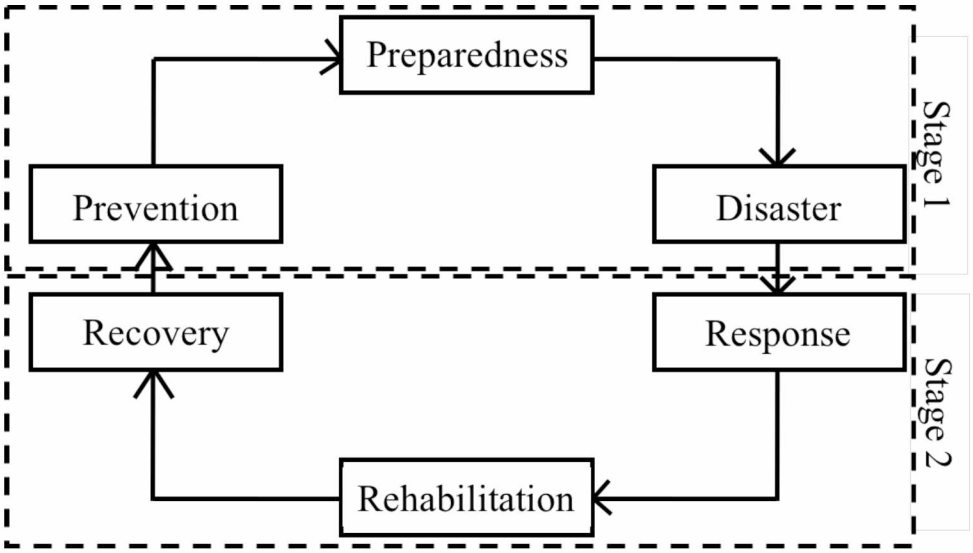

Figure 1.1. Disaster management workflow (Bello and Aina, 2014).

Chapter 2 Characteristic of Radar Imagery

This Chapter is intended to provide the reference material needed for the subsequent Chapters and is not written as a complete reference of all fundamentals of radar and SAR remote sensing. First, a brief summary of the SAR data acquisition concept is provided. Subsequently, geometric distortions typically encountered in SAR images as well as the radiometric properties of SAR acquisitions are explained. Finally, factors influencing SAR backscatter and the interaction of SAR transmitted signal with different surfaces are shown. It is worth mentioning that, for the sake of this dissertation, InSAR and polarimetric properties will not be discussed because they are less relevant as reference material for the research presented in this dissertation.

2.1. Properties and Basic Principles of Radar Imaging Systems

2.1.1. Basics of Data Acquisition

Imaging radar systems typically operate in a side-looking geometry, and sense an area of interest by transmitting pulses of microwave energy at the rate of the pulse repetition frequency (PRF). Radar echoes backscattered from the illuminated area are recorded by the radar receiver (Bamler and Schättler, 1993). When a radar sensor moves along its orbital path, the ground area it illuminates is called the antenna footprint, S, and the strip being imaged is called the swath (Bamler and Schättler, 1993). The look angle, θ_l, is the angle from nadir to the sensor line of site, while the incidence angle, θ_i, is the angle between the line of sight and the normal to the local reference surface (Woodhouse, 2005). From Figure 2.1, the sensor's direction of travel is the along track or azimuth direction, and the two-way travel time of the microwave pulses is measured in range or the across track direction (Woodhouse, 2005). According to Bamler and

Schättler (1993), imaging radar systems provide a two-dimensional representation of the Earth's surface and are operated in a number of radar band wavelengths (Table 1).

2.1.2. Range Resolution

A radar system is described by its resolution in range (across-track) and azimuth (along-track) direction. In range direction, from the near-range to the far-range edge of the swath, echoes from the ground arrive progressively later, and objects at different ranges can be distinguished if their range separation is larger than half the transmitted pulse length. Hence, the range resolution is defined by

$$r_{sr} = \frac{c\tau}{2} \tag{2.1}$$

The projection of r_{sr} on the ground is the ground range resolution, (r_{gr}). Hence, r_{gr} varies inversely with the sine of the incidence angle, θ_i, and increases as the slant range distance increases (Raney, 1998):

$$r_{gr} = \frac{r_{sr}}{sin\theta_i} \tag{2.2}$$

To achieve a higher resolution, the pulse duration must be short enough so that travel times of the backscatter signal differ from one another by at least $\frac{\tau}{2}$. This can be hard to achieve, however, because the short pulse also results in a low signal-to-noise ratio (SNR) at the receiver. In other words, the resolution gain made by shortening the pulse duration reduces the amount of transmitted signal power, and, hence, degrades the SNR compared to that achievable with longer pulse durations. Maximizing resolution is therefore achieved by replacing short bursts at a constant frequency with a frequency-coded signal pulse (a so-called chirp), compressed into the equivalent short pulse using a matched filtering approach (Woodhouse, 2005). This process is

known as range compression. In modern radar systems, the range resolution achieved by a chirped pulse is therefore inversely related to the bandwidth of the pulse, W_p, such that:

$$r_{sr} = \frac{c}{2W_p} \tag{2.3}$$

Following Equation 2.3, high range resolution, and high SNR are usually achieved in modern radars because they are transmitting longer linear frequency modulated (chirped) pulses of high bandwidth instead of narrow pulses. The implementation of a range compression step is therefore standard on imaging radar systems, and it results in the formation of a high-resolution image.

2.1.3. Azimuth Resolution

As the radar system transmits a sequence of short microwave pulses, an area on the ground is illuminated that is often referred to as the antenna footprint, S. In the along-track (azimuth) direction, the size of this footprint is generally defined by the relationship between the wavelength, λ, of the system, and the side length of the antenna, L (defining the antenna's beamwidth through $= \frac{\lambda}{L}$) along this direction, as well as by the distance of the radar sensor from the ground, D. As the ground is scanned, the ability to separate two adjacent targets in the along-track direction is referred to as the azimuth resolution.

For real aperture radars (RARs), the azimuth resolution depends on the width of the antenna footprint in azimuth direction, and is limited by the side length of the antenna in the azimuth direction. To achieve high resolution in the along-track direction with RAR systems, a large antenna has to be used. As the antenna beam spreads out with increasing distance between the object on the ground, and the sensor, the azimuth resolution for RARs is given as (Woodhouse, 2005):

$$r_{ar,RAR} = \frac{D\lambda}{L} \tag{2.4}$$

In Equation 2.4, the azimuth resolution ($r_{ar,RAR}$) degrades linearly as the distance of the radar sensor from the ground, D, increases. For example, an antenna with a length of 3.2 km, a distance of 310 km to a ground target, and a microwave sensor with a wavelength of 3.1 cm will achieve an azimuth resolution of about 3 m.

High resolution can also be attained with short antennas by using the Synthetic Aperture Radar (SAR) approach. High azimuth resolution with SAR systems is achieved by coherently recording the scattered signal echoes from a small antenna over the distance of the sensor's flight path, then combining them to synthesize the effect of a very long antenna (Woodhouse, 2005). The azimuth resolution for a SAR is giving as:

$$r_{a,SAR} = \frac{L}{2} \tag{2.5}$$

2.2. Geometric Distortions in SAR Images

In side-looking viewing geometries, sensor-facing slopes appear foreshortened such that a symmetric mountain would appear as if "leaning" towards the sensor. The geometric background of foreshortening is shown in the first panel of Figure 2.2a, showing that the slope between points A, and B will get foreshortened into the image area $A'B'$. The amount of foreshortening depends both on the system's look angle, θ_l, and on the slope angle, α, and reaches its maximum if, $\theta_l \rightarrow \alpha$. In areas where $\theta_l < \alpha$ (e.g., in areas of steep slopes combined with steep incidence angles), foreshortening turns into layover (see center panel of Figure 2.2b). In layover situations, the tops of mountains are imaged ahead of their base (see projections of points B and C in Figure 2.2b), and backscatter from mountain slopes will overlay with image information at closer, and further image ranges (see green, red, and gray areas in Figure 2.2b). Both foreshortening, and

layover can be reduced if the look angle, θ_l, is increased, however, larger θ_l will produce more image shadow (Figure 2.2c). Hence, topography-related image distortions cannot be entirely removed, and image acquisitions from more than one vantage point may be necessary to jointly minimize all three imaging effects.

2.3. Speckle effect on SAR Images

In the SAR imaging process, the total backscattered signal from a distributed target is the coherent sum of all N randomly distributed individual scatterers contained within an image resolution cell (Woodhouse, 2005). Speckle is found in all coherent imaging systems as a result of interference among the coherent echoes of these N randomly individual scatterers (Woodhouse, 2005). Speckle in a SAR image increases with signal intensity. It affects the image spatial details, reduces radiometric resolution, and hinders automatic processing (Figure 2.3). To reduce the noise-like effect of speckle, speckle filters are often used during processing (Ajadi et al., 2016).

2.4. Radar Equation and Radar Cross Section

The goal of every imaging radar system is to enable high-resolution imaging of the surface while maintaining sufficient SNR of the recorded data. To illustrate the challenges behind this goal, it is worth calculating how much return energy P_r can be expected if a signal of power p_t and wavelength λ is transmitted to the ground at distance R using an antenna of area A.

To calculate the amount of energy that is hitting a target at distance R, we consider a signal of power p_t that is transmitted through an antenna of size A. The antenna is focusing the transmitted power into a narrow range of spatial angles achieving a (unitless) so-called "antenna gain" G corresponding to

$$G = \frac{4\pi . A}{\lambda^2}. \tag{2.6}$$

The transmitted energy $p_t . G$ disperses spherically as it travels down to the ground according to $\frac{1}{4\pi . R^2}$ such that the power density that hits a ground target corresponds to

$$P_g = \frac{p_t . G}{4\pi . R^2}. \tag{2.7}$$

Only a part of the incoming power P_g is scattered back into the direction of the radar and received by the antenna. The fraction of the incoming power that is backscattered toward the sensor is defined by the object's *radar cross section* σ such that the backscatter power corresponds to $P_g . \sigma$. After traveling back to sensor and dispersing along its way (again by $\frac{1}{4\pi . R^2}$), the signal is received back by the antenna such that the received power P_r can be calculated using

$$P_r = A \frac{p_g}{4\pi . R^2} \sigma = A \frac{p_t . G}{4\pi^2 . R^4} \sigma = \frac{G\lambda^2}{4\pi} \frac{p_t . G}{4\pi^2 . R^4} \sigma = P_t \frac{G^2 \lambda^2}{4\pi^3 . R^4} \sigma \tag{2.8}$$

Equation (2.8) is called the *radar equation* and links the backscattered power received at the sensor to the transmit power, the imaging geometry, the radar antenna, and the properties of the surface.

The amount of scattering and the value of σ depends on various parameters. The system specific parameters encompass the frequency and polarization while the object specific properties include roughness and dielectric properties.

2.4.1. System Properties Influencing SAR Backscatter

According to Lillesand et al. (2014), the frequency of the signal determines the penetration depth of the object imaged. Penetration depth tends to be longer with longer wavelengths. When analyzing surface structures, X- and C-band are preferred because of their high frequency

characteristics, and the lower capacity for these wavelengths to penetrate into the subsurface. However, when analyzing structures below the surface with little to no moisture content, L-band is preferred because of the low frequency characteristics of L-band systems, and their associated surface penetration capabilities (Lillesand et al., 2014). Regardless of frequency, radar pulses can be transmitted, and received in different polarization. Most modern SAR systems can transmit radar pulses that oscillate either in a horizontal (H) or a vertical (V) plane (relative to the orientation of the antenna). Similarly, backscattered signals can be received in horizontal, and vertical polarizations, resulting in signals that are observed in like-polarized (HH, VV), and cross-polarized (HV, VH) combinations. As different polarizations interact differently with structures on the Earth surface, the mode of polarization also gives an insight about an object. For example, using like-polarization, the signal can be weakened when depolarization occurs. However, this is the opposite when cross-polarization is used.

Finally, the radar's incidence angle is another important factor affecting the backscatter characteristics of a SAR. The incidence angle affects how the roughness of an object appears in an image and controls the geometric properties of SAR data. A very rough surface, that scatters signal in all directions, will have little dependence on incidence angle, while the backscatter of a moderately rough surface will decrease with increasing incidence angle. A smooth surface on the other hand can have a backscatter brighter than a rough surface at small incidence angles.

2.4.2. Object Properties Influencing SAR Backscatter

For a given wavelength, the amount of backscatter received at the sensor depends, in large part, on the surface roughness, and the dielectric properties of the object.

Surface roughness: Surface roughness is an important factor influencing backscatter signal. In Ulaby et al. (1982), surface roughness decided the angular distribution of surface scattering.

When a surface is smooth (Figure 2.4a), energy is scattered away from the monostatic sensor (specular reflection) and the smooth surface boundary is known as a specular reflector (Lillesand et al., 2014). In addition, the incidence angle, θ_i, is the same as the reflection angle, θ_r. The specular reflection causes smooth surfaces to appear dark in a SAR image (low signal return). When the roughness of a surface starts to increase, the coherent component decreases and the fraction of diffuse scattering increases (Ulaby et al., 1982). This increase in roughness scatters the incidence energy in all directions and a certain amount is transmitted back to the sensor (Figure 2.4b). Moreover, when the surface appears to be very rough, the incidence energy is scattered equally in all directions (Figure 2.4c).

It is worth noting that the roughness of a surface appearing in an image does not only depend on the geometric properties but also on the local incidence angle and the wavelength of the transmitted signal. According to Woodhouse, (2005), the relationship between these parameters is given by Rayleigh criterion, which states that a surface is rough when the following condition holds:

$$\sigma_{rms} > \frac{\lambda}{8 \cos \theta_{local}} \tag{2.9}$$

Also, a more conservative condition for roughness is expressed by the Fraunhofer criterion as:

$$\sigma_{rms} > \frac{\lambda}{32 \cos \theta_{local}} \tag{2.10}$$

where, θ_{local}, is the local incidence angle, and, σ_{rms}, is the root mean square of the surface variations. A surface will appear smooth when λ increases and a surface will appear rough when the phase difference ($\Delta\Phi$) of two reflected waves is greater than $\frac{\pi}{2}$ radians, and $\frac{\pi}{8}$ radians for Rayleigh criterion, and Fraunhofer criterion, respectively.

Dielectric properties: Dielectric properties control whether microwave signals will scatter at the surface or whether (parts of) the signal will penetrate into the medium. They also determine how much of the penetrating energy is transmitted into deeper layers and how much is being absorbed (Raney, 1998). Hence, the dielectric properties govern large parts of the microwave interactions with objects and determine how much backscattered signal can be expected at the sensor. According to Raney, (1998), the relative dielectric constant, ε, which describes a material response to the electric field of an electromagnetic signal, consists of a real, ε', and an imaginary, ε'', part. Both, ε', and, ε'', depend on the signal wavelength, and the moisture content of the target. The permittivity of the material is largely defined by the real part of the dielectric constant, ε', while the imaginary part, ε'', determines losses of signal power through absorption (Ulaby et al., 1982). For example, an object such as metal has a high dielectric constant. A vacuum has a dielectric constant of 1.0, while most natural materials have real dielectric constant between 2 and 10, and imaginary dielectric constant between 0.01 and 0.1 (Ulaby et al., 1982).

2.4.3. Interaction between Microwave Signals and Water Surfaces

In this section, the interaction of SAR signals with waterbodies such as ocean surfaces or rivers is explained. Understanding the interactions of SAR with water surfaces is important to prepare the reader for the research performed in Chapter 4 of this dissertation, where the interaction is mostly governed by surface roughness. Due to the ocean's high dielectric constant, there is little to no penetration into the water, but there is scattering at the water surface. When the ocean surface appears smooth (at the radar's microwave wavelength), then specular reflection is dominant, and low signal power is returned back to the sensor. Hence, smooth water bodies generally appear dark in SAR images. The radar backscatter of the water surface

increases as a consequence of friction between the air and the ocean surface. Wind causes friction to set up an oscillation on the ocean surface, leading to small surface perturbations (ripples) ranging from mm to cm (capillary waves) as well as longer waves with spatial scales between m, and km (gravity waves) on the ocean surface (Lewis et al., 1998). As a result of this, the ocean surface is usually modelled as a combination of these successive waveforms and the range of these waveforms is known as wave spectrum. These successive waveforms also act as a Bragg surface which is responsible for the backscatter energy detected by SAR. The radar backscatter is primarily determined by the Bragg scattering. The Bragg scattering is a coherent scattering mechanism, which scatters the waves in a number of different direction and not just the specular direction (Woodhouse, 2005). The relationship between the wave spectrum and wind is not simple, but as the wind speed increases, the roughness of the ocean surface increases as well and higher backscatter signal is achieved (Lillesand et al., 2014; Tello et al., 2007; Woodhouse, 2005).

2.4.4. Interactions between Microwave Signals and Freshwater Ice

Understanding the interaction of transmitted SAR signals and ice is important to help the reader grasp the research performed and discussions on the results generated in Chapter 5 of this dissertation. As stated earlier, water in its liquid state has a high dielectric constant, and, hence, does not allow microwave signals to penetrate. However, when water is in solid state (ice), the dielectric constant reduces ($\varepsilon' = 3$), and penetration depth increases. For example, for pure ice, a C-band can have a penetration of about 10 m (Meissner and Wentz, 2004; Onstott, 1992; Woodhouse, 2005).

The formation of ice is important, as scattering can occur from the upper surface of an ice layer, from within the ice layer, or from the boundary between the ice layer, and the underlying

surface (Woodhouse, 2005). This process can be best described from examining shallow river aufeis in the North Slope of Alaska that is gradually freezing over (See Figure 5.12). Ideally, when water in its liquid state starts to cool, it becomes thick, and it sinks to the bottom (Jeffries et al.,1994; Woodhouse, 2005). However, in Northern Alaska, where the atmospheric temperature is cold, water at above freezing temperatures is less dense, and the ice on the surface tends to have two smooth boundaries. The first boundary is formed at the bottom of the ice cover with the liquid water surface and the second boundary is at the top of the ice cover with surrounding air (Jeffries et al.,1994). The boundary between the ice and the liquid water will result in specular reflection because it appears as smooth. As the liquid water continues to freeze over, progressing all the way to the bottom of the lake, the boundary changes from a smooth surface to a rough surface due to the interaction between ice and soil. As a result of the ice growth progress, radar backscatter varies.

2.5. References

Ajadi, O. A., Meyer, F. J., and Webley, P. W., 2016, Change Detection in Synthetic Aperture Radar Images Using a Multiscale-Driven Approach: Remote Sensing, v. 8, no. 6, p. 482.

Bamler, R., and Schättler, B., 1993, SAR data acquisition and image formation, Wichmann-Verlag, p. 53-102.

Jeffries, M., Morris, K., Weeks, W., and Wakabayashi, H., 1994, Structural and stratigraphie features and ERS 1 synthetic aperture radar backscatter characteristics of ice growing on shallow lakes in NW Alaska, winter 1991–1992: Journal of Geophysical Research: Oceans, v. 99, no. C11, p. 22459-22471.

Lewis, A. J., Henderson, F. M., and Holcomb, D., 1998, Radar fundamentals: the geoscience perspective: Principals and Applications of Imaging Radar. John Wiley and Sons, New York, p. 131-181.

Lillesand, T., Kiefer, R. W., and Chipman, J., 2014, Remote sensing and image interpretation, John Wiley & Sons.

Meissner, T., and Wentz, F. J., 2004, The complex dielectric constant of pure and sea water from microwave satellite observations: IEEE Transactions on Geoscience and Remote Sensing, v. 42, no. 9, p. 1836-1849.

Onstott, R. G., 1992, SAR and scatterometer signatures of sea ice: Microwave Remote Sensing of Sea Ice, p. 73-104.

Raney, R. K., 1998, Radar fundamentals: technical perspective: Principles and Applications of Imaging Radar, v. 2, p. 9-130.

Tello, M., Lopez-Martinez, C., Mallorqui, J. J., Danisi, A., Di Martino, G., Iodice, A., Ruello, G., and Riccio, D., 2007, Characterization of local regularity in SAR imagery by means of multiscale techniques: application to oil spill detection, *in* Proceedings Geoscience and Remote Sensing Symposium. IGARSS 2007. IEEE International, p. 5228-5231.

Ulaby, F. T., Moore, R. K., and Fung, A. K., 1982, Microwave Remote Sensing Active and Passive-Volume II: Radar Remote Sensing and Surface Scattering and Enission Theory. Research supported by NASA, NSF, and U.S. Department of Defense. Reading, MA, Addison-Wesley Publishing Co., 1982, p. 624.

Woodhouse, I. H., 2005, Introduction to microwave remote sensing, CRC press.

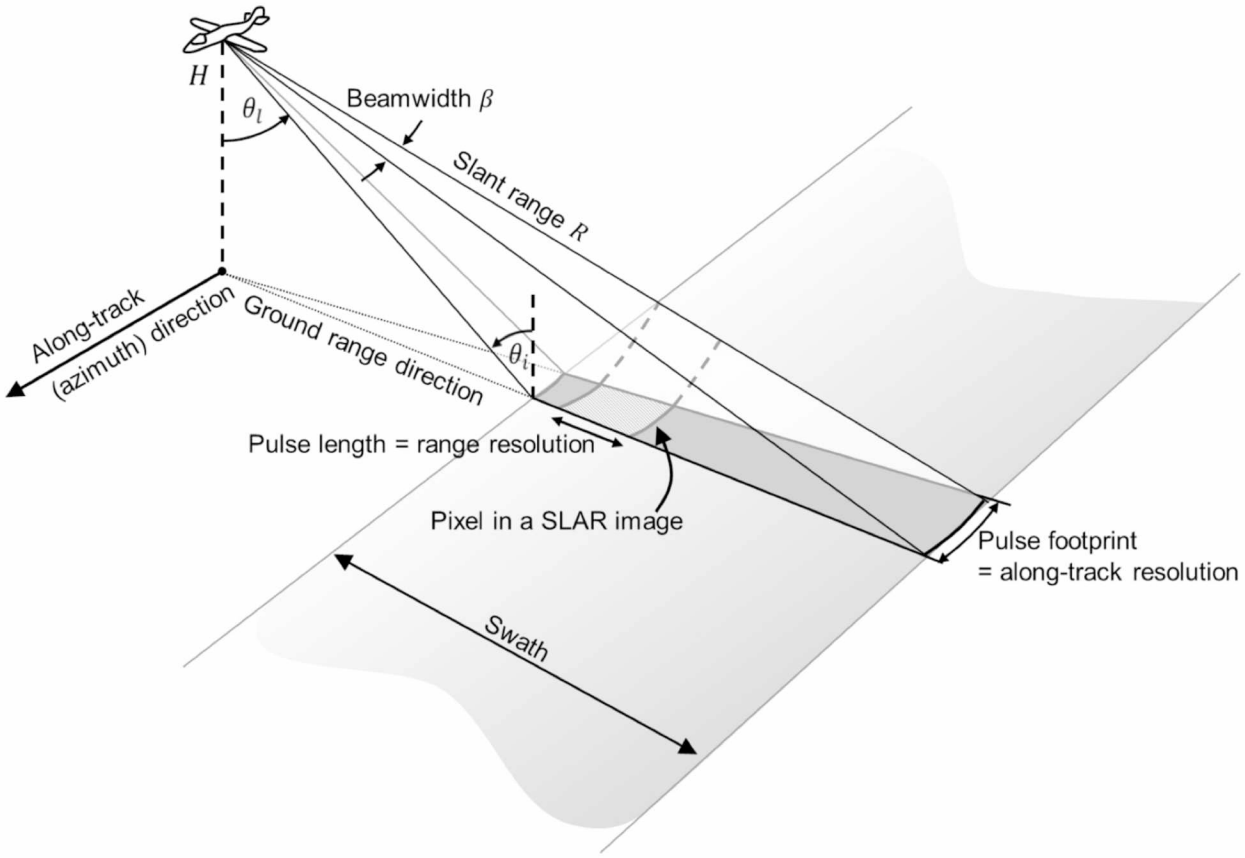

Figure 2.1. Observation geometry of a side-looking airborne radar (SLAR) imager generation of an image is facilitated by the forward motion of the airborne platform. Courtesy: FJ Meyer, UAF.

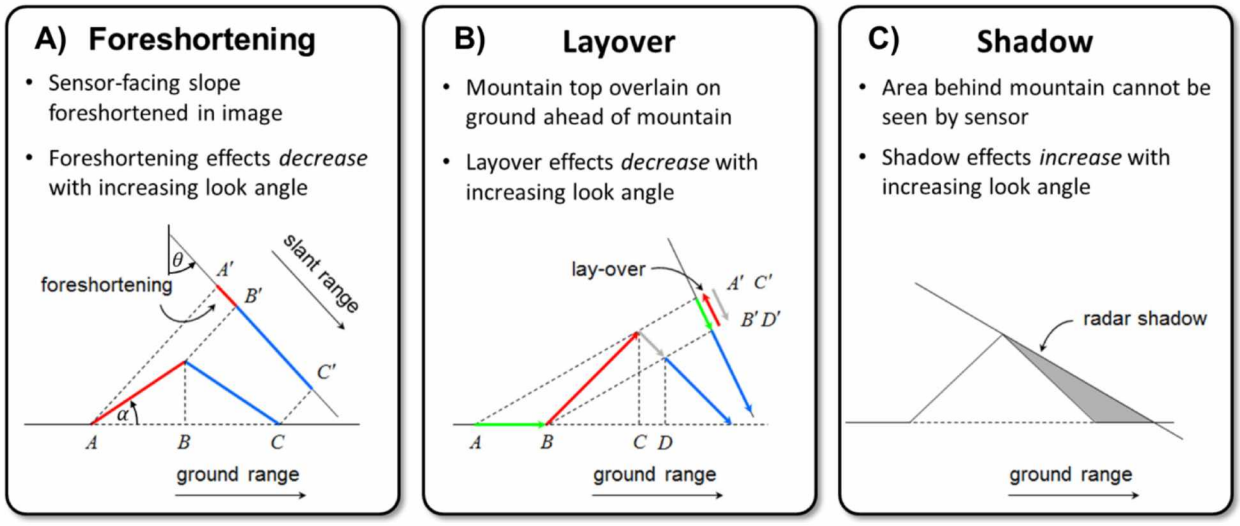

Figure 2.2. Geometric effects of SAR images with their dependence on acquisition geometry. A) Foreshortening; B) Layover; and C) shadow effects. Courtesy: FJ Meyer, UAF.

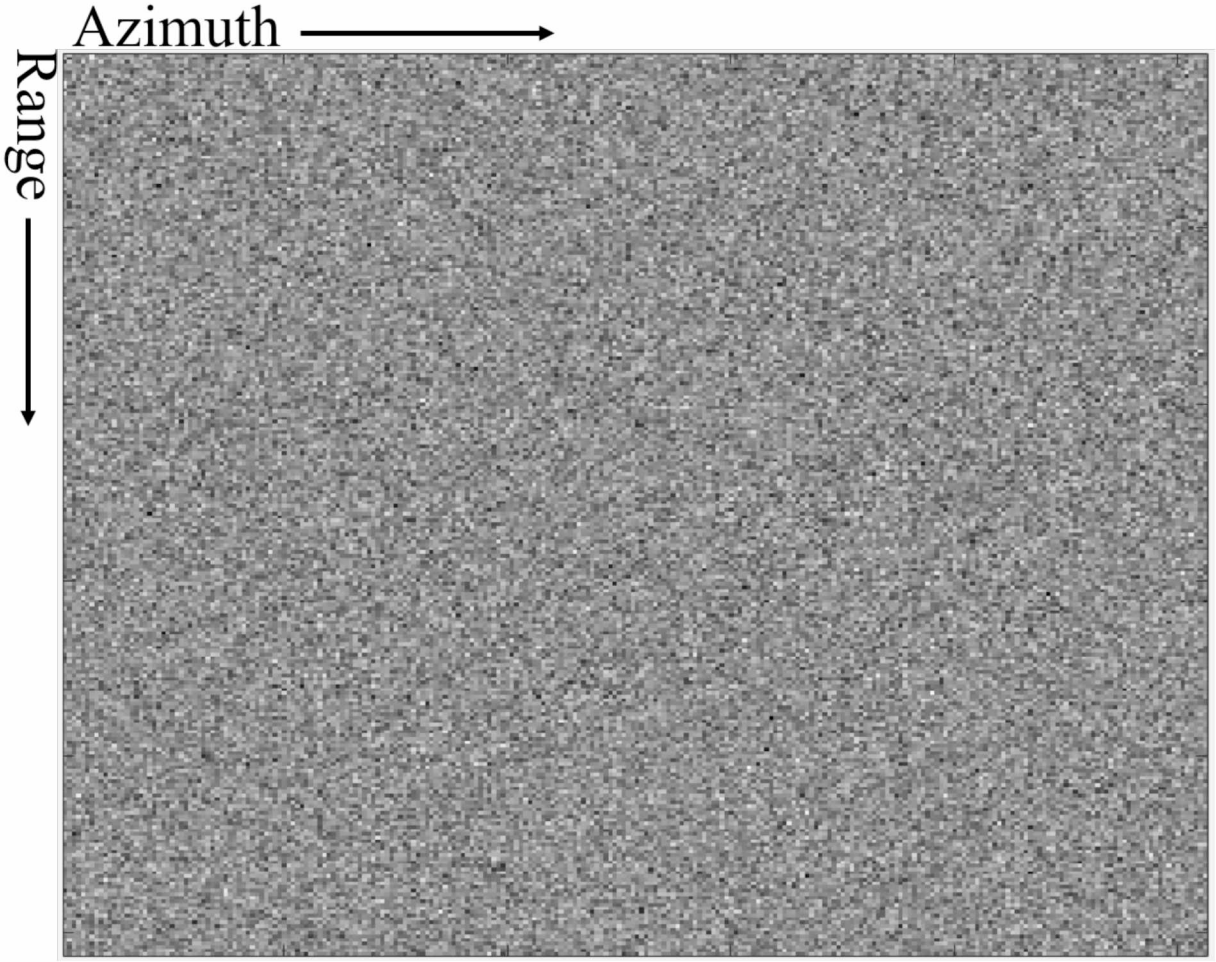

Figure 2.3. Example of Speckle noise in a SAR image

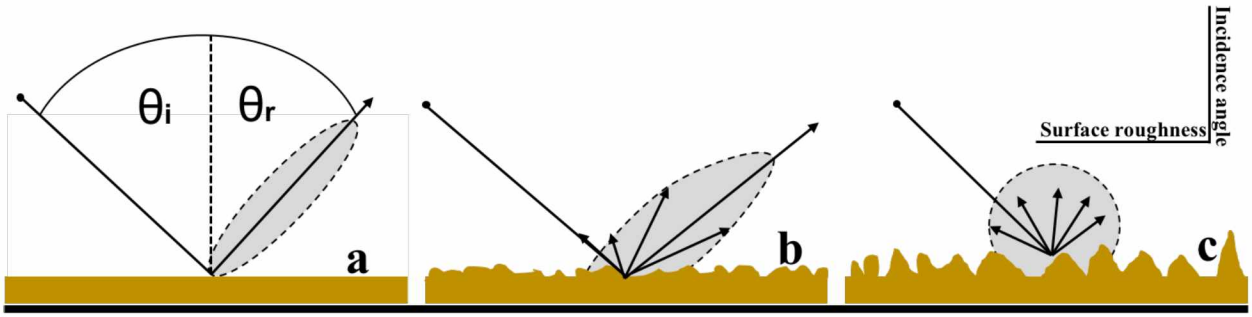

Figure 2.4. Surface roughness and incidence angle define the scattered field. Radar reflection of a) smooth, b) moderately roughened and c) strongly roughened surfaces (Woodhouse, 2005).

Table 2.1. Wavelength bands of imaging radar systems.

Band	**P**	**UHF**	**L**	**S**	**C**	**X**	**Ku**	**Ka**	**Q**
Wavelength	0.75 - 100 m	70.6 - 49.18 cm	24 - 21.74 cm	11.1 - 7.69 cm	5.6 - 5.43 cm	3.2 - 3.19 cm	1.8 cm	1.5 cm	0.75 cm

Chapter 3 Change Detection in Synthetic Aperture Radar Images Using a Multiscale-Driven Approach [1]

3.1. Abstract

Despite the significant progress that was achieved throughout the recent years, to this day, automatic change detection and classification from synthetic aperture radar (SAR) images remains a difficult task. This is, in large part, due to (a) the high level of speckle noise that is inherent to SAR data; (b) the complex scattering response of SAR even for rather homogeneous targets; (c) the low temporal sampling that is often achieved with SAR systems, since sequential images do not always have the same radar geometry (incident angle, orbit path, *etc.*); and (d) the typically limited performance of SAR in delineating the exact boundary of changed regions. With this paper, we present a promising change detection method that utilizes SAR images and provides solutions for these previously mentioned difficulties. We will show that the presented approach enables automatic and high-performance change detection across a wide range of spatial scales (resolution levels). The developed method follows a three-step approach of (i) initial pre-processing; (ii) data enhancement/filtering; and (iii) wavelet-based, multi-scale change detection. The stand-alone property of our approach is the high flexibility in applying the change detection approach to a wide range of change detection problems. The performance of the developed approach is demonstrated using synthetic data as well as a real-data application to wildfire progression near Fairbanks, Alaska.

---

[1] Ajadi, O.A.; Meyer, F.J.; Webley, P.W. Change detection in synthetic aperture radar images using a multiscale-driven approach. Remote Sensing 2016, 8, 482.

3.2. Introduction and Background

Multi-temporal images acquired by optical (Bruzzone and Prieto, 2000) or radar remote sensing sensors (Tello Alonso et al., 2011) are routinely applied to the detection of changes on the Earth's surface. As both of these two sensor types have their own imaging and sensitivity characteristics, their performance in change detection varies with the properties of the changing surface features (Dekker, 1998). In recent years, synthetic aperture radar (SAR) data have gained increasing importance in change detection applications, because SAR is an active sensor, operating without regard to weather, smoke, cloud cover, or daylight (Meyer et al., 2014). So SAR has shown to be a valuable data source for the detection of changes related to river ice breakup (Floyd et al., 2014), earthquake damage (Yun et al., 2012), oil spill detection (Tello et al., 2007), flood (D'Addabbo et al., 2016), and forest growth assessment (Siegert and Hoffmann, 2000).

In this paper, we are interested in developing an unsupervised change detection method from series of SAR images. Despite extensive research that was dedicated to this topic throughout the last decade (Tello et al., 2007), automation and robust change detection from a series of SAR images remains difficult for the following reasons: (A) Due to the complicated nature of the surface backscatter response in SAR data, most SAR-based change detection methods require repeated acquisitions from near-identical vantage points. These repeated acquisitions provide a static background against which surface change can be identified with reasonable performance (Loew and Mauser, 2007). This requirement severely limits the temporal sampling that can be achieved with modern SAR sensors with revisit times in the order of tens of days, and strongly limits the relevance of the method for many dynamic phenomena; (B) The multiplicative speckle statistic associated with SAR images limits the change detection performance because it renders

the identification of a suitable detection threshold difficult and it adds noise to the detection result; (C) The lack of automatic and adaptive techniques for the definition of change detection thresholds has hindered the development of a fully automatic change detection approach. Finally; (D) the lack of accuracy in delineating the boundary of changed regions has limited the performance of SAR data for applications that require high location accuracy of change information.

Most of the recently proposed SAR-based change detection techniques utilize the concept of ratio or difference images for suppressing background information and enhancing change information. Published methods differ in their approach to extracting a final binary change detection map from the image ratio or difference data. In Bruzzone and Prieto, (2000), two automatic unsupervised approaches based on Bayesian inferencing were proposed for the analysis of the difference image data. The first approach aims to select an adaptive decision threshold to minimize the overall change detection error, using the assumption that the pixels of the change map are spatially independent and that the gray value probability density function (PDF) of the difference image map is composed of two Gaussian distributions representing a change and a no-change class. This approach was further extended in Bazi et al. (2007) and Celik (2010) by adding an expectation-maximization (EM) algorithm to estimate the statistical parameters of the two Gaussian components. The second approach in Bruzzone and Prieto, (2000), which utilizes a Markov random field (MRF) model, is taking into account contextual information when analyzing the change map.

In Kasetkasem and Varshney, (2002), an MRF is used to model noiseless images for an optimal change image using the maximum *a posteriori* probability computation and the simulated annealing (SA) algorithm. The SA algorithm generates a random sequence of change

images, such that a new configuration is established, which depends only on the previous change image and observed images by using the Gibbs sampling procedure (Kasetkasem and Varshney, 2002).

A computationally efficient approach for unsupervised change detection is proposed in Celik (2009b). The approach initially starts by generating an h × h non-overlapping image block from the difference image. Eigenvector space is created using Principal Component Analysis (PCA) on the h × h non-overlapping image blocks. In addition, a feature vector space over the entire difference image is created by projecting overlapping h × h data blocks around each pixel onto eigenvector space. Furthermore, a k-means algorithm is employed to cluster the feature vector space into two clusters and assigns each pixel in the final change detection map to the cluster that minimizes the Euclidean distance between the pixel's feature vector and the mean feature vector of clusters (Celik, 2009b).

Several recent publications have utilized wavelet techniques for change detection from SAR. Analyzing an image in the wavelet domain helps to reduce the problems caused by the speckle noise. Wavelet domain analysis has been applied to unsupervised change detection for SAR images (Bovolo and Bruzzone, 2005; Celik, 2009a; Celik and Ma, 2010, 2011). In Bovolo and Bruzzone, (2005), a two-dimensional discrete stationary wavelet transform (2D-SWT) was applied to decompose SAR ratio images into different scale-dependent images, each of which is characterized by a tradeoff between speckle noise suppression and preservation of image details. The undecimated discrete wavelet transform (UDWT) was proposed by Celik, (2009a) to decompose the difference image. For each pixel in the difference image, a feature vector is extracted by locally sampling the data from the multiresolution representation of the difference image (Celik, 2009a). The final change detection map is obtained using a binary k-means

algorithm to cluster the multi-scale feature vectors, while obtaining two disjoint classes: change and no-change. Individual decompositions of each input image using the dual-tree complex wavelet transform (DT-CWT) are used in Celik and Ma, (2010). Each input image is decomposed into a single low-pass band and six directionally-oriented high-pass bands at each level of decomposition. The DT-CWT coefficient difference resulting from the comparison of the six high-pass bands of each input image determines classification of either change or no-change classes, creating a binary change detection map for each band. These detection maps are then merged into a final change detection map using inter-scale and intra-scale fusion. The number of decomposition scales (levels) for this method must be determined in advance. This method boasts high performance and robust results, but has a high computational cost. In Celik and Ma, (2011), a region-based active contour model with UDWT was applied to a SAR difference image for segmenting the difference image into change and no-change classes. More recently, Schmitt et al. (2010) used a curvelet-based change detection algorithm to automatically extract changes from SAR difference images.

Even though these papers have provided a solution to a subset of the limitations highlighted above, not all the limitations are solved in a single paper. The work done by Bazi et al. (2007); Bruzzone and Prieto, (2000); and Celik, (2010) does not provide an effective way to select the number of scales needed for the EM algorithm in order to avoid over- or under-estimation of the classification. Also, the noise filtering methods employed do not preserve the detailed outline of a change feature. The disadvantages of the method in Kasetkasem and Varshney, (2002) are its high computational complexity and reduced performance in the presence of speckle noise. Although the method in Celik, (2009b) achieves a good result with low computational cost, the performance of the employed PCA algorithm decreases when the data is highly nonlinear. While

Bovolo and Bruzzone, (2005); Celik, (2009a); Celik and Ma, (2010), (2011); and Schmitt et al. (2010) provided promising results in a heterogeneous image, the various methods have several disadvantages. They do not consider image acquisitions from multiple geometry, are not fully preserving the outline of the changed regions, and require manual selection of detection thresholds.

To improve upon previous work, we developed a change detection approach that is automatic, more robust in detecting surface change across a range of spatial scales, and efficiently preserves the boundaries of change regions. In response to the previously identified limitation (A), we utilize modern methods for radiometric terrain correction (RTC) (Gens and Logan, 2003; Loew and Mauser, 2007; Small, 2011) to mitigate radiometric differences between SAR images acquired from different geometries (e.g., from neighboring tracks). We show in this paper that the application of RTC technology allows combining multi-geometry SAR data into joint change detection procedures with little reduction in performance. Thus, we show that the addition of RTC results in improved temporal sampling with change detection information and in an increased relevance of SAR for monitoring dynamic phenomena.

To reduce the effects of speckle on image classification (limitation (B)), we integrate several recent image processing developments in our approach: We use modern non-local filtering methods (Darbon et al., 2008) to effectively suppress noise while preserving most relevant image details. Similarly, we perform a multi-scale decomposition of the input images to generate image instances with varying resolutions and signal-to-noise ratios. We use a 2D-SWT in our approach to conduct this decomposition.

To fully automate the classification operations required in the multi-scale change detection approach (limitation (C)), we model the probability density function of the change map at each

resolution level as a sum of two or more Gaussian distributions (similar to Bazi et al., 2007). We developed an automatic method to identify the number of Gaussian processes that make up our data and then use probabilistic Bayesian inferencing with EM algorithm and mathematical morphology to optimally separate these processes.

Finally, to accurately delineate the boundary of the changed region (limitation (D)), we utilize measurement level fusion techniques. These techniques used the posterior probability of each class at each multi-scale image to compose a final change detection map. Here we tested five different techniques including (i) product rule fusion; (ii) sum rule fusion; (iii) max rule fusion; (iv) min rule fusion; and (v) majority voting rule fusion.

These individual methods are combined in a multi-step change detection approach consisting of a pre-processing step, a data enhancement and filtering step, and the application of the multi-scale change detection algorithm. The details of the proposed approach are described in Section 3.3. A performance assessment using a synthetic dataset and an application to wildfire mapping is shown in Sections 3.4 and 3.5, respectively. A summary of the presented work is shown in Section 3.6.

3.3. Change Detection Methodology

The work presented here is motivated by the challenges associated with change detection and the desire to develop an improved algorithm for unsupervised change detection in SAR images that can provide change information at high temporal sampling rates. We aim at using information at different resolution levels to obtain high accuracy change detection maps in both heterogeneous and homogeneous regions, contributing to a change detection method that is applicable to a wide range of change situations. To achieve this goal, a multi-step processing workflow was developed that is presented in Figure 3.1. The overall contribution of our

methodology has two components. First, we developed a set of new techniques that are utilized within our change detection workflow to streamline processing and improve detection performance. As part of these techniques we (1) developed an efficient way to improve classification performance by combining EM algorithms with mathematical morphology—this is a novel contribution to this field of research; (2) we integrated a low computational complexity way to achieve high accuracy in preserving the boundary of changed regions using measurement level fusion techniques; and (3) we combine modern non-local filtering and 2D-SWT to provide robustness against noise. The second contribution comes from a novel way of combining our own technology with other published processing procedures to arrive at a new, efficient and highly flexible change detection workflow that can be applied to a wide range of change detection problems.

It is worth mentioning that the automatic process of our approach requires some parameters to be set beforehand. The parameters that need to be set include (i) the neighborhood size of the filtering step; (ii) the number of multi-scale decomposition levels; (iii) the structuring element of the morphological filter; and, finally, (iv) the maximum number of allowed change classes. Please note that while we identified optimal settings for these parameters, we found that the performance of our algorithm does not critically depend on the exact choice for these variables. This is true for the following reasons: (i) as non-local means filtering is conducted very early in the workflow, the impact of changes in the neighborhood size is mitigated by subsequent processing steps such as multi-scale decomposition and the application of mathematical morphology. Hence, we found that varying the neighborhood size from its optimal value changed system performance only slowly; (ii) in empirical tests it was found that using six decomposition levels was a good compromise between processing speed and classification

accuracy. Adding additional levels (beyond six) did not result in significant performance improvement but added computational cost. Reducing the number of layers leads to a slow decrease of change detection performance, yet this reduction of performance does not become significant unless the number of bands drops below four; (iii) from an analysis of a broad range of data from different change detection projects we found (1) that a 20 × 20 pixel-sized structuring element of the morphological filter led to the most consistent results; and (2) that change detection performance changed slowly with deviation from the 20 pixel setting. Hence, while 20 pixels was found to be optimal, the exact choice of the window size is not critical for change detection success; finally, (iv) the maximum number of allowable change classes is a very uncritical variable as it merely sets an upper bound for a subsequent algorithm that automatically determines the number of distinguishable classes in a data set (see Section 3.3.3.3). By presetting this variable to 20 classes we ensure that almost all real life change detection scenarios are captured. There is no need to change this variable unless unusually complex change detection situations with more than 20 radiometrically distinguishable change features are expected

3.3.1. SAR Data Pre-Processing

The ultimate goal of the pre-processing step is to perform image normalization, *i.e.*, to suppress all image signals other than surface change that may introduce radiometric differences between the acquisitions used in the change detection analysis. Such signals are largely related to (i) seasonal growth or (ii) topographic effects such as terrain undulation that arise if images were not acquired from near-identical vantage points. In order to enable a joint change detection analysis of SAR amplitude images acquired from different observation geometries, we attempt to

mitigate relative geometric and radiometric distortions. In a calibrated SAR image, the radar cross-section (RCS) of a pixel can be modeled as (Meyer et al., 2014):

$$\sigma = \sigma^0(\theta_i) \times A_\sigma(\theta_i) \tag{3.1}$$

where A_σ is the (incidence angle–dependent) surface area covered by a pixel, θ_i is the local incidence angle, and σ^0 is the normalized RCS. According to (1), images acquired from different geometries will differ due to the look angle dependence of both σ^0 and A_σ.

In areas that are dominated by rough surface scattering and for moderate differences $\Delta\theta_i$ of observation geometries, we can often assume that $\Delta\sigma^0(\Delta\theta_i) \ll \Delta A_\sigma(\Delta\theta_i)$ (Meyer et al., 2014). Under these conditions, the geometric dependence of σ can largely be removed by correcting for $\Delta A_\sigma(\Delta\theta_i)$. This correction is called radiometric terrain correction (Small, 2011), which is completed by the following steps:

- In the first step, geometric image distortions related to the non-nadir image geometry are removed by applying a "geometric terrain correction" step (Loew and Mauser, 2007) using a digital elevation model (DEM).
- Secondly, to remove radiometric differences between images, we use radiometric terrain normalization (Loew and Mauser, 2007). This normalization also utilizes a DEM to estimate, pixel by pixel, and compensate $A_\sigma(\theta_i)$, for the radiometric distortions.

In areas dominated by rough surface scattering, the application of RTC allows for combining SAR data acquired from moderately different incidence angles into joint change detection procedures with little reduction in performance. Hence, it can lead to significant improvements in the temporal sampling with change detection data.

An example of the effect of geometric and radiometric terrain correction is shown in Figure 3.2. Figure 3.2a shows an original ALOS PALSAR image over the Tanana Flats region in Alaska while the image after geometric and radiometric terrain correction is presented in Figure 3.2b. The normalized data is now largely free of geometric influences, reducing differences between images acquired from different geometries and enhancing the performance of change detection from multi-geometry data.

It is worth mentioning that the RTC utilized in our approach is most effective when dealing with natural environments that are dominated by rough surface scattering. For these target types, the surface scattering properties change slowly with incidence angle and differences in measured radar brightness are dominated by geometric effects. However, RTC will be less useful for areas dominated by targets with very oriented scattering characteristics (e.g., urban environments). For these regions, RTC correction may not lead to significant reduction of radiometric differences between images from different incidence angles. Furthermore, limitations exist for regions with complex small-scale topography, if this topography is not sufficiently captured in the available DEM.

3.3.2. Data Enhancement

3.3.2.1. Logarithmic Scaling and Ratio Image Formation

To suppress image background structure and improve the detectability of potential surface changes from SAR data, a ratio image is formed between a newly acquired image X_i and a reference image X_R. Using ratio images in change detection was first suggested by Dekker, (1998) and has since been the basis of many change detection methods (Bazi et al., 2005; Celik, 2010; Coppin et al., 2004). The reference image X_R and image X_i are selected such that the

effects of seasonal variations as well as spurious changes of surface reflectivity on the change detection product are minimized. Before ratio image formation, all data are geometrically and radiometrically calibrated following the approach in Section 3.3.1. The resulting ratio image can then be modeled as (Dekker, 1998):

$$O_{ir} = xT_{ir} \tag{3.2}$$

where O_{ir} is the observed intensity ratio, x is a multiplicative speckle contribution, and T_{ir} is the underlying true intensity ratio. The observed intensity ratio image has the disadvantage that the multiplicative noise is difficult to remove. Therefore, a logarithmic scaling is applied to O_{ir}, resulting in:

$$X'_{LR} = 10\,log(x) + 10\log(T_{ir}) \tag{3.3}$$

The application of logarithmic scaling and ratio image formation helps to transform our data into a near normal distribution which closely resembles a Gaussian distribution. To suppress the now-additive noise in the log-scaled ratio image (X'_{LR}), we applied a fast non-local means filtering procedure.

3.3.2.2. Fast Non-Local Means Filtering Approach

As we are interested in developing a flexible change detection method that can be applied to a wide range of change situations, we are interested in preserving the original image resolution when filtering the data. Non-local means filters are ideal for this task as they identify similar image patches in a dataset and use those patches to optimally suppress noise without sacrificing image resolution. The non-local means concept was first published in Buades et al. (2005). The algorithm uses redundant information to reduce noise, and restores the original noise-free image by performing a weighted average of pixel values, considering the spatial and intensity

similarities between pixels (Darbon et al., 2008). Given the log-ratio image X'_{LR} (see Section 3.3.2), we interpret its noisy content over a discrete regular grid, Ω.

$$X'_{LR} = \{X'_{LR}(x,y) | (x,y) \in \Omega\} \tag{3.4}$$

The restored image content $X_{LR}(x_i, y_i)$ at pixel (x_i, y_i) is then computed as a weighted average of all of the pixels in the image, according to:

$$X_{LR}(x_i, x_j) = \sum_{(x_j y_j) \in \Omega} w(i,j) X'_{LR}(x_j, y_j) \tag{3.5}$$

The weight $w(i,j)$ measures the similarities between two pixels (x_i, y_i) and (x_j, y_j) and is given by:

$$w(i,j) = \frac{1}{D(i)} e^{-\frac{s(i,j)}{h^2}} \tag{3.6}$$

where h controls the amount of filtering, $D(i)$ is the normalization constant, and $s(i,j)$ is the weighted Euclidean distance (gray-value distance) of two neighborhood pixels *(P_i* and *P_j)* that are of equal size. According to Buades et al. (2005), the similarity between two neighborhood pixels (*P_i* and *P_j)* is based on the similarity of their intensity gray level. Neighborhoods having similar gray-level pixels will have larger weights in the average. To compute the similarity of the intensity gray level, we estimated $s(i,j)$ as follows:

$$s(i,j) = \|P_i - P_j\|_a^2 \tag{3.7}$$

The standard deviation of the Gaussian kernel is denoted as a. To ensure that the averaging in Equations (3.5) – (3.7) is more robust, we set the neighborhood size for weight computation to 5 × 5 pixels and the size of the searching region to 13 × 13 pixels. We referred to Ω as the

searching window. The optimal neighborhood sizes were determined in empirical tests. These tests also showed that the choice of neighborhood size does not critically affect the filtering performance. We implemented the modern non-local filtering methods to effectively suppress the noise while preserving most relevant details in the image.

3.3.3. Change Detection Approach

The workflow of our change detection approach is shown in the lower frame of the sketch in Figure 3.1 and includes three key elements. In an initial step, a multi-scale decomposition of the input ratio images is conducted using a 2D-SWT and resulting in K image instances. Secondly, a multi-scale classification is performed at each of the K levels, resulting in K classification results per pixel. In our approach, the classifications are performed automatically and adaptively using an EM algorithm with mathematical morphology. Finally, in a third step, we conduct a measurement level fusion of the classification results to enhance the performance of our change detection.

3.3.3.1. Multi-Scale Decomposition

As previously mentioned, often our ability to detect change in SAR images is limited by substantial noise in full resolution SAR data. Here, we utilize multi-scale decomposition of our input images to generate image instances with varying resolutions and signal-to-noise ratios, and also to further reduce residual noise that remains after an initial non-local means filtering algorithm (Section 3.3.2) was applied.

Multi-scale decomposition is an elegant way to optimize noise reduction while preserving the desired geometric detail (Tello Alonso et al., 2011). In our approach, 2D-SWTs are used to decompose the log-ratio images (Wang et al., 2003). Figure 3.3 shows that in our implementation

of the wavelet decomposition we apply a set of high-pass and low-pass filters first to the rows and then to the columns of an input image at resolution level $k-1$, resulting in four decomposition images at resolution level k. The four decomposition images include (1) a lower resolution image X_{LR}^{LL} and (2) three high-frequency detail images (X_{LR}^{LH}, X_{LR}^{HL}, and X_{LR}^{HH}), where the superscripts LL, LH, HL, HH indicate in which order low-pass (L) and high-pass (H) filters were applied.

We chose the discrete stationary wavelet transform (SWT) over the discrete wavelet transform (DWT), as the SWT is computationally more efficient, shift invariant, and un-decimated (SWT adjusts the filters (up-sampling) at each level by padding them with zero in order to preserve the image size). To gain a greater flexibility in the construction of wavelet bases, we select a wavelet decomposition filter from the biorthogonal wavelet family. The biorthogonal wavelet was selected because of its symmetric capabilities, which is often desirable since it exhibits the property of linear phase, which is needed for image reconstruction. Another reason for using the biorthogonal wavelet was that, rather than having one wavelet and one scaling function, biorthogonal wavelets have two different wavelet functions and two scaling functions that may produce different multiresolution analyses. In addition, the biorthogonal wavelet has good compact support, smoothness and good localization. We choose the fifth-order filter, which has a filter length of 12. The fifth-order filter was selected to avoid distortions along the image boundary. Using SWT, the log-ratio image X_{LR} is recursively decomposed into six resolution levels. Empirical analysis suggested six to be the optimum level for multi-scale decomposition.

To reduce computation time, we focused only on the lower resolution images X_{LR}^{LL} per decomposition level. Discarding the detail images is allowed as the information contents at a

certain resolution level are recovered at a higher level. Hence, the exclusion of the detail images does not affect the change detection approach. The final multi-scale decomposition X_{MS} image stack then contains the lower resolution images at each level, as below:

$$X_{MS} = \{X_{LR}^{0}.., X_{LR}^{k} \dots\dots\dots.., X_{LR}^{K-1}\} \tag{3.8}$$

3.3.3.2. Classification by Expectation-Maximization (EM) Algorithm with Mathematical Morphology

After the multi-scale decomposition, each decomposed image is inserted into a mathematical morphology framework. Mathematical morphology defines a family of morphological filters, which are nonlinear operators that aim at emphasizing spatial structures in a gray-level image. For more details on mathematical morphology the reader is referred to (Soille, 2013). Morphological filters are defined by a structuring element (S), which is based on a moving window of a given size and shape centered on a pixel $X_{LR}(i,j)$. In image processing, erosion $\mathbb{e}(X_{LR}(i,j))$ and dilation $\mathbb{d}(X_{LR}(i,j))$ are the basic operators used, and are defined as follows (Soille, 2013):

$$\mathbb{e}(X_{LR}(i,j)) = min\{X_{LR}(i,j), x_s\} \; \forall \; x_s \; \in S(i,j) \tag{3.9}$$

$$\mathbb{d}(X_{LR}(i,j)) = max\{X_{LR}(i,j), x_s\} \; \forall \; x_s \; \in S(i,j) \tag{3.10}$$

The two morphological filters used are opening ($\mathbb{o}(X_{LR}(i,j))$) and closing ($\mathbb{c}(X_{LR}(i,j))$), and they are the concatenation of erosion and dilation. They are defined as follows:

$$\mathbb{o}(X_{LR}(i,j)) = \mathbb{d}\left(\mathbb{e}(X_{LR}(i,j))\right) \tag{3.11}$$

$$\mathbb{c}\big(X_{LR}(i,j)\big) = \mathbb{e}\left(\mathbb{d}\big(X_{LR}(i,j)\big)\right) \tag{3.12}$$

The effect of opening on a gray-level image tends to suppress regions that are brighter than the surroundings while closing suppresses regions that are darker than the surroundings. In order to preserve the spatial structures of our original image, opening by reconstruction followed with closing by reconstruction was applied. The sequence of first doing opening by reconstruction followed by closing by reconstruction is particularly designed to reduce noise in detection masks without incurring loss of details in mask outlines (Soille, 2013). Hence, it is relevant for achieving boundary preservation. The method requires an original image and a marker ($\mathbb{m}_{\mathbb{k}}$) image. If the marker image is obtained after erosion has been initially applied to the original image $\left(\mathbb{m}_{\mathbb{k}} = \mathbb{e}\big(X_L(i,j)\big)\right)$, and the original image is reconstructed by a series of iterative dilations of $\mathbb{m}_{\mathbb{k}}$, then the resulting filter is opening by reconstruction $\left(\mathbb{o}_{\mathbb{r}}(\mathbb{m}_{\mathbb{k}})\right)$:

$$\mathbb{o}_{\mathbb{r}}^{t}\left(\mathbb{e}\big(X_{LR}(i,j)\big)\right) = min\{\mathbb{m}_{\mathbb{k}}^{t}, X_{LR}(i,j)\} \tag{3.13}$$

Moreover, closing by reconstruction $\left(\mathbb{c}_{\mathbb{r}}(\mathbb{m}_{\mathbb{k}})\right)$ initially applies dilation to the original image, then reconstructs the original image by applying a series of iterative erosion. The resulting filter is:

$$\mathbb{c}_{\mathbb{r}}^{t}\left(\mathbb{d}\big(X_{LR}(i,j)\big)\right) = max\{\mathbb{m}_{\mathbb{k}}^{t}, X_{LR}(i,j)\} \tag{3.14}$$

Both filtering processes stop when $\mathbb{o}_{\mathbb{r}}^{t} = \mathbb{o}_{\mathbb{r}}^{t-1}$ and $\mathbb{c}_{\mathbb{r}}^{t} = \mathbb{c}_{\mathbb{r}}^{t-1}$. It is worth mentioning that in this paper, we used a fixed square shape $S(i,j)$ with a size of 20 × 20 pixels. From an analysis of a broad range of data from different change detection projects, we found (1) that most consistent results were achieved with a 20 pixel window; and (2) that change detection performance changed slowly with deviation from the 20 pixel setting. Hence, while 20 pixels

was found to be optimal, the exact choice of the window size is not critical for change detection success. The new multi-scale decomposition X_{MD} stack now contains morphological filtered images at each level in X_{MS}, as below:

$$X_{MD} = \left\{X_{MD}^{0}.., X_{MD}^{k} \ldots\ldots\ldots.., X_{MD}^{K-1}\right\} \tag{3.15}$$

The importance of opening and closing by reconstruction is that it filters out darker and brighter elements smaller than $S(i,j)$, while preserving the original boundaries of structures in our image. Note that morphological filtering leads to a quantization of the gray-value space such that each image in X_{MD} can be normalized into the gray-value range of [0, 255] without loss of information. At the kth level in X_{MD}, a lossless normalization is applied, leading to a float value between 0 and 255, such that:

$$X_{MD}^{k} = \frac{X_{MD}^{k} - min\left(X_{MD}^{k}\right)}{max\left(X_{MD}^{k} - min\left(X_{MD}^{k}\right)\right)} \times 255 \tag{3.16}$$

After the mathematical morphology step, we calculate the posterior probability of one "no-change" and potentially several "change" classes at every one of the K resolution levels, resulting in K posterior probabilities per pixel. The various classes are assumed to be a mixture of Gaussian density distributions. While an approximation, assuming Gaussian characteristics for SAR log-ratio data is not uncommon. Previous research (Dekker, 1998) has found that the statistical distribution of log-ratio data is near normal and closely resembles a Gaussian distribution. Hence, our assumption of Gaussian characteristics is only weakly affecting the performance of our change detection approach. Still, we are currently assessing the benefits of using non-Gaussian descriptions in these processing steps and, depending on the results of this study, may modify our approach in the future. To automate the calculation of the posterior

probabilities, we employ an EM approach. The importance of integrating mathematical morphology into our EM algorithm framework is to suppress the effect of background clutter that may constitute false positives after applying the EM algorithm.

The EM algorithm focuses on discrimination between the posterior probability of one no-change (ω_u) and potentially several change classes (ω_c). For each level in X_{MD}, we model the probability density function $p(X_{MD})$ of the normalized image series X_{MD} as a mixture of N density distributions. This mixture contains the probability density functions, denoted $p(X_{MD}|\omega_c)$ and $p(X_{MD}|\omega_u)$, and the prior probability, $P(\omega_c)$ and $P(\omega_u)$. At the k^{th} level in X_{MD}, the probability density function (PDF) is modeled as:

$$p(X_{MD}^k) = \sum_{n=1}^{N-1} \left(p(X_{MD}^k|w_c^n)P(w_c^n)\right) + p(X_{MD}^k|\omega_u)P(\omega_u) \tag{3.17}$$

The first summand in Equation (3.17) ($\sum_{n=1}^{N-1} p(X_{MD}^k|w_c^n)P(w_c^n)$) represents the mixture of $N-1$ change PDFs described by their respective likelihood $p(X_{MD}^k|w_c^n)$ and prior probabilities $P(w_c^n)$, while the second summand describes the PDF of a single no-change class. It is worth noting that all PDFs in Equation (3.17) are assumed to be of Gaussian nature, such that the mean μ_{ω_c} and variance $\sigma_{\omega_c}^2$ are sufficient to define the density function associated with the change classes ω_c, and mean μ_{ω_u} and variance $\sigma_{\omega_u}^2$ can be used to describe the density function related with the no-change classes ω_u. The parameters in Equation (3.17) are estimated using an EM algorithm. Given X_{MD}^k is the k^{th} level image in X_{MD}, we inferred which class ($\omega_i = (\omega_c, \omega_u)$) each pixel in X_{MD}^k belongs to, using $\Theta^s = \left(\mu_{\omega_c}, \sigma_{\omega_c}^2, \mu_{\omega_u}, \sigma_{\omega_u}^2\right)$ which is our current (best) estimate for the full distribution, and Θ as our improved estimate. The expectation step at the sth iteration is calculated by the conditional expectation:

$$Q(\Theta|\Theta^s) = E\left[\ln P\left(\omega_i, X_{MD}^k|\Theta|X_{MD}^k, \Theta^s\right)\right] = \sum P\left(\omega_i|X_{MD}^k, \Theta^s\right)\ln P\left(\omega_i, X_{MD}^k|\Theta\right) \quad (3.18)$$

The maximization step maximizes $Q(\Theta|\Theta^s)$ to acquire the next estimate:

$$\Theta^{(s+1)} = \underset{\Theta}{\operatorname{argmax}}\, Q(\Theta|\Theta^s) \quad (3.19)$$

The iterations cease when the absolute differences between the previous and current variables are below a tolerance value (ε). In our paper, we empirically set the tolerance value ε to 10^{-6}. Once the iterations cease, the final optimal $\Theta^{(s+1)}$ is used to calculate the posterior probability using Bayes' formula. The EM algorithm is applied separately to all K levels of the multi-scale decomposition series, X_{MD}, resulting in a stack of posterior probability maps $PP_{MD} = \{PP^0, \ldots . PP^k, \ldots ., PP^{K-1}\}$ of depth K where each map contains the posterior probability of change and no-change classes, respectively. Our EM algorithm is illustrated as follows:

3.3.3.3. Selection of Number of Change Classes

In order to execute the expectation maximization algorithm from Section 3.3.3, the number of change classes that are present in an image has to be known. Selection of classes is a difficult task, and care should be taken to avoid over- or under-classifying the data. Various methods have been proposed for selecting the number of classes (N) to best fit the data, and examples include the penalty method (Zhu and Bamler, 2010), the cross-validation method (Pham, 2001) and the minimum description length approach (Bischof et al., 1999). In our paper, we developed a selection approach that identifies the number of required classes (N) using a sum of square error (SSE) approach. The SSE approach utilized the measured data PDF, which is the statistical distribution of the highest decomposition level image, and the estimated PDF, which is the statistical distribution estimated after applying the EM algorithm to the highest decomposition

level image. The highest decomposition level image was used because at this level, most of the noise in the image was filtered out. This approach seeks to minimize the sum of the square of the differences between the measured data PDF and the estimated PDF, as follows:

$$SSE = \sum_{i=2}^{NN} (m_{ii} - f_{ii})^2 \tag{3.20}$$

where NN is the overall number of classes, m_{ii} is the original measured PDF and f_{ii} is the estimated PDF. An example of the dependence of SSE on the number of classes used in f_{ii} is shown in Figure 3.4. Initially, we start with two classes (one change and one no-change class) and calculate the SSE. For each extra class that is added into the procedure, its corresponding SSE is estimated. Plotting each class sequentially against its corresponding SSE leads to a continuous decrease of approximation error as NN gets larger.

The data from Section 3.5 is used in this example and SSE was carried out using a maximum of 20 classes, with each classes being added sequentially. The knee point on the curve in Figure 3.4 suggests that 3 is a good candidate for N.

3.3.3.4. Measurement Level Fusion

We developed a measurement level fusion technique to accurately delineate the boundary of the changed region by using the posterior probability of each class at each multi-scale image to compose a final change detection map (M). We developed and tested five measurement level fusion methods that are briefly explained below:

1. Product rule fusion: This fusion method assumes conditionally statistical independence, and each pixel is assigned to the class that maximizes the posterior conditional probability, creating a change detection map. Each pixel is assigned to the class such that

$$\omega_i = \underset{\omega_i \varepsilon \{\omega_c, \omega_u\}}{\operatorname{argmax}} \prod_{i=0}^{K} \left\{ P(\omega_i | X_{MD}^k(i,j)) \right\}$$

$$= \underset{\omega_i \varepsilon \{\omega_c, \omega_u\}}{\operatorname{argmax}} \prod_{i=0}^{K} \left\{ PP^i \right\} \tag{3.21}$$

2. Sum rule fusion: This method is very useful when there is a high level of noise leading to uncertainty in the classification process. This fusion method assumes each posterior probability map in X_{MD} does not deviate much from its corresponding prior probabilities. Each pixel is assigned to the class such that

$$\omega_i = \underset{\omega_i \varepsilon \{\omega_c, \omega_u\}}{\operatorname{argmax}} \sum_{i=0}^{K} \left\{ PP^i \right\} \tag{3.22}$$

3. Max rule fusion: Approximating the sum in Equation (3.22) by the maximum of the posterior probability, we obtain

$$\omega_i = \underset{\omega_i \varepsilon \{\omega_c, \omega_u\}}{\operatorname{argmax}} \underset{i=0}{\overset{K}{max}} \left\{ PP^i \right\} \tag{3.23}$$

4. Min rule fusion: This method is derived by bounding the product of posterior probability. Each pixel is assigned to the class such that

$$\omega_i = \underset{\omega_i \varepsilon \{\omega_c, \omega_u\}}{\operatorname{argmax}} \underset{i=0}{\overset{K}{min}} \left\{ PP^i \right\} \tag{3.24}$$

5. Majority voting rule fusion: This method assigns a class to the pixel that carries the highest number of votes. Each pixel in each posterior probability map (PP_{MD}) is converted to binary, *i.e.*,

$$\Delta_{bn}^{i} = \begin{cases} 1, if \ \ \underset{i=0}{\overset{K}{max}}\{PP^{i}\} \\ 0, otherwise \end{cases}$$

$$\omega_i = \underset{\omega_i \varepsilon \{\omega_c, \omega_u\}}{\text{argmax}} \sum_{i=0}^{K} \Delta_{bn}^{i} \tag{3.25}$$

The measurement level fusion with the lowest overall error, highest accuracy, and highest kappa coefficient is selected as the best fusion method and is used as our final change detection map. The next section shows how the best fusion method was selected.

3.4. Performance Assessment Using Synthetic Data

To assess the performance of the developed change detection approach under both controlled and uncontrolled conditions, we have conducted two types of validation studies, both of which are presented in this paper. In this section, we summarize change detection results on a synthetic dataset to evaluate the performance and limitations of the technique under controlled conditions. Subsequently, in the next section, we show an application of the developed change detection technique to wildfire mapping. An area in Alaska is chosen and the change detection results are compared to ground truth measurements for validation.

3.4.1. Description of Synthetic Dataset

A synthetic dataset of size 1152 × 1152 pixels was generated from two SAR images acquired over the same area but at different times, and "change patches" were artificially introduced into the second of these images. A post-event image was generated by adding 2 dB to the radar cross-section of certain locations to form the change patches. Our approach was tested on synthetic data, because with synthetic data, we can control every aspect of the data, and also

evaluate the accuracy with absolute reliability. The purpose of analyzing the synthetic dataset was to assess, more accurately, the robustness of the proposed approach and also to select the best measurement level fusion.

It is worth mentioning that, with the exception of the border pixels, moderate changes in speckle noise do not significantly impact our classification result. This is due to the mitigating effects of the wavelet decomposition and due to the way decisions at different decomposition levels are merged in our approach. In homogeneous areas (e.g., within the change patches), the higher decomposition levels carry the majority of the weight in the classification of these areas. As most speckle noise is removed at these higher decomposition levels, the classification result within homogeneous areas is very robust to speckle noise. Only in heterogeneous areas (the boundary pixels of our simulated data), where lower decomposition levels contribute more to the final classification result, residual speckle noise may have a measurable effect on performance. As there are only very few boundary pixels and as we only applied a very moderate change of radar cross-section, we believe that neglecting the recalculation of speckle is a well-justified decision. Figure 3.5a shows the ratio image generated between the synthetic pre-event image and the post-event images, while Figure 3.5b depicts the ground truth change map. The faint change signatures in Figure 3.5a indicate that a challenging change detection situation was generated.

3.4.2. Performance Evaluation for Selecting Best Fusion Method

For selecting the best performing fusion method, quantitative measurements are derived from the binary change detection map obtained using the different measurement level fusion techniques. In generating the confusion matrix which shows the accuracy of our classification result, the following defined quantities are computed: (i) the false alarm (FA), which signifies the no-change pixels incorrectly classified as change. The false alarm rate (FAR) is computed in

percentage as $FAR = FA/N_1 \times 100\%$, where N_1 is the total number of unchanged pixels in the ground truth change detection map; (ii) the missed alarm (MA), which signifies the changed pixels incorrectly classified as no-change. The missed alarm rate (MAR) is computed in percentage as $MAR = MA/N_0 \times 100\%$, where N_0 is the total number of changed pixels in the ground truth change detection map; (iii) the overall error (OE), which is the percentage ratio of incorrect classification made (addition of both the false alarm rate and missed alarm rate). Hence, $OE = (FA + MA)/(N_1 + N_0) \times 100\%$; (iv) the overall accuracy (OA), which is calculated by adding the number of pixels classified correctly and dividing it by the total number of pixels. Therefore $OA = 100\% - OE$; and (v) the kappa coefficient, which measures the agreement between classification pixels and ground truth pixels (Guide, 2008). A kappa value of 1 represents perfect agreement while a value of 0 represents no agreement. Table 3.1 shows the quantitative performance of each of the measurement level fusion techniques. It can be seen that *product rule fusion* achieved the best performance with an overall accuracy of 98.97%.

3.4.3. Comparison to Alternative Change Detection Methods

To evaluate the performance of our proposed algorithm relative to the state-of-the-art, we conducted an extensive qualitative (Figure 3.6) and quantitative (Table 3.2) comparison of the results of our change detection approach to results of other recently published change detection methods. The following alternative methods were used in the comparison: (a) Method A: our proposed approach is used without fast non-local means filtering; (b) Method B: our proposed approach is used without 2D-SWT and measurement level fusion—the approach utilized mathematical morphology and the EM algorithm for classification; (c) Method C: our proposed approach is used without morphological filtering; (d) Method D: our proposed approach is used without the EM algorithm—the approach employed the thresholding algorithm proposed by

Otsu, (1975) and majority voting rule fusion for classification; (e) Method E: semi-supervised change detection, based on using a kernel-based abnormal detection into the wavelet decomposition of the SAR image (Mercier and Girard-Ardhuin, 2006); (f) Method F: image denoising using fast discrete curvelet transform via wrapping with the EM algorithm to produce the change detection map (AlZubi et al., 2011); (g) Method G: using UDWT to obtain a multiresolution representation of the log-ratio image, then identifying the number of reliable scales, and producing the final change detection map using fusion at feature level (FFL_ARS) on all reliable scales (Bovolo and Bruzzone, 2005); (h) Method H: implementing probabilistic Bayesian inferencing with the EM algorithm to perform unsupervised thresholding over the images generated by the dual-tree complex wavelet transform (DT-CWT) at various scales, and moreover, using intra- and inter-scale data fusion to produce the final change detection map (Celik, 2010); (i) Method I: obtaining a multiresolution representation of the log-ratio image using UDWT, then applying the Chan–Vese (region-based) active contour model to the multiresolution representation to give the final change detection map (Celik and Ma, 2011). Based on Table 3.2 and Figure 3.6, one can observe that the change detection result from Method G showed the lowest performance of all tested methods with an overall accuracy of 68.412% and a kappa coefficient of 0.162. The low performance of this approach is due to the effectiveness of the method employed to select the optimal resolution level (reliable scale). The result of Method G was computed by averaging the reliable scales for every pixel which led to the low performance. Thus, most reliable scales contain a large amount of both geometrical details and speckle components (lowest decomposition level) and a low amount of geometrical details and speckle components (highest decomposition level). The proposed method yields the best performance with an overall accuracy of 98.973% and a kappa coefficient of 0.906. It is worth

mentioning that the aim of Methods A–D is to show the importance of each element in our proposed approach (see gray shade area in Table 3.2).

3.5. Performance Analysis through Application to Wildfire Mapping

3.5.1. Description of Area

The study area for this real-data experiment is situated around the Tanana Flats region of Alaska, just east of the communities of Healy, Clear, Anderson and Nenana, and approximately 26 miles southwest of Fairbanks, Alaska (Figure 3.7). The topography of the area is relatively flat and is comprised of low-vegetation tundra and taiga regions with an interspersed network of small streams. The forest vegetation of the area is diverse, containing white spruce, black spruce, aspen and birch. During the hot summer climate, this area is very prone to wildfires.

In Alaska, wildfires affect thousands of km^2 each year (Wendler et al., 2011). The dry conditions, increased lightning strikes, and higher-than-normal temperatures cause atmospheric effects that impact the strength of wildfires (Wendler et al., 2011). The strongest occurrences of wildfires in Alaska happen in the mid-summer months, and occurrences vary annually. According to the Alaska interagency coordination center, the mapped fire in our study area is called the Survey Line fire, which started in the year 2001. This fire, caused by lightning, consumed an area of 796 km^2, and lasted four months from 20 June to 14 October 2001. During the winter of the year 2002, the fire scar disappears and this is likely due to the freezing of the soils and the addition of a seasonal snow cover (see Section 3.5.5). By the beginning of the year 2004, the trees in the fire scar area have regenerated.

3.5.2. Description of SAR and Reference Data Used in this Study

We obtained eight, HH-polarized (horizontal transmit and horizontal receive polarization), Radarsat-1 images acquired between 2000 and 2004 over the area of interest. Only acquisitions between April and October of pre- and post-fire images were used to avoid seasonal effects in change detection. For ease of visual comparison, the acquisition is not shown successively according to the year but according to the pre- and post-fire images. Pre-fire images (images showing no fire scar) are displayed first, and are shown in Figure 3.8a–d, while the post-fire images (images showing fire scar) can be found in Figure 3.8e–h.

Each image has a size of 3584 × 5056 pixels, corresponding to an area of 44.8 × 63.2 square kilometers. The pixel spacing in each image is 12.5 × 12.5 m with a range resolution of 26.8 m and an azimuth resolution of 24.7 m. The eight Radarsat-1 images were used to generate seven different ratio images, and were used for the analysis of seven different detection scenarios (scenarios 1–7 in Table 3.3). Table 3.3 shows the seven independent scenarios that we investigated to analyze the performance of our approach. The image acquisitions highlighted in gray in Table 3.3 are the post-fire images, while the rest of the acquisitions are pre-fire images. Three of the analyzed scenarios are "negative tests" as they do not include fire activity and test our ability to correctly identify no-change scenarios. The four remaining scenarios include change signatures related to wildfires and allow us to quantify our ability to correctly detect fire perimeters. Table 3.4 shows the incidence angle of all the individual image acquisitions. The image acquisitions highlighted in gray in Table 3.4 are images with a different incidence angle. All the images were radiometrically corrected using the Alaska IFSAR DEM which has a resolution of 5 m. The images were calibrated and co-registered as well, with ASF *MapReady* software, then geocoded to latitude and longitude (Gens and Logan, 2003). Notice that the pre-

and post-fire comparisons in scenarios 2 and 5 collated images with different incidence angles. These comparisons were included to test our approach's ability to increase temporal resolution through the combination of images of varying geometry (see Section 3.3.1).

To validate achieved detection results, we used a fire area history map generated by the Alaska Fire Service as ground truth. The fire area history map was prepared using ground-based GPS, which, although effective, suffers from the limitation that everything inside the fire area history map is considered to be wildfire. We modified the fire area history map by using optical imagery to visually digitize areas that are not actually affected by wildfire. Other limitations the Alaska Fire Service faced include time and safety.

3.5.3. Description of Classification Processes

Based on several experiments, the performance of our approach was measured qualitatively and quantitatively by comparing detections to a fire area history map. To execute the classification process, ratio images (scenarios 1–7) previously shown in Table 3.3 were filtered and decomposed into six resolution levels. As previously described, 2D-SWT using the biorthogonal wavelets procedure was employed.

As an example of the decomposition process, Figure 3.9 shows the decomposed images for scenario 4. Looking at the highest resolution images in Figure 3.9 (top left panel of each sub-Figure), we see how the contrast between background and change regions is initially low due to the significant noise in the data. This contrast is continuously improving with the increasing decomposition level. This is due to a continuous improvement of noise suppression through the K levels. At the same time, the loss of contrast and detail level can be observed for higher decomposition levels, which is particularly strong at the border between the background and changed area.

For every of the decomposed K resolution levels, we calculate the posterior probability of one "no-change", one "negative change" and one "positive change" class, resulting in K posterior probabilities per pixel. Product rule fusion is then used to fuse the K classification results achieved per pixel and to produce the final classification map M. Table 3.5 shows the quantitative comparison of each fusion method to confirm our choice of product rule fusion as the best-performing method. It is evident that product rule fusion gave a better result with an overall accuracy of 99.932% and a kappa coefficient of 0.997. Figure 3.10 shows a qualitative comparison of the burned area detected by our algorithm to the available fire area information (red outlines in Figure 3.10) retrieved from the archives of the Alaska interagency coordination center.

A good match between the automatic detection and ground truth information can be observed. Particularly note (1) the "cleanness" of the detection result outside of the burn scar and (2) the close preservation of the burn scar boundary that was achieved. Both properties indicate our method's ability to simultaneously achieve high performance noise suppression and outline preservation. Classification results for the remaining six scenarios are shown in Figure 3.11. These results show good performance for both the "negative" and the "positive" tests. As expected, no extended change was identified for the scenarios that did not span a forest fire. Some change was identified along a stream that crosses the area. This change is likely real and due to changes of river flow patterns or water level variations. Even though three classes (see Section 3.3.3.3) were used for the classification in areas with negative change, none of the classes have a mean similar to that of a fire scar class. All "positive" tests reliably identify the burn scar and retrace its boundary. Figure 3.11b and d showed that the classification of fire scars was not inhibited by the varying geometry of the pre- and post-fire images. Thus, this approach

is able to increase the temporal sampling of our image acquisitions. The benefit of radiometric normalization for combining data with different observation geometry is quantified by comparing scenario 5 with and without radiometric and geometric normalization. Employing radiometric and geometric normalization to scenario 5 gave an overall accuracy of 97.78% and a kappa coefficient of 0.924. When radiometric and geometric normalization is not employed we have an overall accuracy of 87.08% and a kappa coefficient of 0.585.

3.5.4. Comparison to Reference Change Detection Techniques

Change detection results obtained from different approaches for scenario 4 are analyzed quantitatively in Table 3.6 and qualitatively in Figure 3.12. Our proposed approach yields an overall accuracy of 99.932%, an overall error of 0.067%, and a kappa coefficient of 0.997. The performance of our approach without a fast non-local means filter gave a good result as well. However, the accuracy was reduced as a result of a false positive, causing the overall accuracy and kappa coefficient to drop to 98.402% and 0.946%, respectively. The performance decreased when wavelet transform was not utilized in our approach, giving an overall accuracy of 97.823% and a kappa coefficient of 0.927. Furthermore, without the application of the morphological filter the performance dropped, giving an overall accuracy of 97.963% and a kappa coefficient of 0.932. Also, in the absence of the EM algorithm in our approach, the accuracy dropped to 97.550% and the kappa coefficient dropped to 0.916. Given the results of Methods A–D (see gray shade area in Table 3.6), it is evident that each individual processing step is important for the effectiveness of our approach. With regard to other published techniques, Method E gave a lower accuracy when compared with our approach, with an overall accuracy of 93.816% and a kappa coefficient of 0.808. The lower accuracy is likely due to the region of interest definition which leads to spectral confusion and resulted in several numbers of false positives and false

negatives in the final change detection result. The curvelet method (Method F) effectively filtered the ratio image; however, it only relies on the EM algorithm to classify the fire scar. The method has an overall accuracy of 93.054% and a kappa coefficient of 0.745. According to Method G, no filtering was done, along with the absence of the EM algorithm. The thresholding of fire scars was done manually, and this reduced the effectiveness of the method. Method G has an overall accuracy of 94.986% and a kappa coefficient of 0.830. The degradation in the accuracy of the change detection result from Method H, with respect to the proposed approach, is mainly because of the DT-CWT used. The DT-CWT is fairly robust to speckle noise, and the down-sampling process used is not able to detect the changes whose spatial supports are lost through the multi-scale decomposition. Method H gave an overall accuracy of 89.078% and a kappa coefficient of 0.605. Method I showed a decent detection with an overall accuracy of 96.587% and a kappa coefficient of 0.891. This is mainly due to the effective contour definition that partitions the ratio image into change and no-change.

It is worth mentioning that all the methods used for comparative analysis were sent through the identical pre-processing chain including SAR data pre-processing, ratio image formation and logarithmic scaling, fast non-local means filtering and mathematical morphology filtering. While the fire scars are correctly delineated in Methods E–I, minute changes (false positive) in the background landscape were detected and amplified. Attempts to reduce the number of false positives for these techniques led to a significant distortion of the fire-scar boundaries and reduced the reliability of the final change detection map. Thus, our proposed approach produced a more consistent and more robust result as indicated by the information in Figure 3.12 and Table 3.6.

3.5.5. Electromagnetic Interpretation of Change Signatures

After change features are detected using the aforementioned approach, the history of the amplitude change can be analyzed to attempt a geophysical interpretation of the observed change. In this section, we show the kinds of analyses that can be conducted after a robust change detection approach were applied to a time series of SAR images.

In the presented wildfire scenarios, we observe (from the time-series of data that was analyzed) that the burn event led to a general increase of the average radar cross-section in the affected areas (Figure 3.13). An increase of about 4 dB relative to the pre-fire situation can be observed. This is likely due to an increase of double bounce scattering after the tree foliage was burned off, exposing the remaining tree stumps and branches for interaction with the microwave signals. Figure 3.13 also shows that the radar cross-section in the affected area slowly decreases starting about 1.5 years after the burn event. This slow return toward pre-fire image brightness is likely related to regrowth in the affected area.

It is worth mentioning that seasonal effects can be observed in the detection of the fire scar in our study area. While during the summer seasons the average radar brightness remained significantly above the pre-burn level throughout the time series, it can be observed that the average brightness value decrease during the winter periods, likely due to the freezing of the soils and the addition of a seasonal snow cover. After the winter periods, the average brightness value increases again near the radar cross-section of the previous summer. This is an interesting and significant observation as it indicates that, for this test site and dataset, fire scar detection will be less successful during winter.

To support our interpretation of the data, we plot a second time series in Figure 3.13 (red line) that shows the average radar cross-section of an area unaffected by fire in all pre- and post-

fire images. The seasonal brightness variations can also be observed for this area, supporting the assertion of weather effects as the cause of the seasonal signal.

3.6. Conclusion

A flexible and automatic change detection method was presented that is effective at identifying change signatures from pairs of SAR images. The proposed approach removes radiometric differences between SAR images acquired from different geometries by utilizing radiometric terrain correction (RTC) which enables change detection from different image geometries and, hence, improves the temporal sampling of surface change that can be achieved from a given database. Suppressing background information and enhancing change information by performing log-ratio operations, our approach displayed high detection performance while preserving change signature details. The integration of modern non-local filtering and 2D-SWT techniques provided robustness against noise. The classification performance, increased by integrating an EM algorithm with mathematical morphology and preservation of the geometric details in the border regions, was shown when product rule fusion was employed. Moreover, our approach gave a very high overall accuracy. In addition to analyzing the performance of our approach on synthetic data, we used our algorithm to conduct change detection in an area affected by wildfires. From this change detection analysis, we found that a fire scar could be detected with high accuracy from the available data. In addition to accurately detecting the location and extent of the burn scar, an analysis of the image information within the detected scar revealed slow changes in image amplitudes over time, most likely related to the regrowth of forest within the burned area.

Comparison of our approach to selected recent methods showed that (1) our approach performed with a high overall accuracy and high geometric preservation; (2) neglecting any of the steps in our approach will result in an inferior change detection capability.

The main drawbacks of the proposed approach are: (1) the assumption that the image is a mixture of Gaussian distribution; and (2) that the approach does not take full advantage of all the information present in the speckle. Future work will explore using Gamma distribution for fitting the EM algorithm rather than the assumed Gaussian distribution. Non-uniform geometric and radiometric properties for all the areas of change in the synthetic image will be pursued as well. Images with high varying geometry will be considered and analyzed. In addition, the development of the advanced approach for selecting the number of changed classes will be pursued.

3.7. Acknowledgments

The authors want to thank the Alaska Satellite Facility (ASF) for providing access to the Radarsat-1 data used in this study. We furthermore thank the Geographic Information Network of Alaska (GINA) for the provision of high resolution Digital Elevation Models (DEMs) and for providing computing support. Thanks to Maria Tello Alonso for many fruitful discussions. The work presented here was funded by the National Aeronautics and Space Administration (NASA) through Established Program to Stimulate Competitive Research (EPSCoR) program under grant #NNX11AQ27A.

3.8. Author Contributions

This research was written and revised by Olaniyi Ajadi with contributions from all coauthors. All authors have read and approved the final manuscript.

3.9. References

AlZubi, S., Islam, N., and Abbod, M., 2011, Multiresolution analysis using wavelet, ridgelet, and curvelet transforms for medical image segmentation: Journal of Biomedical Imaging, v. 2011, p. 4.

Bazi, Y., Bruzzone, L., and Melgani, F., 2005, An unsupervised approach based on the generalized Gaussian model to automatic change detection in multitemporal SAR images: IEEE Transactions on Geoscience and Remote Sensing, v. 43, no. 4, p. 874-887.

Bazi, Y., Bruzzone, L., and Melgani, F., 2007, Image thresholding based on the EM algorithm and the generalized Gaussian distribution: Pattern Recognition, v. 40, no. 2, p. 619-634.

Bischof, H., Leonardis, A., and Selb, A., 1999, MDL principle for robust vector quantisation: Pattern Analysis & Applications, v. 2, no. 1, p. 59-72.

Bovolo, F., and Bruzzone, L., 2005, A detail-preserving scale-driven approach to change detection in multitemporal SAR images: IEEE Transactions on Geoscience and Remote Sensing, v. 43, no. 12, p. 2963-2972.

Bruzzone, L., and Prieto, D. F., 2000, Automatic analysis of the difference image for unsupervised change detection: IEEE Transactions on Geoscience and Remote Sensing, v. 38, no. 3, p. 1171-1182.

Buades, A., Coll, B., and Morel, J.-M., 2005, A review of image denoising algorithms, with a new one: Multiscale Modeling & Simulation, v. 4, no. 2, p. 490-530.

Celik, T., 2009a, Multiscale change detection in multitemporal satellite images: Geoscience and Remote Sensing Letters, IEEE, v. 6, no. 4, p. 820-824.

Celik, T., 2009b, Unsupervised change detection in satellite images using principal component analysis and-means clustering: Geoscience and Remote Sensing Letters, IEEE, v. 6, no. 4, p. 772-776.

Celik, T., 2010, A Bayesian approach to unsupervised multiscale change detection in synthetic aperture radar images: Signal Processing, v. 90, no. 5, p. 1471-1485.

Celik, T., and Ma, K.-K., 2010, Unsupervised change detection for satellite images using dual-tree complex wavelet transform: IEEE Transactions on Geoscience and Remote Sensing, v. 48, no. 3, p. 1199-1210.

Celik, T., and Ma, K.-K., 2011, Multitemporal image change detection using undecimated discrete wavelet transform and active contours: IEEE Transactions on Geoscience and Remote Sensing, v. 49, no. 2, p. 706-716.

Coppin, P., Jonckheere, I., Nackaerts, K., Muys, B., and Lambin, E., 2004, Review ArticleDigital change detection methods in ecosystem monitoring: a review: International Journal of Remote Sensing, v. 25, no. 9, p. 1565-1596.

D'Addabbo, A., Refice, A., Pasquariello, G., Lovergine, F. P., Capolongo, D., and Manfreda, S., 2016, A Bayesian Network for Flood Detection Combining SAR Imagery and Ancillary Data: IEEE Transactions on Geoscience and Remote Sensing, v. 54, no. 6, p. 3612-3625.

Darbon, J., Cunha, A., Chan, T. F., Osher, S., and Jensen, G. J., 2008, Fast nonlocal filtering applied to electron cryomicroscopy, *in* Proceedings Biomedical Imaging: From Nano to Macro, 2008. ISBI 2008. 5th IEEE International Symposium, p. 1331-1334.

Dekker, R. J., 1998, Speckle filtering in satellite SAR change detection imagery: International Journal of Remote Sensing, v. 19, no. 6, p. 1133-1146.

Floyd, A. L., Prakash, A., Meyer, F. J., Gens, R., and Liljedahl, A., 2014, Using Synthetic Aperture Radar to Define Spring Breakup on the Kuparuk River, Northern Alaska: Arctic, p. 462-471.

Gens, R., and Logan, T., 2003, Alaska Satellite Facility Software Tools: Manual: Geophysical Institute, University of Alaska Fairbanks.

Guide, E. U. S., 2008, ENVI on-line software user's manual: ITT Visual Information Solutions.

Kasetkasem, T., and Varshney, P. K., 2002, An image change detection algorithm based on Markov random field models: IEEE Transactions on Geoscience and Remote Sensing, v. 40, no. 8, p. 1815-1823.

Loew, A., and Mauser, W., 2007, Generation of geometrically and radiometrically terrain corrected SAR image products: Remote Sensing of Environment, v. 106, no. 3, p. 337-349.

Mercier, G., and Girard-Ardhuin, F., 2006, Partially supervised oil-slick detection by SAR imagery using kernel expansion: IEEE Transactions on Geoscience and Remote Sensing, v. 44, no. 10, p. 2839-2846.

Meyer, F. J., McAlpin, D. B., Gong, W., Ajadi, O., Arko, S., Webley, P. W., and Dehn, J., 2014, Integrating SAR and derived products into operational volcano monitoring and decision support systems: Journal of Photogrammetry and Remote Sensing, no. 100, p. 106-117.

Otsu, N., 1975, A threshold selection method from gray-level histograms: Automatica, v. 11, no. 285-296, p. 23-27.

Pham, D. L., 2001, Spatial models for fuzzy clustering: Computer Vision and Image Understanding, v. 84, no. 2, p. 285-297.

Schmitt, A., Wessel, B., and Roth, A., 2010, Curvelet-based change detection on SAR images for natural disaster mapping: Photogrammetrie-Fernerkundung-Geoinformation, v. 2010, no. 6, p. 463-474.

Siegert, F., and Hoffmann, A. A., 2000, The 1998 forest fires in East Kalimantan (Indonesia): A quantitative evaluation using high resolution, multitemporal ERS-2 SAR images and NOAA-AVHRR hotspot data: Remote Sensing of Environment, v. 72, no. 1, p. 64-77.

Small, D., 2011, Flattening gamma: Radiometric terrain correction for SAR imagery: IEEE Transactions on Geoscience and Remote Sensing, v. 49, no. 8, p. 3081-3093.

Soille, P., 2013, Morphological image analysis: principles and applications, Springer Science & Business Media.

Tello Alonso, M., López-Martínez, C., Mallorquí, J. J., and Salembier, P., 2011, Edge enhancement algorithm based on the wavelet transform for automatic edge detection in SAR images: IEEE Transactions on Geoscience and Remote Sensing, v. 49, no. 1, p. 222-235.

Tello, M., Lopez-Martinez, C., Mallorqui, J. J., Danisi, A., Di Martino, G., Iodice, A., Ruello, G., and Riccio, D., 2007, Characterization of local regularity in SAR imagery by means of multiscale techniques: application to oil spill detection, *in* Proceedings Geoscience and Remote Sensing Symposium. IGARSS 2007. IEEE International, p. 5228-5231.

Wang, X., Istepanian, R. S., and Song, Y. H., 2003, Microarray image enhancement by denoising using stationary wavelet transform: IEEE Transactions on NanoBioscience, v. 2, no. 4, p. 184-189.

Wendler, G., Conner, J., Moore, B., Shulski, M., and Stuefer, M., 2011, Climatology of Alaskan wildfires with special emphasis on the extreme year of 2004: Theoretical and Applied Climatology, v. 104, no. 3-4, p. 459-472.

Yun, S.-H., Fielding, E. J., Webb, F. H., and Simons, M., 2012, Damage proxy map from interferometric synthetic aperture radar coherence, Google Patents.

Zhu, X. X., and Bamler, R., 2010, Very high resolution spaceborne SAR tomography in urban environment: IEEE Transactions on Geoscience and Remote Sensing, v. 48, no. 12, p. 4296-4308.

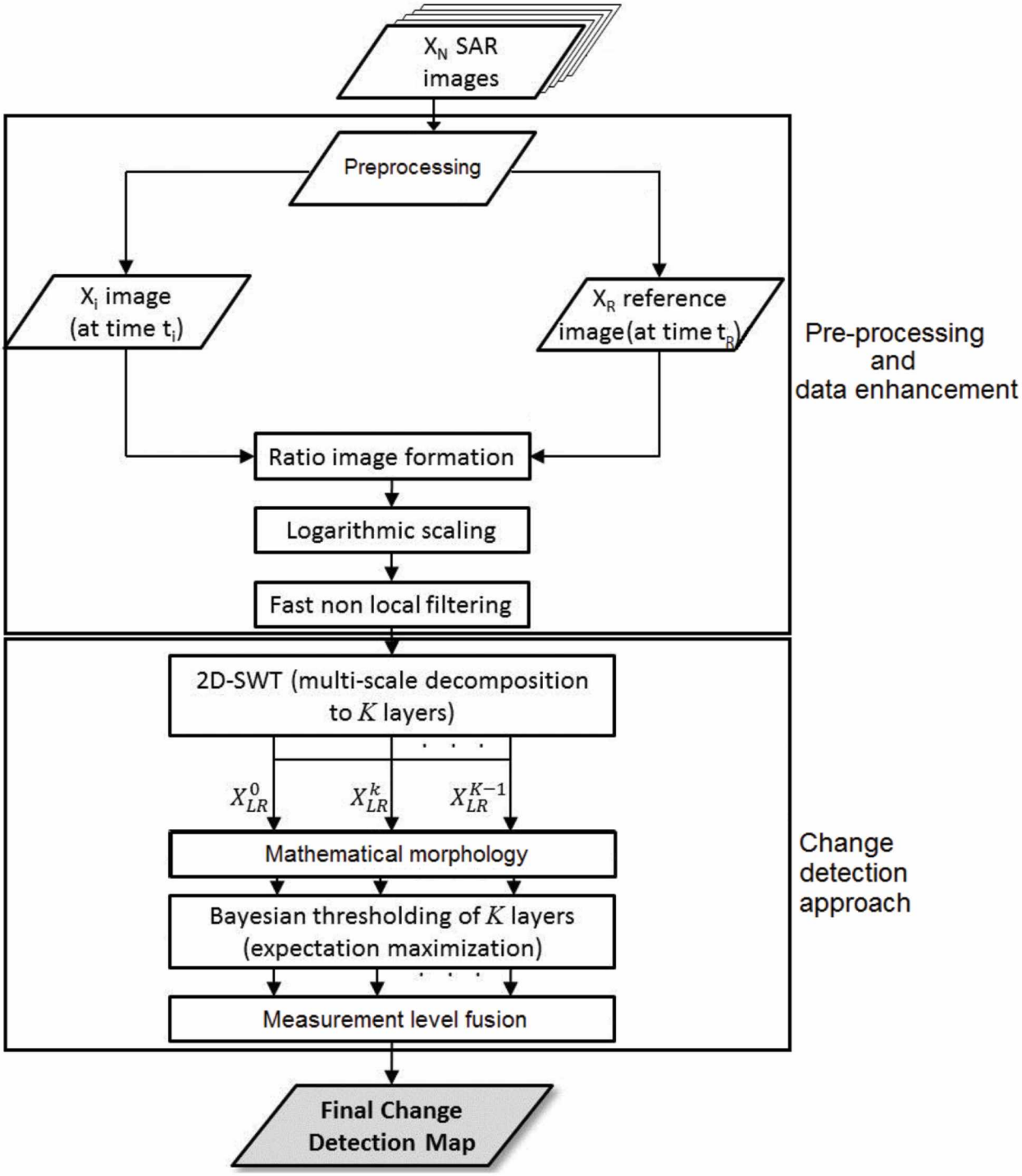

Figure 3.1. Workflow of the proposed approach. Here, $\mathbf{X_{LR}^{0}}$ is the original log-ratio image, $\mathbf{X_{LR}^{k}}$ is the k^{th} decomposed image, and $\mathbf{X_{LR}^{K-1}}$ is the highest decomposed level.

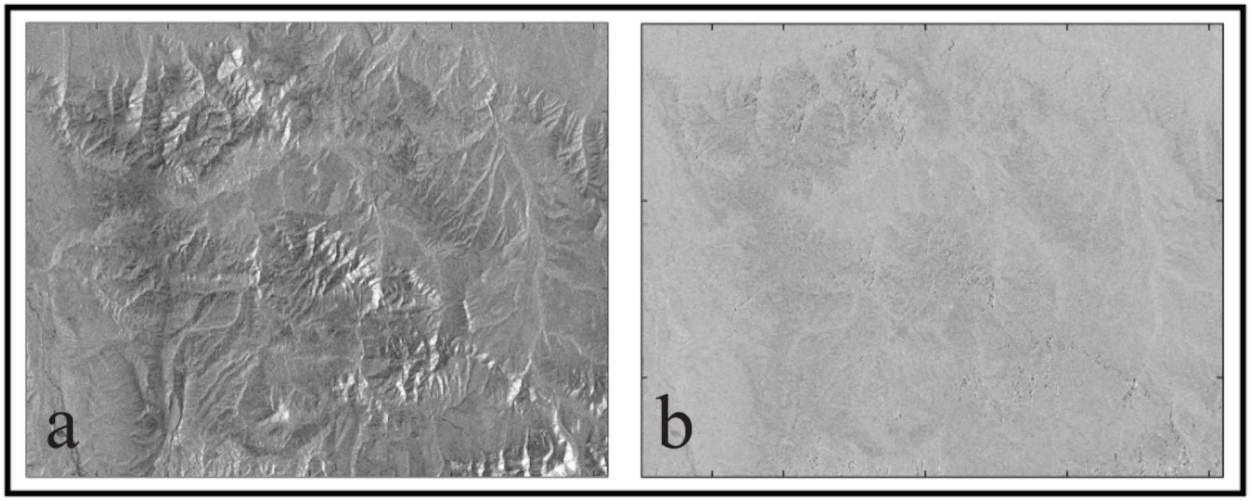

Figure 3.2. Example of (a) image affected by radiometric and geometric distortions; (b) radiometric and geometric normalized image enabling change detection analysis from multiple geometries.

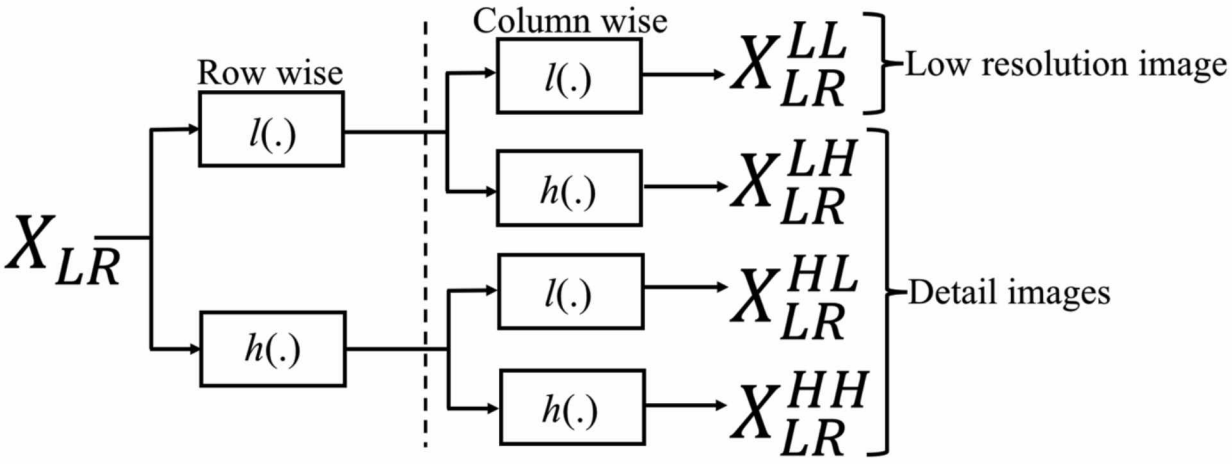

Figure 3.3. Multi-scale decomposition of input log-ratio image $\boldsymbol{X_{LR}}$ into a lower resolution and detail images; $\boldsymbol{X_{LR}^{LL}}$ is the lower resolution image and ($\boldsymbol{X_{LR}^{LH}}, \boldsymbol{X_{LR}^{HL}}, \boldsymbol{X_{LR}^{HH}}$) are the high frequency detail images, which captures horizontal, vertical and diagonal directions, respectively.

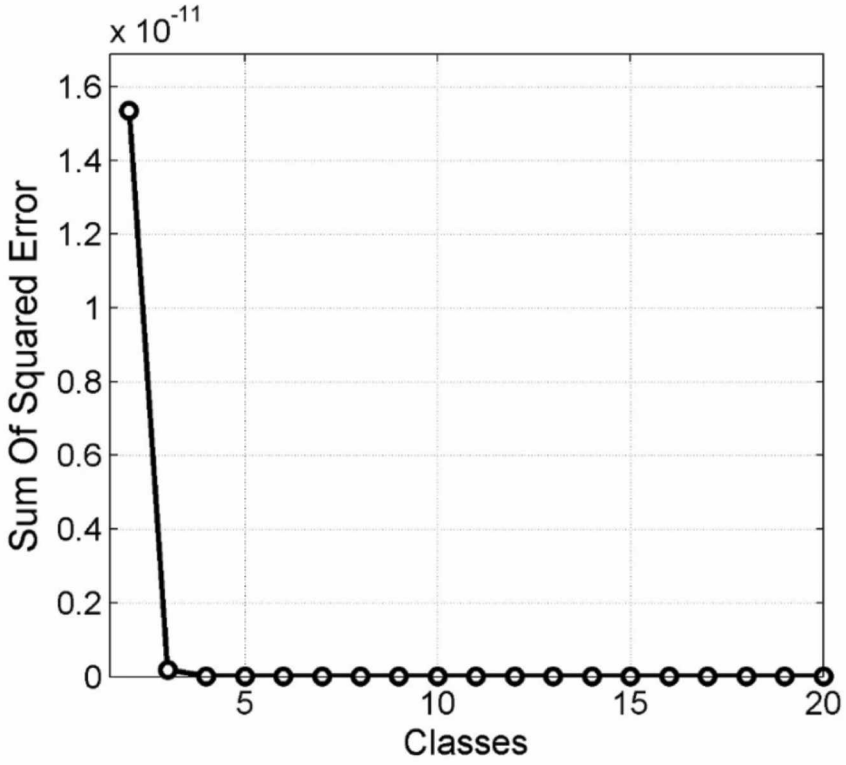

Figure 3.4. Selection of classes used for final classification.

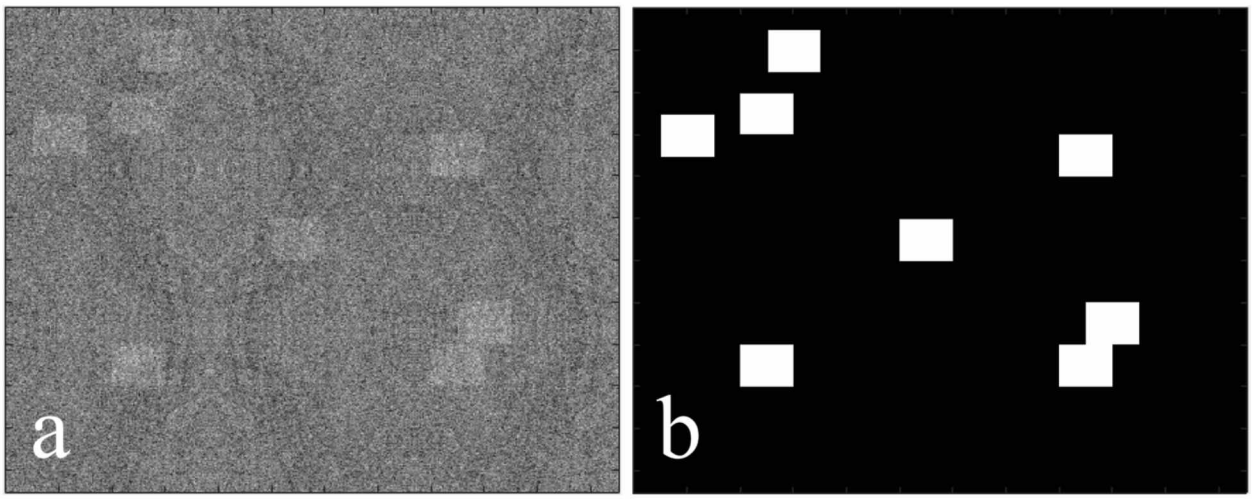

Figure 3.5. (a) Ratio image calculated from pre- and post-event images; (b) ground truth change map.

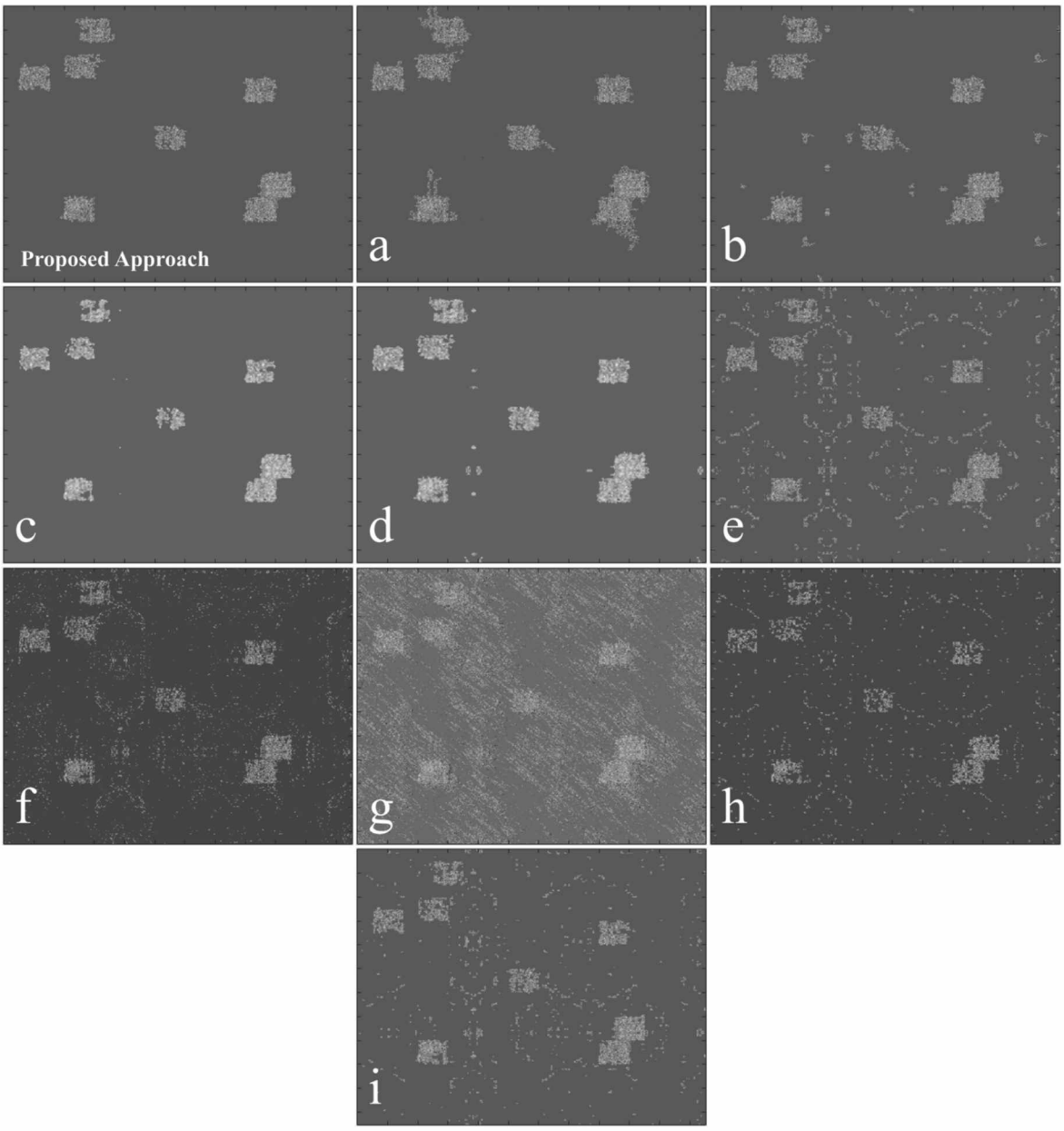

Figure 3.6. Change detection map showing: (a) proposed approach without fast non-local means filter; (b) proposed approach without 2D-SWT; (c) proposed approach without morphological filtering; (d) proposed approach without EM algorithm; (e) SVM approach; (f) image denoising using fast discrete curvelet transform via wrapping with EM algorithm; (g) FFL_ARS approach; (h) DT-CWT with intra- and inter-scale data fusion approach; (i) UDWT with Chan–Vese active contour model approach.

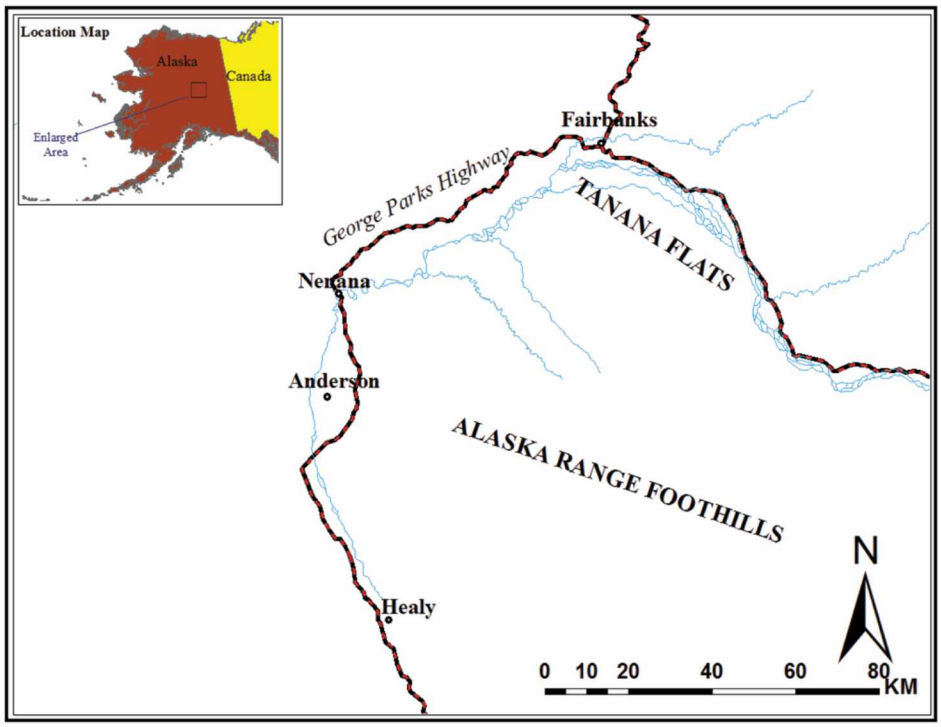

Figure 3.7. Study area for wildfire mapping.

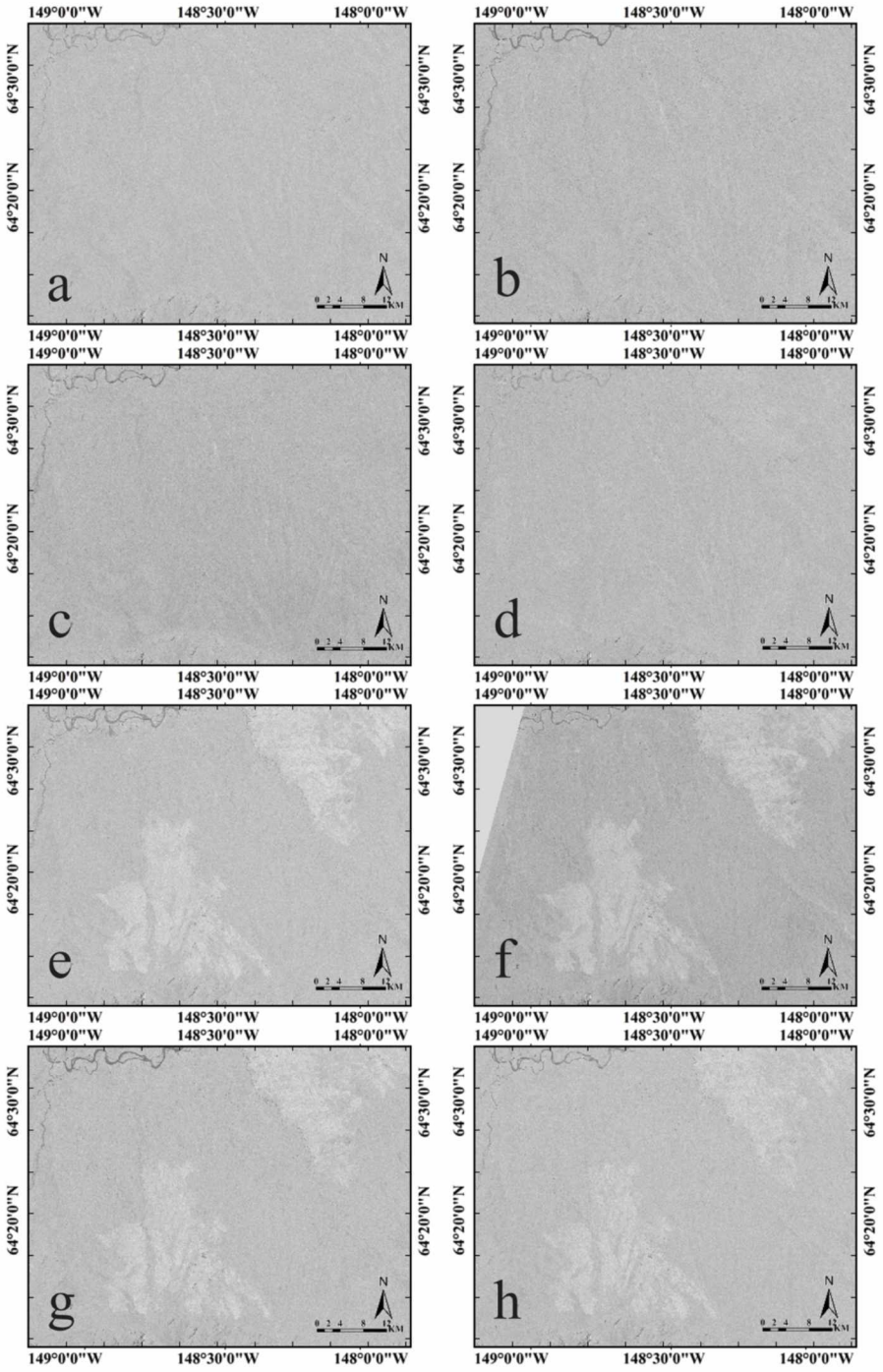

Figure 3.8. Pre-fire image acquired on: (a) 21 June 2000; (b) 6 June 2001; (c) 23 October 2002; (d) 13 April 2004. Post-fire image acquired on: (e) 3 August 2001; (f) 7 October 2001; (g) 22 August 2002; (h) 6 June 2003. The triangular gray area in F denotes no data available.

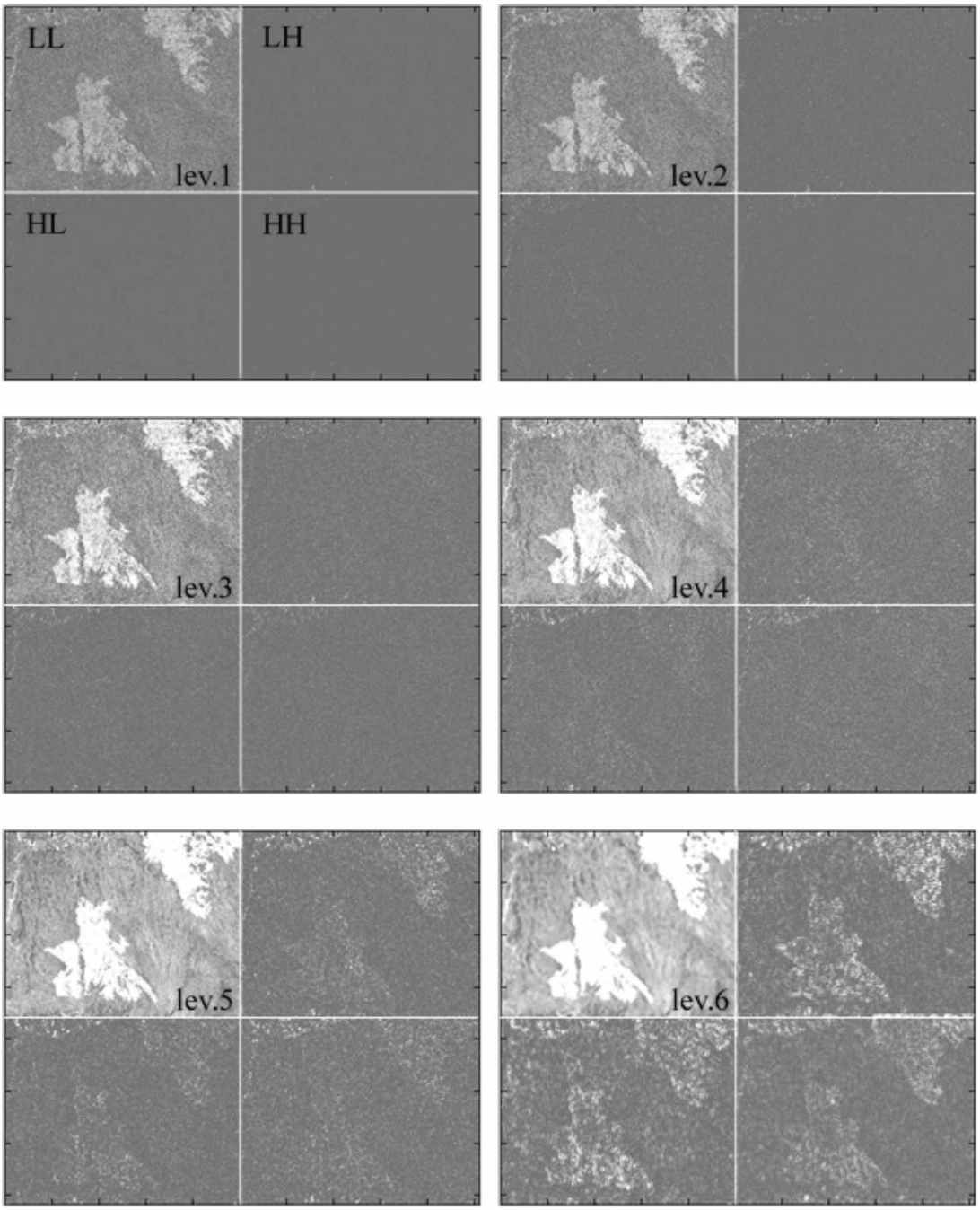

Figure 3.9. SWT decomposition of scenario 4 from level 1 to 6. Each level (level 1–6) of decomposition is showing the lower resolution (LL) image (top left) and the three detail (high frequency) images (LH, HL, HH). Level 0 is the original SAR image.

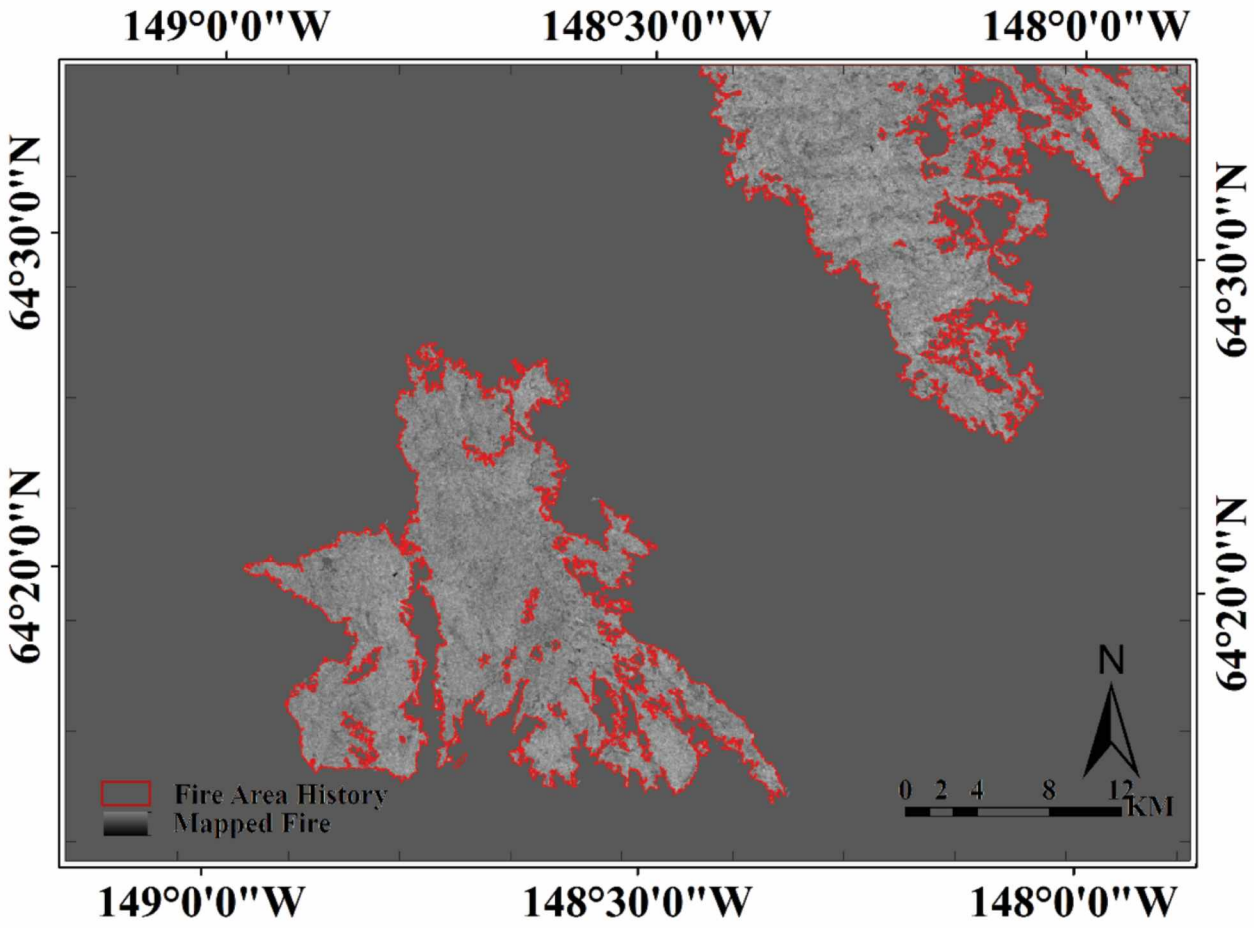

Figure 3.10. Overlay of the change detection map resulting from product rule fusion applied to scenario 4 with fire area history.

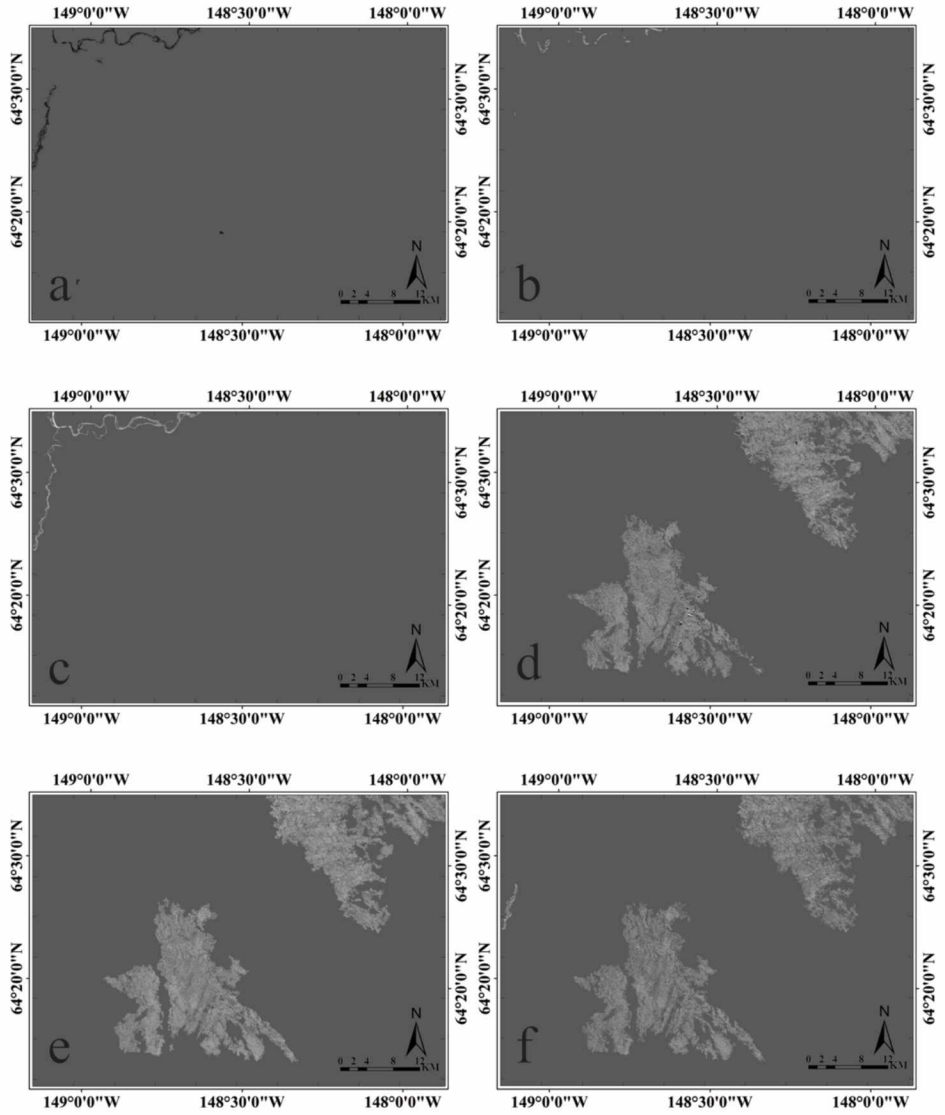

Figure 3.11. Change detection map resulting from product rule fusion applied to (a) scenario 1; (b) scenario 2; (c) scenario 3; (d) scenario 5; (e) scenario 6; (f) scenario 7.

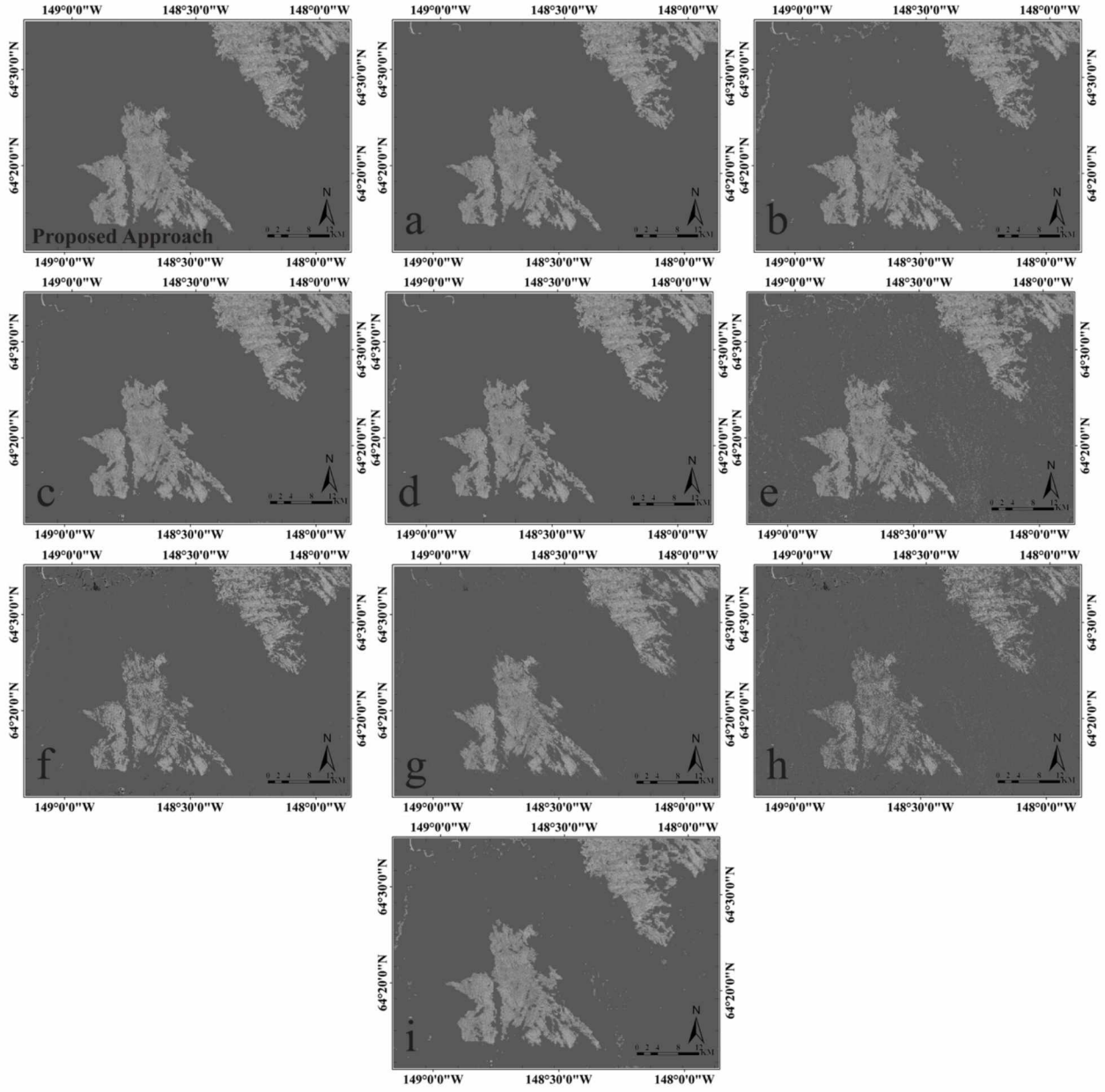

Figure 3.12. Change detection map showing: (a) proposed approach without fast non-local means filter; (b) proposed approach without 2D-SWT; (c) proposed approach without morphological filtering; (d) proposed approach without EM algorithm; (e) SVM approach; (f) image denoising using fast discrete curvelet transform via wrapping with EM algorithm; (g) FFL_ARS approach; (h) DT-CWT with intra- and inter-scale data fusion approach; (i) UDWT with Chan–Vese active contour model approach.

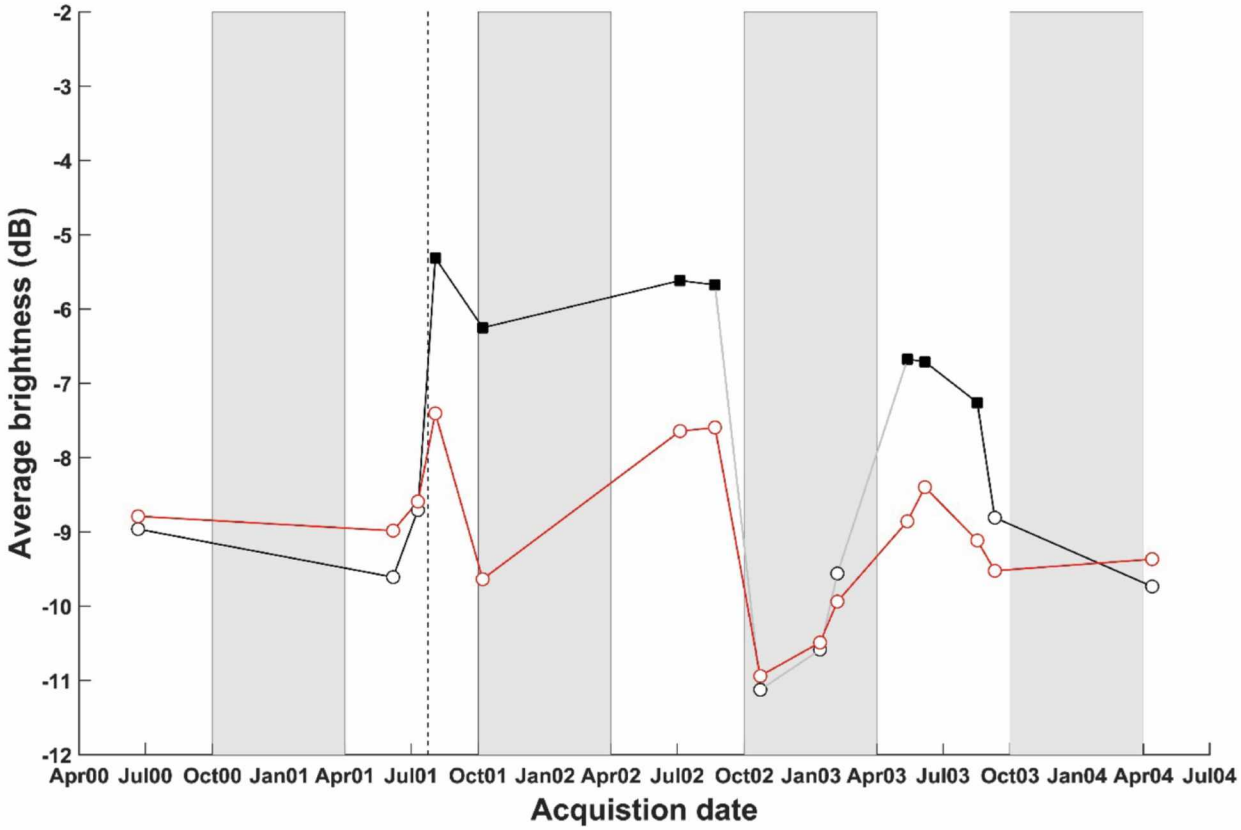

Figure 3.13. Time series showing fire scar area plotted over time (black line) and an area not affected by fire plotted over time (red line). The gray line represents a fire scar that cannot be seen as a result of snow cover. The circle symbol on each line indicates an area with no fire, while the square symbol indicates a fire scar area. The gray shaded box area indicates winter months, and the dashed line denotes when the fire started.

Table 3.1. Overall accuracy, overall error, kappa coefficient, false positive and false negative of the measurement level fusion using Figure 3.5a.

	Overall Accuracy (%)	**Overall Error (%)**	**Kappa Coefficient**	**False Positive (%)**	**False Negative (%)**
Product rule fusion	98.973	1.035	0.906	0.361	11.532
Sum rule fusion	98.941	1.058	0.904	0.380	11.626
Max rule fusion	98.952	1.042	0.905	0.365	11.582
Min rule fusion	67.256	32.743	0.157	34.076	11.972
Majority voting rule fusion	98.826	1.173	0.891	0.340	14.157

Table 3.2. Overall accuracy, overall error, kappa coefficient, false positive and false negative of our proposed approach with alternative methods using Figure 3.5a.

	Overall Accuracy (%)	**Overall Error (%)**	**Kappa Coefficient**	**False Positive (%)**	**False Negative (%)**
Proposed approach	98.973	1.035	0.906	0.361	11.532
Method A	98.038	1.961	0.844	1.843	3.806
Method B	98.024	1.975	0.827	1.127	15.201
Method C	98.352	1.648	0.836	0.109	25.622
Method D	98.647	1.353	0.878	0.694	9.942
Method E	93.583	6.416	0.575	5.708	17.453
Method F	94.763	5.236	0.594	3.741	28.547
Method G	68.412	31.587	0.162	32.773	13.101
Method H	94.527	5.473	0.519	2.953	44.750
Method I	95.549	4.450	0.659	3.409	20.678

Table 3.3. Combination of image acquisitions used to generate the ratio images.

Image 1 (X1)	Image 2 (X2)	Scenarios	Change	Figure
21 June 2000	6 June 2001	scenario 1	Negative	3.11a
6 June 2001	23 October 2002	scenario 2	Negative	3.11b
6 June 2001	13 April 2004	scenario 3	Negative	3.11c
6 June 2001	3 August 2001	scenario 4	Positive	3.10
6 June 2001	7 October 2001	scenario 5	Positive	3.11d
6 June 2001	22 August 2002	scenario 6	Positive	3.11e
6 June 2001	6 June 2003	scenario 7	Positive	3.11f

Table 3.4. Incidence angle of all the individual image acquisitions.

Image Acquisitions	Incidence Angle
21 June 2000	27.207°
6 June 2001	27.238°
23 October 2002	33.736°
13 April 2004	27.375°
3 August 2001	27.236°
7 October 2001	22.796°
22 August 2002	27.296°
6 June 2003	27.336°

Table 3.5. Overall accuracy, overall error, kappa coefficient, false positive and false negative of the measurement level fusion using scenario 4.

	Overall Accuracy (%)	**Overall Error (%)**	**Kappa Coefficient**	**False Positive (%)**	**False Negative (%)**
Product rule fusion	99.932	0.067	0.997	0.021	0.269
Sum rule fusion	98.991	1.008	0.967	0.653	2.543
Max rule fusion	97.609	2.390	0.924	2.476	2.020
Min rule fusion	98.273	1.726	0.944	1.815	1.342
Majority voting rule fusion	98.842	1.158	0.961	0.417	4.359

Table 3.6. Overall accuracy, overall error, kappa coefficient, false positive and false negative of our proposed approach with alternative methods using scenario 4.

	Overall Accuracy (%)	Overall Error (%)	Kappa Coefficient	False Positive (%)	False Negative (%)
Proposed approach	99.932	0.067	0.997	0.021	0.269
Method A	98.402	1.597	0.946	0.172	7.761
Method B	97.823	2.176	0.927	0.797	8.144
Method C	97.963	2.036	0.932	0.713	7.754
Method D	97.550	2.450	0.916	0.248	11.972
Method E	93.816	6.183	0.808	5.526	9.021
Method F	93.054	6.945	0.745	1.105	32.206
Method G	94.986	5.013	0.830	3.964	4.659
Method H	89.078	10.921	0.605	3.959	41.035
Method I	96.587	3.412	0.891	2.887	5.681

Chapter 4 Oil Spill Detection in Synthetic Aperture Radar Images using Lipschitz-Regularity and Multiscale Techniques [1]

4.1. Abstract

This research adapts an effective change detection approach originally applied to mapping fire scar from a stationary Synthetic Aperture Radar (SAR) scene to the problem of oil spills from SAR data. The method presented here combines several advanced image processing techniques to mitigate some of the common performance limitations of SAR-based oil spill detection. Principally among these limitations are: (1) the radar cross section of the areas affected by an oil spill strongly depends on wind and wave effects and is therefore highly variable; and (2) the radar cross section of oil covered water is often indistinguishable from other dark ocean features such as low wind areas, which leads to errors and uncertainties in oil spill detection. In this paper, we introduce a multi-image analysis, the Lipschitz regularity (LR), and wavelet transforms as a combined approach to mitigate these performance limitations. We show that the LR parameter is much less sensitive to variations of wind and waves in an oil spill SAR imagery, lending itself well for normalizing and suppressing ocean background using image ratio processing. Beyond its benefit for image normalization, we also show that the LR transform enhances contrast between oil-covered and oil-free ocean surfaces and therefore improves spill detection performance. We combine LR processing with a multi-scale technique based on the wavelet transform to additionally achieve high quality noise suppression without losing relevant image details. Bayesian thresholding based on expectation maximization techniques is used to achieve high levels of automation in oil spill detection. To describe the performance of this approach under controlled conditions, we applied our method to simulated SAR data of wind driven oceans with oil spills and low wind areas. We also applied our method to several real-

world oil spill data, using a series of images from the Phased Array L-band Synthetic Aperture Radar (PALSAR), and from X-band TerraSAR-X sensors, acquired during the 2010 Deep Water Horizon spill in the Gulf of Mexico. From our analysis, we concluded that both LR and wavelet transforms have led to high oil spill detection performance even during unfavorable wind conditions.

---

[1] Ajadi, O.A.; Meyer, F.J.; Marivi, T.; Giuseppe, R (2017), Application of Lipschitz Regularity and Multiscale Techniques for the Detection of Oil Spill in Synthetic Aperture Radar Imagery. Prepared for submission to *IEEE Journal of Selected Topics in Applied Earth Observations and Remote Sensing* 2017.

4.2. Introduction and Background

Marine pollution caused by oil spills -- the release of petroleum hydrocarbons -- poses a major threat to marine environments (Marghany, 2015). To minimize the effects caused by an oil spill, it is important to identify the source, extent, and progression of the spill. In recent years, researchers have focused their efforts on using satellite sensors to detect oil spills once they occur. Although various types of orbiting sensors have been used for this purpose, imaging with Synthetic Aperture Radar (SAR), multi-band optical cameras (Puestow et al., 2013), and infrared sensors (Yu et al., 2017) are the most common.

SAR data are gaining increasing importance as a critical tool to assist in monitoring oil spills, due to their day-and-night and all-weather imaging capabilities (Garcia-Pineda et al., 2013). For example, ERS-1/2 SAR images were used to monitor oil spills in the Caspian Sea, eastward of Apsheron Peninsula in May of 1996 (Ivanov and Ermoshkin, 2004). The areal extent of the Prestige wreck in 2002 near the Spanish coast was mapped by ENVISAT Advanced SAR

(ASAR) (Fortuny et al., 2004; Mercier and Girard-Ardhuin, 2006; Palenzuela et al., 2006). RADARSAT-1 was used for classifying and detecting oil slicks for the Nakhodka fuel oil spill in the Sea of Japan in 1997 (Hodgins et al., 1996) while RADARSAT-2 data were used for oil spill detection after the 2010 Deepwater Horizon Blowout in the Gulf of Mexico (Marghany, 2015). Additionally, Phased Array-type L-band Synthetic Aperture Radar (PALSAR) sensor data were employed for oil slick observation after the accident of the Solar 1 tanker, about 24 km off the southern coast of Lusaca Point, Guimaras Island of the Philippines in 2006 (Migliaccio et al., 2009) while TerraSAR-X data were used for emergent oil spill monitoring after the Hebei Spirit oil spill incident that occurred on the west coast of the Korean Peninsula in 2007 (Kim et al., 2010). In this paper, we will make use of PALSAR and TerraSAR-X data.

SAR backscattering from bodies of water is heavily determined by small surface waves called gravity-capillary waves, which induce surface roughness. The presence of oil dampens the gravity-capillary waves by reducing surface tension. This makes areas affected by the spill appear smoother than wind-roughened ocean not covered by oil. In a SAR image, these areas will be darker relative to wind-roughened clean ocean surfaces. Areas affected by oil are not the only dark patches in a SAR image, however. Similar darkened patches in a SAR image can be caused by grease ice, low wind conditions (< 2 m/s), rain cells, internal waves, upwelling and downwelling zones (Hovland et al., 1994). These patches (e.g. low wind areas) are known as look-alikes, and their similarity to oil spills is a major problem in SAR-based oil spill detection.

4.2.1. State-of-the-Art in Amplitude-Based Oil Spill Detection

Over the years, several approaches have been developed to discriminate oil spill and look-alikes from the ocean surface and they are described here. In Solberg et al. (1999) an unsupervised semiautomatic system for oil spill detection was developed by combining a

statistical model with a rule-based modification of prior probabilities, such that objects with a high probability of being oil slicks are automatically identified. In the work done by Nirchio et al. (2005), a supervised approach using multiple linear regression was used to identify oil spills and a supervised approach based on support vector machine (SVM) for oil spill classification was employed by Brekke and Solberg, (2008) while in Moctezuma and Parmiggiani, (2014) an unsupervised binary segmentation scheme based on the Markov random field theory was utilized for oil spill detection . In Mercier and Girard-Ardhuin, (2006), a semi-supervised oil-slick detection was presented by using a kernel-based abnormal detection into the wavelet decomposition of a SAR image while according to Marghany and Van Genderen, (2001), supervised texture algorithms were used for automatic detection of oil spills in a RADARSAT-1 SAR image. Fractal geometry for texture analysis based on an unsupervised approach was employed in a multi-resolution algorithm (Benelli and Garzelli, 1999). Artificial supervised neural network (ANN) approaches to detect dark formations and to discriminate oil spills from look-alikes were introduced in Frate et al. (2000) and Topouzelis et al. (2007).

More recently, Shu et al. (2010) developed an automated dark-spot detection using SAR intensity imagery. The approach used spatial density feature to differentiate between dark spots and the background. Intensity threshold segmentation was applied first to differentiate potential dark-spot pixels from potential background pixels. The density of potential background pixels was then estimated using kernel density estimation to determine real dark-spot pixels. In the last step, an area threshold and a contrast threshold were employed to eliminate any remaining false targets. In Garcia-Pineda et al. (2013) a supervised Textural Classifier Neural Network Algorithm (TCNNA) to process SAR data to map oil spills was developed. Their algorithm processes wind model outputs (CMOD5) and SAR data using a combination of two neural

networks. An oil spill segmentation method was presented by Ren et al. (2016) that coupled two smoothing modules at the label and the pixel levels to accurately characterize oil spill structures. The integration of their two smoothing modules was referred to as dual smoothing. At the label level, Ren et al. (2016) employed the rolling guidance filter, which smoothens the label cost volumes and hence alleviates the ambiguous segmentation that blurs the oil spills structure. At the pixel level, Ren et al. (2016) employed the cooperative model which smoothens the higher order pixel variations, and henceforth preserves the elongated strips of the oil spill. In Xu et al. (2016), a detection algorithm was developed which utilized a stochastic fully connected continuous conditional random field (SFCCRF) approach to model SAR imagery and perform soft- label inference. Xu et al. (2016) did not treat all the pixel in an image as being connected, but instead used the SFCCRF approach in a stochastic manner to determine the connectivity of two pixels based on their proximity in both image space and feature space. Moreover, Xu et al. (2016) used the SFCCRF approach to model SAR image and to perform soft-label inference, which led to an efficient dark-spot detection that can discriminate between dark spot and the background. Taravat and Oppelt, (2014) utilized a neural network model, which adopts the Weibull multiplicative filter to suppress speckle noise and thereby enhancing the contrast between the background and the targets. In addition, they used the multilayer perceptron (MLP) neural networks to segment the speckle suppressed SAR image. Singha et al. (2016) developed an oil spill processing chain which utilized coherent dual-polarimetric (copolarized channels, i.e., HH- VV) TerraSAR-X images. The method combined traditional and polarimetric features for object- based oil spill detection and look-alike discrimination. The extracted features are divided into training and validation dataset., which are used as input for a support vector machine-based classifier (Singha et al., 2016), while in Salberg et al. (2014), the structure of the compact

polarimetry CL-mode data was used to derive a new feature that has the ability of suppressing look-alikes caused by low wind.

In Section 4.5.4, we will compare a few of the state-of-the-art amplitude based oil spill change detection approaches mentioned above with our adapted approach to evaluate its performance.

4.2.2. Requirement of Current Remote Sensing-Based Oil Spill Detection Techniques

While a range of SAR-based approaches have been developed in the past, in this paper, we are focusing our attention exclusively on techniques using SAR amplitude data and will not discuss techniques based on other forms of SAR data, e.g., polarimetric. This choice is motivated by our goal to develop a technique that can be applied broadly to every incoming SAR image to warrant oil spill tracking with high temporal resolution. This is difficult to achieve by techniques based on polarimetric information, as the required polarimetric information is only available for a fraction of all possible SAR images.

For many spill detection techniques that are using SAR amplitude data, the two most important characteristics driving the performance of oil spill detection are wind speed at the ocean surface and the nature of the slick. Based on analyses from previous researchers (such as Gade and Redondo, 1999; Garcia-Pineda et al., 2013; Girard-Ardhuin et al., 2005; Lu et al., 2000; Solberg and Volden, 1997), optimal conditions for oil spill detection exist for wind speeds from 3 m/s to 10-14 m/s while the shape of a spill was found to be important when discriminating between oil spills and look-alikes (Topouzelis, 2008).

To reduce the sensitivity of oil spill detection to surface winds and improve detection performance at the low wind speed end, we have adapted an effective change detection approach that we have previously published in Ajadi et al. (2016), to present a combined Scale-space

LIpschitz-based Change tracKing (SLICK) approach which consists of a normalization step, a data enhancement and filtering step, and the application of the multi-scale oil spill change detection technique. The properties of the adapted algorithm and their relationship to the task of oil spill detection are as follows:

1. Instead of the original amplitude data, we now utilize a local image structure parameter called Lipschitz Regularity (LR) in our adapted change detection approach (Tello et al., 2007). We will show that LR, which is derived from the original image data, is less dependent of surface wind speed and, hence, reduces the dependence of spill detection on local wind conditions. We will also demonstrate that LR improves the separation between oil-free and oil-covered image pixels, leading to an improved detection performance.

2. In contrast to most other techniques, we utilized the concept of multi-scale analysis (Ajadi et al., 2016) to the application of SAR-based oil spill detection. Previous research (Ajadi et al., 2016; Celik, 2010; Hou et al., 2014) has demonstrated the effectiveness of image ratioing for suppressing stationary image background and improving the detectability of an object of interest. As the radar cross section of the ocean background is typically not stable, we are utilizing the capabilities of the LR transform, which reduces the sensitivity of ocean backscatter to surface winds (Tello et al., 2007), to allow us to normalize the radiometric response of the ocean background and enhance the contrast between oil-covered and oil-free ocean surfaces.

To improve oil spill detection performance, we utilize modern techniques for the treatment of speckle, a multiplicative noise-like signal typically associated with SAR images. The process of removing the speckle noise was adapted from Ajadi et al. (2016) and involves the use of modern non-local filtering methods to effectively suppress noise whilst preserving most relevant

image details, and removing the residual noise by performing a multi-scale decomposition to generate image instances with varying resolution and signal-to-noise ratio.

As an additional important feature, we improve the accuracy of the oil spill detection by introducing a reliable scale selection technique into our workflow. We analyze the reliability of each image pixel at different resolution level. A pixel is said to be reliable if it belongs to a homogeneous area. After identifying at which scale each image pixel is reliable, we model the probability density function (PDF) of the preprocessed data (LR-transform, image ratioing, and noise filtering) as a mixture of Gaussian distributions (one representing background and one representing the oil spill) and use Bayesian inferencing methods with expectation maximization (EM) for their automatic separation. After separation, we then fuse the decisions made at the various levels using an "optimal" scale selection approach (Bovolo and Bruzzone, 2005). In the paper, we provide details on our implemented method and briefly address the appropriateness of using a mixture of Gaussian distributions to represent the PDF of our preprocessed data.

The details of our adapted approach are described in Section 4.3. A performance assessment using a synthetic dataset and a real application to oil spill mapping is shown in Sections 4.4 and 4.5, respectively. A summary of the presented work is shown in Section 4.6.

4.3. Oil Spill Detection Methodology

The work presented here is motivated by the challenges associated with oil spill detection and the desire to produce an improved and near-automatic algorithm for unsupervised oil spill detection in SAR images. Our approach focuses on using LR's to normalize and enhance the contrast between oil-covered and oil-free ocean surfaces. We also modified our change detection techniques, see Ajadi et al. (2016) for the originally published technique, for background suppression and are using information at different resolution levels to obtain high accuracy oil

spill change detection maps in both heterogeneous and homogeneous regions. To achieve this goal, a LR estimation step (Figure 4.1) followed by a modified multi-image processing workflow are presented (Figure 4.2). The individual processing steps of our updated change detection approach are explained in the following sub-sections.

4.3.1. Normalizing Ocean Backscatter through Lipschitz-Regularity Estimation

Previous research has shown that texture transforms such as LR estimation are effective processes for normalizing ocean clutter and improving the detectability of objects on oceans (Tello et al., 2007). This statement is based on the finding that the local regularity of the ocean backscatter (in contrast to the backscatter itself) is less dependent on environmental conditions such as surface wind. Hence, calculation of the local regularity of a signal lends itself for clutter normalization. The LR is an effective measure of the local regularity of the intensity function associated with a SAR image. In the following section, we present an efficient method for calculating LR based on two-dimensional continuous wavelet transform (2D-CWT).

4.3.1.1. Two-Dimensional Continuous Wavelet Transform

The 2D-CWT has several advantages over other multi-scale time-frequency methods, because it provides high flexibility, and has been successfully used in the estimation and detection of abrupt changes in non-stationary environments (Hambaba, 2000). In this section, the 2D-CWT is discussed to the extent needed in the context of LR estimation. Further details on 2D-CWT can be found in Mallat, (1999).

The 2D-CWT can be defined as the projection of a complex signal in a function space, such that the functions are localized in both time and frequency (Tello et al., 2007). Given a function $\psi(t)$ which satisfies the condition:

$$\int_{-\infty}^{\infty} \psi(t)dt = 0 \tag{4.1}$$

centered at $t = 0$ and with unity power, the function $\psi_{u,s}(t)$ can be expressed as:

$$\psi_{u,s}(t) = \frac{1}{\sqrt{s}}\psi\left(\frac{t-u}{s}\right) \tag{4.2}$$

where u is the translation parameter, and s is the dilation parameter. The function $\psi(t)$ in (4.1) is the mother wavelet, while the functions $\psi_{u,s}(t)$ are the family of wavelets resulting from translations and dilations of the mother wavelet (Mallat, 1999). The CWT of a signal, $f(t)$, is defined as:

$$wf(u,s) = \int_{-\infty}^{\infty} f(t)\frac{1}{\sqrt{s}}\psi^*\left(\frac{t-u}{s}\right)dt \tag{4.3}$$

given $f \in L^2(\mathbb{R})$, where * signifies conjugate. Moreover, CWT can be viewed as filtering of $f(t)$ using the dilated band-pass filters whose impulse response is given by the wavelet functions. To estimate LR using 2D-CWT, the mother wavelet $\psi(t)$ used in the decomposition must have more than two vanishing moments. One wavelet that satisfies this requirement is the Gaussian wavelet whose n^{th} derivative has N-vanishing moments. We utilize the second derivative of a Gaussian wavelet (also known as a Mexican hat wavelet) in our approach. It is worth mentioning that the 2D-CWT is carried out in the Fourier space, and the Mexican hat mother wavelet is expressed as:

$$\hat{\psi}(\omega) = \frac{-\sqrt{8}\sigma^{\frac{5}{2}}\pi^{\frac{1}{4}}}{\sqrt{3}}\omega^2 exp\left(\frac{-\sigma^2\omega^2}{2}\right) \tag{4.4}.$$

where σ is a scale factor. In this paper, we employed a 2D-CWT. For more information on the 2D-CWT, the reader is referred to Wang and Lu, (2010).

4.3.1.2. Estimation of Lipschitz Regularity Using 2D-CWT

The objective of estimating the LR is to provide an accurate estimate of the local regularity of a signal, which, in our case, reflects the local roughness of the observed SAR sea clutter (Tello et al., 2007). By definition (Tello et al., 2007), a function f is pointwise Lipschitz $\alpha \geq 0$ at point v, if there exists a constant $K > 0$, and a polynomial p_v of degree $m = \lfloor \alpha \rfloor$ such that $\forall t \in \mathbb{R}$,

$$|f(t) - p_v(t)| \leq K|t - v|^{\alpha} \quad (4.5).$$

If $0 \leq \alpha < 1$ then $p_v(t) = f(v)$ and the Lipschitz condition becomes:

$$|f(t) - f(v)| \leq K|t - v|^{\alpha} \quad (4.6)$$

Assuming a wavelet ψ has N vanishing moments, and if f is uniformly Lipschitz $\alpha \leq N$ over $[a, b]$, then there exists $A > 0$ such that $\forall (u, s) \in [a, b] \times \mathbb{R}^+$,

$$log|wf(u, s)| \leq log\, A + \left(\alpha + \frac{1}{2}\right) log\, s \quad (4.7)$$

The LR (α in Equation (4.7)) of the signal is related to the decay of the 2D-CWT amplitude across spatial scales. In this paper, we employed the Gradient Modulus Wavelet Projection (GMWP) method (Turiel et al., 2006) to estimate LR over the standard modulus maxima method because the GMWP method produces a dense representation of the image analyzed. Computing the GMWP involves the wavelet decomposition of the modulus of the gradient of the image analyzed (Turiel et al., 2006), or

$$log(w|\nabla f(u, s)|) \propto \alpha\, log\, S \quad (4.8)$$

where $\nabla f(u, s)$ is the gradient of function and $w|\nabla f(u, s)|$ is its 2D-CWT. The measure of the LR α can be interpreted as the maximum slope of the logarithmic transform of the wavelet coefficients at point u across scales.

As stated in Section 4.3.1, the estimation of local regularity of the ocean backscatter (in contrast to the backscatter itself) is less dependent on surface wind. If LR α is conceptually interpreted as the slope of the local image power spectrum (Figure 4.3), this is because variations of wind speed mostly modify the intercept of the power spectrum (see high wind (P_{HW}) and low wind (P_{LW}) power in Figure 4.3) while the presence of oil changes slope α. The importance of LR in our paper is demonstrated in Section 4.5.3, where Figure 4.13 shows its effectiveness for ocean background normalization. It is noticeable in Figure 4.13 that in the LR-transformed data, oil-covered ocean water is more emphasized against a now normalized ocean background. Also, examining the PDF's in Figure 4.13, it is evident that in the LR space, the background and target PDF's of ocean versus oil spill are more distinct from each other and therefore easier to separate. After the LR was calculated for all SAR images, the next step is to perform data enhancement (Figure 4.2).

4.3.2. Data Enhancement

4.3.2.1. Ratio Image Formation and Fast Non-Local Means Filtering Approach

As the ocean background is largely normalized after LR transformation, we can now apply logarithmic ratio image formation between a post-event (after an oil spill) LR image (X_i) and a pre-event (before an oil spill) LR image (X_R) to effectively suppress ocean background and enhance the visibility of oil spill features. The pre-event images can be selected at any day, time, and location provided the image is a free ocean surface without any oil spill. Selection at any day, time, and location does not affect our approach because of the continuous nature of the ocean surface, and because all the images had undergone LR transformation. The resulting logarithmic ratio image is modeled as (Ajadi et al., 2016):

$$X'_{LS} = 10\log(x) + 10\log\left(\frac{X_i(i,j)}{X_R(i,j)}\right) \tag{4.9}$$

where X'_{LS} is the log-scaled ratio image and x is an additive speckle noise contribution. To perform a first-order suppression of the additive noise component, we apply a fast non-local mean filtering procedure that results in the filtered ratio image X_{LS}. Fast non-local mean filters suppresses noise without degrading spatial resolution (Buades et al., 2005). Our implementation of the fast non-local mean filtering procedure follows the approach of Ajadi et al. (2016) and more details can be found therein. After estimating X_{LS}, we are ready to apply our adapted multi-scale oil spill change detection technique.

4.3.3. Oil Spill Change Detection Technique

The oil spill change detection approach is shown in the lower frame of the workflow in Figure 4.2 and includes four key elements. The first step consists of a multi-scale decomposition of the input ratio images using an UDWT, resulting in K image instances that are all analyzed for spill detection. To facilitate optimal change detection in every pixel, we decompose the input log-scaled ratio image into a multi-scale image pyramid, where each scale is characterized by a different tradeoff between speckle noise suppression and image details. To this end, the wavelet transform is expressed as a multi-scale differential operator utilizing a wavelet $\psi(t)$ with n vanishing moments. The multi-scale representation of X_{LS} is obtained by applying an UDWT to create $X_{MS} = \{X_{LS}^0 .., X_{LS}^k \dots\dots\dots.., X_{LS}^{K-1}\}$. For more information on multi-scale decomposition, the reader is referred to Mallat, (1999).

In a second step, a separate image classification is performed at each of the K levels of the multi-scale data, resulting in K classification results per pixel. In our approach, the classifications

are performed automatically and adaptively using an Expectation-Maximization (EM) algorithm supported by mathematical morphology filtering following the approach of Ajadi et al. (2016). In a third step, we determine for every pixel, which of the multi-scale classification results can be considered reliable and therefore should be considered when determining the final classification result. As will be shown in Section 4.3.3.2, a decision on the reliability of a classification at a specific spatial scale can be made based on image context. Finally, in a fourth step, we conduct a scale-driven fusion of all "reliable" classification results to result in a final detection mask for a targeted spill event.

4.3.3.1. Classification by Expectation-Maximization (EM) with Mathematical Morphology

Following our previous work in Ajadi et al. (2016), after the images have been decomposed into the multi-resolution set X_{MS}, each decomposed image undergoes mathematical morphology processing to simplify a subsequent image classification. Please refer to Ajadi et al. (2016) for more information on the motivation behind applying mathematical morphology processing. Mathematical morphology defines a family of morphological filters, which are nonlinear operators, that aim at emphasizing spatial structures that are homogeneous in a gray level image (Ajadi et al., 2016). To retain the spatial structures in our image, we applied opening and closing by reconstruction, using a square shape structuring element of size 20. From an analysis of a broad range of data from different change detection projects we found (1) that a 20 x 20 pixel-sized structuring element of the morphological filter led to the most consistent results; and (2) that the oil spill change detection performance changed slowly with deviation from the 20-pixel setting. We applied our mathematical morphology following the approach is Ajadi et al. (2016),

and the new multi-scale decomposition X_{MD} stack now contained morphological filtered images at each level in X_{MS}, as below:

$$X_{MD} = \left\{X_{MD}^{0}.., X_{MD}^{k} \ldots\ldots\ldots.., X_{MD}^{K-1}\right\} \quad (4.10).$$

After the mathematical morphology step, we perform a separate image classification at each of the K resolution levels, resulting in K classification decisions per pixel. To automate the classification process, we employ an EM algorithm. According to Moon, (1996), the EM algorithm consists of two major steps: an expectation step followed by a maximization step. In our paper, the goal of the EM algorithm is to calculate the probability that a pixel belongs to a set of predefined classes, and every pixel is assigned to the class with the highest probability.

Assume an image y is the k^{th} level image in X_{MD}, we infer the class ($\omega_l = (\omega_c, \omega_u)$) that each pixel in y belongs to, with ω_c defining the oil spill class and ω_u corresponding to the ocean background. Using $\Theta^s = \left(\mu_{\omega_c}, \sigma^2_{\omega_c}, \mu_{\omega_u}, \sigma^2_{\omega_u}\right)$ as our current (best) estimate for the full distribution, such that mean μ_{ω_c} and variance $\sigma^2_{\omega_c}$ are sufficient to define the density function associated with the oil spill areas' ω_c, and mean μ_{ω_u} and variance $\sigma^2_{\omega_u}$ can be used to describe the density function related with the ocean background' ω_u. Given Θ as our improved estimate, the expectation step at s^{th} iteration is calculated by the conditional expectation:

$$\begin{aligned} Q(\Theta|\Theta^s) &= E[\text{In } P(\omega_l, y|\Theta|y, \Theta^s)] \\ &= \sum P(\omega_l|y, \Theta^s)\text{In } P(\omega_l, y|\Theta) \end{aligned} \quad (4.11).$$

The maximization step maximizes $Q(\Theta|\Theta^s)$ to acquire the next estimate:

$$\Theta^{(s+1)} = \underset{\Theta}{\text{argmax}}\, Q(\Theta|\Theta^s) \quad (4.12).$$

The iterations cease when the absolute differences between the previous and current variables are below a tolerance value (ε). In this paper, we empirically set the tolerance value ε to 10^{-6}. The higher the tolerance value, the faster the convergence and the lower the tolerance value, the slower the convergence. Once the iteration ceases, the final optimal $\Theta^{(s+1)}$ is used to calculate the posterior probability of the k^{th} level image in X_{MD}, using Bayes' formula. The EM algorithm is applied separately to all K levels of the multi-scale decomposition series, X_{MD}, resulting in a stack of posterior probability maps $PP_{MD} = \{PP^0, \ldots . PP^k, \ldots , PP^{K-1}\}$ of depth K. Each pixel in each posterior probability map (PP_{MD}) is assigned to the class with the highest probability resulting in the set of classification maps $\Delta_{bn} = \{\Delta^0, \ldots . \Delta^k, \ldots , \Delta^{K-1}\}$ of depth K using

$$\Delta_{bn}^k = \begin{cases} change, & if \quad \max_{i=0}^{K} \{PP^i\} \\ no - change, & otherwise \end{cases} \tag{4.13}$$

For more details about the EM algorithm, the reader is referred to Moon, (1996).

4.3.3.2. Selection of Reliable Scale

To obtain a change map with high accuracy across an entire image and independent of local image structure, we select a subset of resolution scales from all K scales that we consider "reliable" for the classification of a certain image pixel. The selection of reliable scales considers whether the pixel being analyzed belongs to a homogeneous area or a border area between features with different gray value (Figure 4.4).

As image resolution is reduced toward higher decomposition levels, the image information near border regions becomes more biased due to the mixing of neighboring homogeneous areas with different properties that are occurring in these areas (see Figure 4.4). Hence, data below an

acceptable "reliable" resolution scale cannot be used to analyze border area pixels to avoid unreliable (biased) classification results.

To express whether a pixel belongs to a homogeneous or heterogeneous (border) area at a given scale k, we calculate a multi-scale local coefficient of variation ($LCV^k(i,j) = \sigma^k(i,j)/\mu^k(i,j)$) and a global coefficient of variation ($CV^k = \sigma^k/\mu^k$) (Bovolo and Bruzzone, 2005), where $\mu^k(i,j)$ and $\sigma^k(i,j)$ are the local mean and local standard deviation at resolution level k and spatial position (i,j). A constant kernel of size 9 is utilized throughout all resolution levels. Low values of the LCV indicate homogeneous areas, while high values correspond to border areas. In the homogeneous area, a pixel is said to be reliable for that resolution level if the following condition is satisfied:

$$LCV^k(i,j) \leq CV^k \tag{4.14}.$$

At each resolution level, every pixel *(i, j)* that satisfies Equation (4.14) will be reliable and will have the form as shown below in Equation (4.15), with S_{ij} being the lowest resolution level that is considered reliable for pixel *(i, j)* and $X_{RS}^{R_{ij}}$ being the set of images with reliable scale:

$$X_{RS}^{R_{ij}} = \left\{X_{RS}^0 .., X_{RS}^k .., X_{RS}^{S_{ij}}\right\} \tag{4.15}.$$

4.3.3.3. Scale-Driven Fusion of all K Classification Results Per Image Pixel

In this step, we determine the final oil spill change detection (CD) map based on the set of K initial classification results $\left(\Delta_{bn}^k\right)$ as well as information about the reliable scale that was derived in Section 4.3.3.2. for each image pixel. To generate the CD map we employ fusion at the decision level by an "optimal" scale selection (Bovolo and Bruzzone, 2005). According to this approach, each pixel in CD is assigned to the class identified at the lowest reliable resolution

level of this pixel. The reliable scale with the lowest resolution is used as at this scale most of the noise was removed and the signal-to-noise ratio was maximized, i.e.:

$$CD(i,j) \in \omega_l \Leftrightarrow \Delta_{bn}^{S_{ij}}(i,j) \in \omega_l, with\ l = \{c,u\} \quad (4.16).$$

4.4. Performance Assessment Using Simulated Oil Spill Data

4.4.1. SAR Simulation of Ocean Surface Covered with Oil Spill

To assess the robustness of our oil spill detection approach under controlled conditions, we took advantage of an existing SAR image simulation concept published in Franceschetti et al. (2002). We generated simulated SAR images representing two frequency bands (L-band and X-band). In both oil spill situations, the ocean surface was generated by using a multiscale model in the simulator that can be best described as the superposition of a swell and a roughness of the order of the incident wavelength. As the presence of oil on the ocean surface reduces the friction and surface tension between liquid surface and wind, we accounted for the oil influence by adopting the Marangoni theory, as a damping of the ocean spectrum. For more information about the mathematics behind the Marangoni theory, the reader is referred to Alpers and Hühnerfuss, (1988). The oil spill signature used in the SAR simulator was generated as a level curve of a fractional Brownian motion (fBm) process. Similar to Coscione et al. (2011), a realization of the fBm process was created using the Weiersrass-Mandelbrot (WM) function, which is a superposition of M sinusoidal tones, spaced by an irrational parameter v, as in:

$$z(x,y) = A\sum_{p=0}^{M-1} C_p v^{-H.p} sin\left[k_0 v^p\left(xcos\Psi_p + ysin\Psi_p\right) + \Phi_p\right] \quad (4.17)$$

where H is the Hurst coefficient, k_0 is the wavenumber, A is the vertical overall height scaling factor, C_p, Φ_p, Ψ_p are amplitude, phase and direction coefficients respectively (Danisi et al.,

2007). In addition, the WM function was also used to simulate the shapes of areas with low wind intensity with respect to the free ocean surface, generating an ambiguity problem. For more information about the SAR simulator, the reader is referred to Franceschetti et al. (2002).

In our paper, we consider two SAR simulations, relevant to L- and X-band operating frequencies. Both simulations contain three types of features: (1) regular wind driven ocean background; (2) an oil spill feature; and (3) a low-wind oil spill look-alike. Figure 4.5a shows the results of the L-band simulation, where a surface wind speed of 10 m/s was used to simulate the ocean surface response. Figure 4.5b depicts the simulated X-band data, which was also generated for a wind speed of 10 m/s. For both simulations, we considered an ocean swell of 300 m, with a height of 3 m. The wind direction is 30^0 with respect to azimuth, the sensor look angle is 45^0, and the sensor's pulse repetition frequency (PRF) is 1736 Hz. In both cases, a spilled substance was simulated and highlighted on the image (Figure 4.5). The spilled substance corresponds to oleyl alcohol (OLA), where its dampening effect translates to a drastically reduced radar brightness in the spill area. Also, included in the simulation is a low-wind area (Figure 4.5). For this feature, a reduced wind speed of 2 m/s was used, also leading to a significant reduction in radar brightness. The simulations have an HH polarization, with a resolution of 5 m in azimuth, 18 m in ground range, and 13 m in slant range.

Following the outline approach in Section 4.3, LR was estimated for both the simulated L-band and X-band acquisitions (Figure 4.6) to perform background normalization and to optimize the contrast between oil spills and look-alikes. It can be observed from the LR-transformed images in Figure 4.6 that the LR pre-processing enhances the contrast between oil-covered areas, low wind look-alikes, and oil-free ocean surfaces. Qualitatively, look-alikes and oil spill features, whose signature was very similar in the amplitude data of Figure 4.5, are different from each

other after LR transformation. Also, the ocean background is now normalized even between L-band and X-band observation frequencies.

4.4.2. Using Simulated Data to Evaluate Oil Spill Detection Performance on our Adapted and an Alternative Oil Spill Detection Approach

After estimating the post-event and pre-event LR images for the L-band and X-band acquisitions, ratio images were generated and filtered (according to Section 4.3.2). After filtering, we applied the processing steps discussed in Section 4.3.3 to arrive at our final oil spill change detection result.

To evaluate the performance of our modified method (see Section 4.3), we conducted a qualitative and quantitative comparison of our algorithm to the result of a dark-spot detection (DSD) approach with spatial density thresholding published in Shu et al. (2010). We chose this method as a reference because of its unsupervised nature, its amplitude-based concept, and its high degree of automation, making it a good match for our own algorithm.

To evaluate our method's performance, we used the ground truth image for L-band and X-band acquisitions provided within the simulation process (Figure 4.7). Three performance measures were defined for use in performance assessment. These measures include: (i) the number of false alarms (FA), which assesses the number of background pixels incorrectly classified as oil spill. The false alarm rate (FAR) is computed in percentage as $(FAR) = FA/(FA + TN) \times 100\%$, where TN is the number of background pixels correctly classified as background; (ii) the number of missed hits (MH), which identifies the oil spill pixels incorrectly classified as ocean background. The missed hit rate (MHR) is computed in percentage as $(MHR) = MH/(MH + TP) \times 100\%$, where TP is the number of oil spill pixels correctly classified as oil spill; and (iii) the kappa coefficient which measures the agreement between

classification pixels and ground truth pixels. A kappa value of 1 represents perfect agreement while a value of 0 represents no agreement.

The classification results for both X-band and L-band data are shown in Figure 4.8 and Figure 4.9, respectively. Figures 4.8a and 4.9a correspond to the oil spill map produced by our algorithm while Figures 4.8b and 4.9b show the results of the reference techniques. The achieved classification performance according to FAR, MHR, and kappa coefficient parameters is shown in Table 4.1.

Based on Table 4.1, Figure 4.8, and Figure 4.9, the change detection result from the reference technique (DSD with spatial density thresholding) showed a lower performance for both the L-band and X-band acquisition compared to our method. The most striking difference is that the reference technique was unable to distinguish between the oil spill and the simulated low-wind lookalike. This is due to the fact that the reference method (Shu et al., 2010) is using the original radar brightness rather than the LR-transformed data as a basis for oil spill classification.

When applied to the L-band acquisition, the reference algorithm produced a false alarm rate of 1.79%, a missed hit rate of 1.31%, and a kappa coefficient of 0.76. At X-band, the reference technique gave a false alarm rate of 1.90%, a missed hit rate of 0.75%, and a kappa coefficient of 0.59. In contrast, our method achieved a much smaller false alarm rate of 0.11% at L-band, while maintaining a small missed hit rate of 1.81%. Due to the reduction of false alarms, our algorithms achieved a much-improved kappa coefficient of 0.97. Similar results were achieved for X-band FAR= 0.22%, MHR=0.24%, and a kappa coefficient of 0.93.

4.5. Application to Oil Spill Detection in SAR Images

4.5.1. Description of Area

To evaluate the performance of our algorithm under real imaging conditions, we analyzed image data of the 2010 Deepwater Horizon spill in the Gulf of Mexico (Figure 4.10). The oil spill originated from the Macondo Well, which is located in the Mississippi Canyon Block 252, approximately 93 km southeast of the Mississippi River delta (28.74°N, 88.39°W) (McNutt et al., 2011). The oil spill originated from a series of explosions that occurred at a 33,000-ton offshore oil-drilling rig (*Deepwater Horizon*), on the morning of April 20, 2010. The explosions resulted in oil leaking from the Macondo Well at an estimated rate of 35,000 to 60,000 barrels per day, and lasting for almost three months (Marghany, 2014). By April 25, the oil slick had spread very fast, covering about 1,500 km^2 of the ocean surface. During the three-month spill period, approximately 4.9 million barrels of oil were spilled.

4.5.2. Description of SAR Images Acquisitions

To analyze the performance of our approach when applied to X-band SAR data, we acquired four TerraSAR-X SAR images from the German Aerospace Center (DLR) through a PI proposal that was submitted by one of our team members. The image set includes one pre-event image acquired on April 25, 2010 (Figure 4.11a) and four post-event images acquired on April 25, 2010, April 30, 2010, May 1, 2010, and May 15, 2010, respectively (Figure 4.11b, Figure 4.11c, Figure 4.11d, and Figure 4.11e). In addition, three PALSAR images were available to us through the services of the Alaska Satellite Facility as the NASA Distributed Active Archive Center (DAAC) to also test the performance at L-band frequencies. Figure 4.11f is the PALSAR pre-event image acquired on May 28, 2010, while Figure 4.11g and Figure 4.11h are the post event images acquired on May 28, 2010 and June 26, 2010 respectively. The pre-event images in both

X- and L-band show an oil free ocean surface and are used as reference in the change detection-based oil spill detection approach.

The TerraSAR-X images were acquired in VV polarization and in ScanSAR mode to maximize spatial coverage. The images were acquired with a pixel size of 8.25 m, and an incidence angle of 37.9°. The PALSAR images were acquired in Fine Beam Double Polarization (FBD) mode with a pixel size of 12.5 m, and an incidence angle of 38.7°. Only HH polarization was used for the PALSAR image analysis. Figure 4.11b (a post-event image) shows that there are two dark spots. Visually looking at the true color of a Moderate Resolution Imaging Spectroradiometer (MODIS) on NASA's Aqua satellite, we concluded that the dark spot in the southwestern part of the image in Figure 4.11b is a true oil spill while the dark spot in the southeastern part is as a result of low wind speed. The rest of the post-event images contain only minimal low wind speed areas so that Figure 4.11b is used to demonstrate our ability to distinguish between oil covered and low-wind areas.

4.5.3. Experimental Methods and Analysis of Results

To normalize image background and enhance the contrast between oil-covered waters, look-alikes, and open ocean, we performed a texture transform for all SAR amplitude images by calculating LR using the GMWP presented in Section 4.3.1. Here, we used CWT with seven decomposition levels and a Mexican hat mother wavelet. We subset each image in Figure 4.11 into tiles [3 x 3] and calculate LR separately for each tile. Figure 4.12 shows the LR-transformed data of Figure 4.11. As previously mentioned, the ocean background appears near-normalized in the LR domain, with consistent LR levels around 0.98. At the same time, oil covered ocean areas have distinctly higher LR values around 1.15.

After texture transformation, the eight LR images were used to generate six different ratio images (four for TerraSAR-X and two for ALOS PALSAR), corresponding to six different area of interest (AOI) images (Table 4.2). To implement the classification process, each of the six ratio images (AOI 1-6) shown in Table 4.2 were filtered and decomposed into six resolution levels. The application of this wavelet transform leads to an increased improvement of the contrast between oil spills and other areas with every decomposition level. For example, in Figure 4.13 we qualitatively compare the characteristics of a PALSAR image in its original state, and after LR and wavelet transform has been applied. Figure 4.13a, depicts the original amplitude image while Figure 4.13b depicts its near-unimodal histogram distribution. Detecting oil spills from this image would result in many false alarms. In Figure 4.13c, an LR-transform has been applied resulting in an increase of contrast between open ocean and oil spill areas. This increase in contrast can be seen in Figure 4.13d as well, where the histogram shows a bimodal distribution. Figure 4.13e highlights the contrast that has increased further after both LR and wavelet computations were applied to the data. In addition to improving contrast, the wavelet operation also led to a significant reduction of noise, manifesting itself in narrower peaks in the image histogram in Figure 4.13f.

Another example showing the importance of LR and wavelet transform can be seen in a TerraSAR-X image, where the effect of low wind areas is noticeable. As shown in Figure 4.14, a multimodal histogram distribution occurs as the decomposition level increases, and this can help to separate oil spill from low wind and free ocean surface. The LR in this application is a way to enhance the contrast for dark spot detection but its main interest actually relies in that it discriminates between different textures and therefore allows dark spot classification into oil spills and look-alikes. It is important to note that, as the decomposition level increases, the

geometric details of the oil spill boundary decrease. This, however, suggests the use of lower decomposition levels (higher resolution) to analyze the border region while using the remaining levels to analyze the homogeneous areas (see Section 4.3.3).

After classification of the individual decomposition level images and the selection of reliable scales, we used the approach presented in Section 4.3.3.3 to fuse the K classification results achieved per pixel and to produce the final oil spill change detection map (see Figure 4.15b). To conduct a qualitative and quantitative evaluation of our approach, a ground truth map for AOI 1 was produced (Figure 4.15a). This ground truth map was generated via a manual digitization of the oil spill boundary in the original SAR image. The white areas in Figure 4.15a represent polluted by oil, while the black areas correspond to free ocean surface. Figure 4.15b shows the classification results for AOI 1 compared to the available ground truth information (white outlines in Figure 4.15b) to exemplify the classification performance of our approach. Even though the oil spill in AOI 1 was embedded in heterogeneous background, a good match between the near-automatic detection and the ground truth information is observed. In addition to this qualitative comparison, we conducted a quantitative analysis of the classification result of AOI 1. When comparing the change detection map of AOI 1 to the ground truth image, our approach yielded a false alarm rate of 0.07%, a missed hit rate of 5.56%, and a kappa coefficient of 0.96. Even though the original amplitude image (Figure 4.11b) is surrounded by heterogeneous background, very few false alarms were detected in the low wind areas. The minimal amount of missed hits can be seen in some areas where the boundaries of the oil spill are not clearly defined, and are smoothed by the wavelet transform. From both the qualitative and quantitative analysis, it is evident that our approach has identified the spill area, preserved the boundary of the spill, and was able to distinguish between true spills and low-wind look-

alikes. From our result, we estimated that the oil spill covered a total area of 1060 km^2 at the acquisition time of this image.

Classification results for the remaining five images are shown in Figure 4.16, indicating high classification performance also for these images. Qualitatively (visual) analyzing the case of AOI 2 and AOI 3, the boundary between the oil spill and the free ocean surface is well-delineated and only a few missed hits can be identified (Figure 4.16b and Figure 4.16d). For these cases, the oil spills captured by these images were estimated to have covered an area of 2813 km^2 and 2474 km^2, respectively. AOI 4 was a complex oil spill dealing with a spill signature embedded in heterogeneous background (Figure 4.16e). Despite this complexity, the classification result shows an excellent recovery of the oil spill area (Figure 4.16f), whose extent was estimated to be 389 km^2. In AOI 5, the oil spill region was cleanly extracted from a homogeneous background, and the spill area was estimated to be 272 km^2 (Figure 4.16h). Also in AOI 6, a good match between our classification result and the oil spill boundary was achieved. The oil spill in AOI 6 covered an area of 81 km^2 (Figure 4.16j).

4.5.4. Comparison with other Oil Spill Change Detection Methods

4.5.4.1. Comparison of Detection Map to a few Selected Methods

As stated in Section 4.2.2, we are focusing our attention exclusively on techniques using SAR amplitude data and will not be comparing with techniques using polarimetric data. To evaluate the performance of our algorithm relative to a few selected methods in this area of research, we conducted an extensive qualitative and quantitative comparison of the results of SLICK to results of other published change detection methods. The following alternative methods were used in the comparison: (a) Method A: semi-supervised change detection (SSCD) based on using a kernel-based abnormal detection and the wavelet decomposition of the SAR

image (Mercier and Girard-Ardhuin, 2006); (b) Method B: dark-spot detection (DSD) with spatial density thresholding (Shu et al., 2010); (c) Method C: Bundling tree-based ensemble classifier (Xu et al., 2014); and (d) Method D: Bagging tree-based ensemble classifier (Xu et al., 2014). For this comparison, we used the data from AOI 1 due to its more complex setup, including oil spill and look-alikes (Figure 4.17 and Table 4.3).

To improve the comparability of detection results, each alternative method has undergone the data enhancement and filtering step of the SLICK approach including logarithmic scaling, ratio image formation, and fast non-local means filtering. Following the approach in Section 4.3, our approach (Figure 4.17a) yielded a false alarm rate of 0.07%, a missed hit rate of 5.56%, and a kappa coefficient of 0.96 for the data in AOI 1. Based on Figure 4.17b, one can observe a performance degradation in Method A when compared with our approach. While the false alarm rate was small, it led to a significantly inflated missed hit rate of 40.30%, and a reduced kappa coefficient of 0.66. The lower detection rate is due to the similarities in grey level pixels between the free ocean surface, low wind speed areas, and oil spill areas. This spectral confusion has led to several false alarms and missed hits in the final oil spill result. It is worth noting that Method A strongly depends on the selection of training areas and the kernel design used. We believe that Method A is likely to give a promising result in a homogeneous environment, while it's more difficult to apply in more heterogeneous regions.

The oil spill change detection results from Method B are also inferior to our approach, mostly due to the difficulties of Method B with rejecting look-alikes. While computationally efficient, the application of intensity threshold segmentation which depends on the radiometric nature of the image resulted in high false alarms. This method generated a false alarm rate of 8.16%, a missed hit rate of 5.63%, and a kappa coefficient of 0.83.

Method C gave a reasonable result when compared to our approach. This is mainly due to the integration of a prediction function as an added predictor for building the classification trees. Due to its basis on amplitude information, some false alarms remain in the low-wind lookalike region. Method C achieved a false alarm rate of 4.16%, a missed hit rate of 11.23%, and a kappa coefficient of 0.85.

The tree-based ensemble technique used in Method C also gave a result similar to Method D. The method generated several trees by using random bootstrap samples of the dataset, and assigned a class membership based on majority voting among the trees. The method produced a false alarm rate of 4.17%, a missed hit rate of 11.23%, and a kappa coefficient of 0.85. Note that this method is the most computationally expensive of all tested approaches. This is due to the many random (bootstrap) samples of the dataset that is required by the technique.

4.5.4.2. Performance Estimation using ROC Curves and Statistical Comparison

We show the performance analysis by calculating full receiver operating characteristic (ROC) curves for each technique. The ROC curve is a two-dimensional plot in which a true positive rate is plotted against a false alarm rate as thresholds or other model parameters are varied. In constructing the ROC curves, predicted probabilities are used rather than a binary result. Using a binary result corresponds to a single point in an ROC space. After the construction of the ROC curves, we compare each change detection method not only by the shape of the ROC curves but also by the area under the ROC curve (AUC). AUC close to 100% depicts a high detection performance.

A qualitative analysis of the generated ROC curves (Figure 4.18) indicates that our method outperforms all other tested methods in detection performance. It's true positive rate is growing faster for smaller false alarm rates and reaches higher true positive rates than all other methods.

The results shown in Figure 18 imply that our method achieves a better overall performance, with an AUC of 99.4 %. Other change detection methods like Method A, B, C and D gave an AUC of 93.2%, 98.3%, 94.9%, 95.1% respectively.

4.5.4.3. Statistical Comparison of the Performance Matrix using Wilcoxon Signed Rank Test

Furthermore, in this paper, we are also interested in statistically determining if there are significant differences in terms of performance between the individual change detection methods. In estimating this, we divide the change detection result of each method into 64 different tiles. For each of the 64 different tiles, we estimated overall accuracy that are then used as input data for the Wilcoxon signed rank test. We chose the Wilcoxon signed rank test because of its non-parametric nature and the non-Gaussian distribution of our data. We defined the null hypothesis, such that the differences in performance between each change detection method are not statistically significant from one another using a p-value of 0.05. A p-value greater than 0.05 indicates that our null hypothesis should be accepted, while a p-value lower than 0.05 indicates that our null hypothesis should be rejected. The result of our comparison can be seen in Table IV and shows that our approach is statistically significant when compared with other methods, with a p-value less than 0.05. However, Method B, C and D with a p-value greater than 0.05 are not statistically significant from one another.

4.6. Conclusion

An approach for oil spill detection from SAR images based on multi-scale time-frequency theory was presented in this paper. The Scale-space LIpschitz-based Change tracKing (SLICK) approach, which includes a combination of a normalization step, a data enhancement and

filtering step, and the application of the multi-scale oil spill change detection technique were adapted from Ajadi et al. (2016) for oil spill detection. A technique based on LR was presented first to normalize the reflectivity properties of ocean water and maximize the visibility of oil in water. The method of LR is robust, simple, and well-suited to an unsupervised change detection approach. Integration of modern non-local filtering and UDWT techniques gave a high robustness against noise. In addition, our oil spill change detection technique gave a good result when an EM algorithm with mathematical morphology are integrated, and preservation of the geometric details in the border regions was shown when fusion at the decision level by an "optimal" scale selection was employed. Analyzing the performance result of our approach using both an oil spill simulated and a real oil spill event dataset, we found out that our approach gave a very high detection rate. In all, this approach can be used to detect oil spills and discard false alarms produced by natural phenomena. Also, our approach outperformed several other selection methods, and it is useful in lieu of other solutions, where training of features can be time consuming and difficult.

The main drawback of the approach is the assumption that the image is a mixture of Gaussian distribution. Future work will explore using other look-alikes such as biogenic slicks in the presence of an oil spill. We would also like to apply our approach to detect oil spills in sea ice. Also, we will explore using Gamma distribution for fitting the EM algorithm rather than the assumed Gaussian distribution.

4.7. Acknowledgments

The authors want to thank the Alaska Satellite Facility (ASF) for providing access to the PALSAR data used in this study. The TerraSAR-X data were provided by the German Aerospace center (DLR) under proposal MTH2653. We furthermore thank the American

Association of Petroleum Geologists and Alaska Geological Society for providing financial support. The work presented here was funded by the National Aeronautics and Space Administration (NASA) through Established Program to Stimulate Competitive Research (EPSCoR) program under grant #NNX11AQ27A.

4.8. Author Contributions

This research was written and revised by Olaniyi Ajadi with contributions from all coauthors. All authors have read and approved the final manuscript.

4.9. References

Ajadi, O. A., Meyer, F. J., and Webley, P. W., 2016, Change Detection in Synthetic Aperture Radar Images Using a Multiscale-Driven Approach: Remote Sensing, v. 8, no. 6, p. 482.

Alpers, W., and Hühnerfuss, H., 1988, Radar signatures of oil films floating on the sea surface and the Marangoni effect: Journal of Geophysical Research, v. 93, no. C4, p. 3642-3648.

Benelli, G., and Garzelli, A., 1999, Oil-spills detection in SAR images by fractal dimension estimation, *in* Proceedings Geoscience and Remote Sensing Symposium, 1999. IGARSS'99 Proceedings. IEEE 1999 International, v. 1, p. 218-220.

Bovolo, F., and Bruzzone, L., 2005, A detail-preserving scale-driven approach to change detection in multitemporal SAR images: IEEE Transactions on Geoscience and Remote Sensing, v. 43, no. 12, p. 2963-2972.

Brekke, C., and Solberg, A. H., 2008, Classifiers and confidence estimation for oil spill detection in ENVISAT ASAR images: Geoscience and Remote Sensing Letters, v. 5, no. 1, p. 65-69.

Buades, A., Coll, B., and Morel, J. M., 2005, A non-local algorithm for image denoising: IEEE Computer Society Conference, v. 2, p. 60-65.

Celik, T., 2010, A Bayesian approach to unsupervised multiscale change detection in synthetic aperture radar images: Signal Processing, v. 90, no. 5, p. 1471-1485.

Coscione, R., Di Martino, G., Iodice, A., Riccio, D., and Ruello, G., 2011, Multifractal analysis of oil slicks on SAR images, *in* Proceedings SPIE Remote Sensing, International Society for Optics and Photonics, p. 81790H-81790H-81798.

Danisi, A., Martino, G. D., Iodice, A., Riccio, D., Ruello, G., Tello, M., Mallorqui, J. J., and Lopez-Martinez, C., 2007, SAR simulation of ocean scenes covered by oil slicks with arbitrary shapes, *in* Proceedings Geoscience and Remote Sensing Symposium, p. 1314-1317.

Fortuny, J., Tarchi, D., Ferraro, G., and Sieber, A., 2004, The use of satellite radar imagery in the Prestige accident, *in* Proceedings of the International Conference Interspill, p. 14-17.

Franceschetti, G., Iodice, A., Riccio, D., Ruello, G., and Siviero, R., 2002, SAR raw signal simulation of oil slicks in ocean environments: IEEE Transactions on Geoscience and Remote Sensing, v. 40, no. 9, p. 1935-1949.

Frate, F. D., Petrocchi, A., Lichtenegger, J., and Calabresi, G., 2000, Neural networks for oil spill detection using ERS-SAR data: IEEE Transactions on Geoscience and Remote Sensing, v. 38, no. 5, p. 2282-2287.

Gade, M., and Redondo, J. M., 1999, Marine pollution in European coastal waters monitored by the ERS-2 SAR: a comprehensive statistical analysis, *in* Proceedings OCEANS'99 MTS/IEEE. Riding the Crest into the 21st Century1999, v. 3, p. 1239-1243.

Garcia-Pineda, O., MacDonald, I. R., Li, X., Jackson, C. R., and Pichel, W. G., 2013, Oil spill mapping and measurement in the Gulf of Mexico with Textural Classifier Neural Network Algorithm (TCNNA): IEEE Journal of Selected Topics in Applied Earth Observations and Remote Sensing, v. 6, no. 6, p. 2517-2525.

Girard-Ardhuin, F., Mercier, G., Collard, F., and Garello, R., 2005, Operational oil-slick characterization by SAR imagery and synergistic data: IEEE Journal of Oceanic Engineering, v. 30, no. 3, p. 487-495.

Hambaba, A., 2000, Nonstationary statistical tests in time-scale space: Aerospace Conference Proceedings.

Hodgins, D., Salvador, S., Tinis, S., and Nazarenko, D., 1996, RADARSAT SAR for oil spill response: Spill Science & Technology Bulletin, v. 3, no. 4, p. 241-246.

Hou, B., Wei, Q., Zheng, Y., and Wang, S., 2014, Unsupervised change detection in SAR image based on Gauss-log ratio image fusion and compressed projection: IEEE Journal of Selected Topics in Applied Earth Observations and Remote Sensing, v. 7, no. 8, p. 3297-3317.

Hovland, H., Johannessen, J., and Digranes, G., Slick detection in SAR images, *in* Proceedings Geoscience and Remote Sensing Symposium, 1994. IGARSS'94. Surface and Atmospheric Remote Sensing: Technologies, Data Analysis and Interpretation., International, v. 4, p. 2038-2040.

Ivanov, A. Y., and Ermoshkin, I. S., 2004, Mapping oil spills in the caspian sea using ERS-1/ERS-2 SAR image quick-looks and GIS: Gayana (Concepción), v. 68, no. 2, p. 297-304.

Kim, D.-J., Moon, W. M., and Kim, Y.-S., 2010, Application of TerraSAR-X data for emergent oil-spill monitoring: IEEE Transactions on Geoscience and Remote Sensing, v. 48, no. 2, p. 852-863.

Lu, J., Kwoh, L., Lim, H., Liew, S., and Bao, M., 2000, Mapping oil pollution from space: Backscatter, v. 11, no. 1, p. 23-26.

Mallat, S., 1999, A wavelet tour of signal processing, Academic Press.

Marghany, M., 2014, Oil Spill Pollution Automatic Detection from MultiSAR Satellite Data Using Genetic Algorithm. Advanced Geoscience Remote Sensing.

Marghany, M., 2015, Automatic detection of oil spills in the Gulf of Mexico from RADARSAT-2 SAR satellite data: Environmental Earth Sciences, v. 74, no. 7, p. 5935-5947.

Marghany, M., and Van Genderen, J., 2001, Texture algorithms for oil pollution detection and tidal current effects on oil spill spreading: Asian Journal of Geoinformatics, v. 1, p. 33-44.

McNutt, M. K., Camilli, R., Guthrie, G. D., Hsieh, P. A., Labson, V. F., Lehr, W. J., Maclay, D., Ratzel, A. C., and Sogge, M. K., 2011, Assessment of flow rate estimates for the Deepwater Horizon/Macondo well oil spill, US Department of the Interior.

Mercier, G., and Girard-Ardhuin, F., 2006, Partially supervised oil-slick detection by SAR imagery using kernel expansion: IEEE Transactions on Geoscience and Remote Sensing, v. 44, no. 10, p. 2839-2846.

Migliaccio, M., Gambardella, A., Nunziata, F., Shimada, M., and Isoguchi, O., 2009, The PALSAR polarimetric mode for sea oil slick observation: IEEE Transactions on Geoscience and Remote Sensing, v. 47, no. 12, p. 4032-4041.

Moctezuma, M., and Parmiggiani, F., 2014, Adaptive stochastic minimization for measuring marine oil spill extent in synthetic aperture radar images: Journal of Applied Remote Sensing, v. 8, no. 1, p. 083553-083553.

Moon, T. K., 1996, The expectation-maximization algorithm: Signal Processing Magazine, IEEE, v. 13, no. 6, p. 47-60.

Nirchio, F., Sorgente, M., Giancaspro, A., Biamino, W., Parisato, E., Ravera, R., and Trivero, P., 2005, Automatic detection of oil spills from SAR images: International Journal of Remote Sensing, v. 26, no. 6, p. 1157-1174.

Palenzuela, J. T., Vilas, L. G., and Cuadrado, M. S., 2006, Use of ASAR images to study the evolution of the Prestige oil spill off the Galician coast: International Journal of Remote Sensing, v. 27, no. 10, p. 1931-1950.

Puestow, T., Parsons, L., Zakharov, I., Cater, N., Bobby, P., Fuglem, M., Parr, G., Jayasiri, A., Warren, S., and Warbanski, G., 2013, Oil spill detection and mapping in low visibility and ice: surface remote sensing: Arctic Oil Spill Response Technology Joint Industry Programme (JIP).

Ren, P., Di, M., Song, H., Luo, C., and Grecos, C., 2016, Dual Smoothing for Marine Oil Spill Segmentation: IEEE Geoscience and Remote Sensing Letters, v. 13, no. 1, p. 82-86.

Salberg, A.-B., Rudjord, O., and Solberg, A. H. S., 2014, Oil spill detection in hybrid-polarimetric SAR images: IEEE Transactions on Geoscience and Remote Sensing, v. 52, no. 10, p. 6521-6533.

Shu, Y., Li, J., Yousif, H., and Gomes, G., 2010, Dark-spot detection from SAR intensity imagery with spatial density thresholding for oil-spill monitoring: Remote Sensing of Environment, v. 114, no. 9, p. 2026-2035.

Singha, S., Ressel, R., Velotto, D., and Lehner, S., 2016, A combination of traditional and polarimetric features for oil spill detection using TerraSAR-X: IEEE Journal of Selected Topics in Applied Earth Observations and Remote Sensing, v. 9, no. 11, p. 4979-4990.

Solberg, A. H. S., Storvik, G., Solberg, R., and Volden, E., 1999, Automatic detection of oil spills in ERS SAR images: IEEE Transactions on Geoscience and Remote Sensing, v. 37, no. 4, p. 1916-1924.

Solberg, A. H. S., and Volden, E., 1997, Incorporation of prior knowledge in automatic classification of oil spills in ERS SAR images, *in* Proceedings Geoscience and Remote Sensing, 1997. IGARSS'97. Remote Sensing-A Scientific Vision for Sustainable Development., 1997 IEEE International, v. 1, p. 157-159.

Taravat, A., and Oppelt, N., 2014, Adaptive weibull multiplicative model and multilayer perceptron neural networks for dark-spot detection from SAR imagery: Sensors, v. 14, no. 12, p. 22798-22810.

Tello, M., Lopez-Martinez, C., Mallorqui, J. J., Danisi, A., Di Martino, G., Iodice, A., Ruello, G., and Riccio, D., 2007, Characterization of local regularity in SAR imagery by means of multiscale techniques: application to oil spill detection, *in* Proceedings Geoscience and Remote Sensing Symposium. IGARSS 2007. IEEE International, p. 5228-5231.

Topouzelis, K., Karathanassi, V., Pavlakis, P., and Rokos, D., 2007, Detection and discrimination between oil spills and look-alike phenomena through neural networks: ISPRS Journal of Photogrammetry and Remote Sensing, v. 62, no. 4, p. 264-270.

Topouzelis, K. N., 2008, Oil spill detection by SAR images: dark formation detection, feature extraction and classification algorithms: Sensors, v. 8, no. 10, p. 6642-6659.

Turiel, A., Pérez-Vicente, C. J., and Grazzini, J., 2006, Numerical methods for the estimation of multifractal singularity spectra on sampled data: a comparative study: Journal of Computational Physics, v. 216, no. 1, p. 362-390.

Wang, N., and Lu, C., 2010, Two-dimensional continuous wavelet analysis and its application to meteorological data: Journal of Atmospheric and Oceanic Technology, v. 27, no. 4, p. 652-666.

Xu, L., Li, J., and Brenning, A., 2014, A comparative study of different classification techniques for marine oil spill identification using RADARSAT-1 imagery: Remote Sensing of Environment, v. 141, p. 14-23.

Xu, L., Shafiee, M. J., Wong, A., and Clausi, D. A., 2016, Fully Connected Continuous Conditional Random Field With Stochastic Cliques for Dark-Spot Detection In SAR Imagery: IEEE Journal of Selected Topics in Applied Earth Observations and Remote Sensing, v. 9, no. 7, p. 2882-2890.

Yu, H., Wang, Q., Zhang, Z., Zhang, Z.-J., Tang, W., Tang, X., Yue, S., and Wang, C.-S., 2017, Oil spill detection using hyperspectral infrared camera, *in* Proceedings SPIE/COS Photonics Asia, International Society for Optics and Photonics, p. 100301G-100301G-100310.

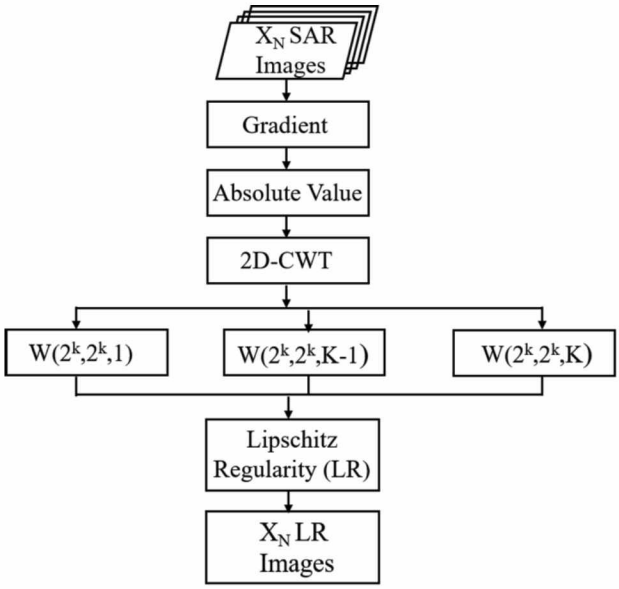

Figure 4.1. Workflow for our LR estimation, where $\boldsymbol{X_N}$ LR images are all the Lipschitz transformed SAR images, 2D-CWT is a two-dimensional continuous wavelet transform, and 'W' are the wavelet coefficients.

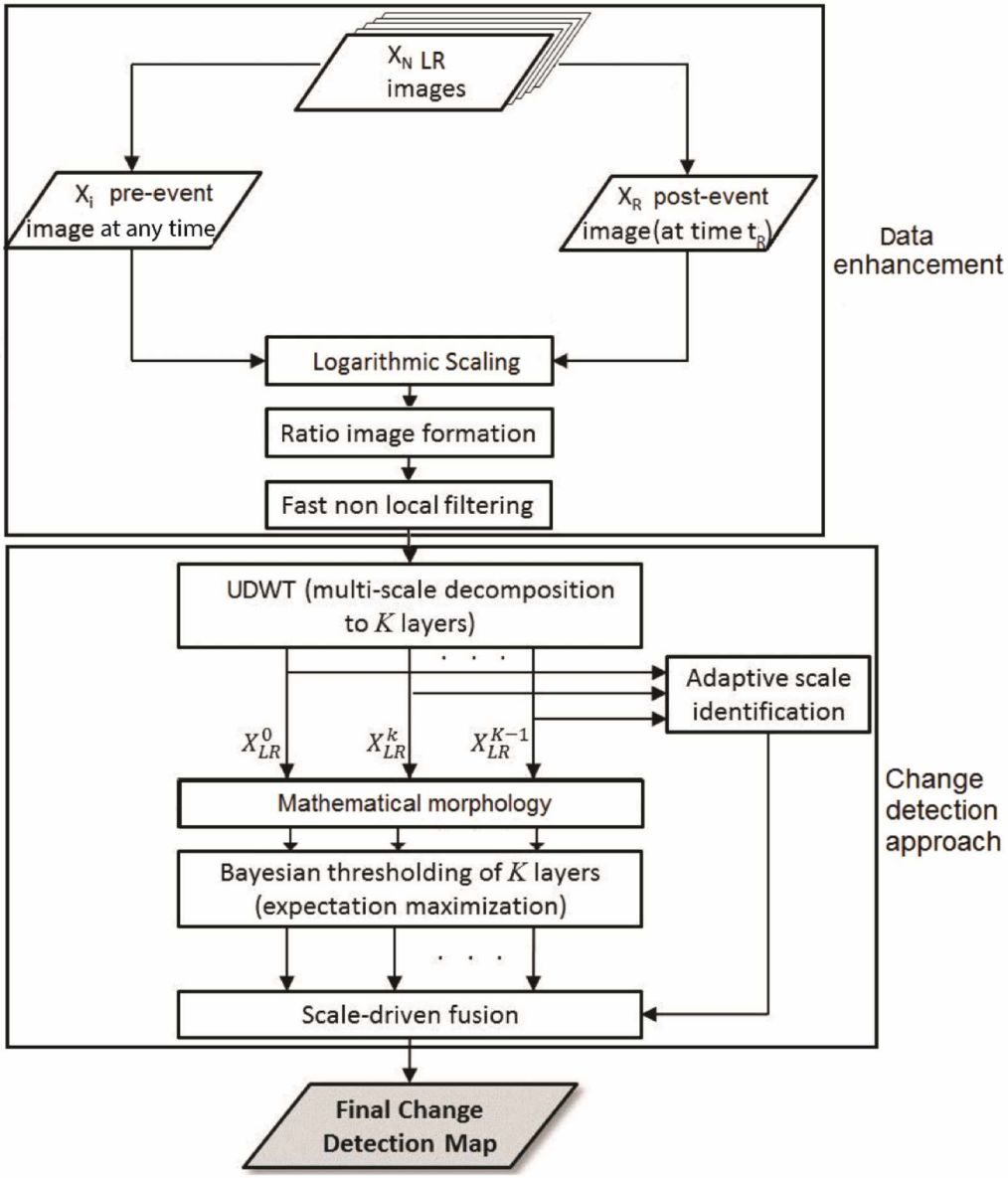

Figure 4.2. Workflow of our adapted approach. Here, UDWT is an undecimated discrete wavelet transform, $\mathbf{X_{LR}^0}$ is the original log-ratio image, $\mathbf{X_{LR}^k}$ is the $\boldsymbol{k^{th}}$ decomposed image, $\mathbf{X_{LR}^{K-1}}$ is the lowest decomposed level, and $\boldsymbol{k}$ is the level of decomposition.

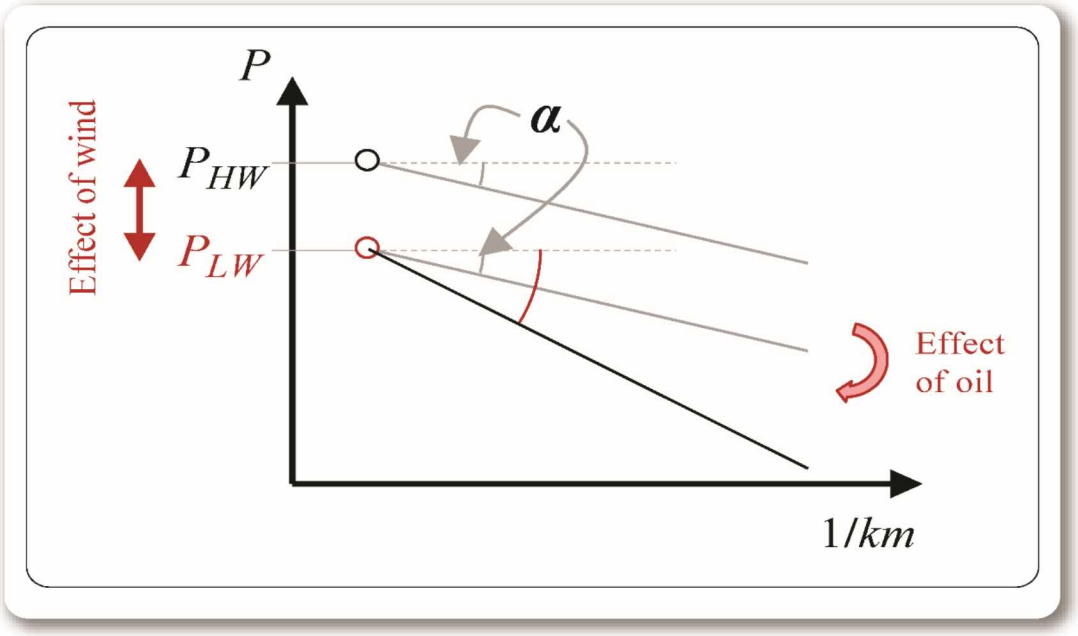

Figure 4.3. Plot showing the LR $\boldsymbol{\alpha}$ of the power spectrum of high wind ($\boldsymbol{P_{HW}}$) effect, low wind ($\boldsymbol{P_{LW}}$) effect, and areas affected by oil.

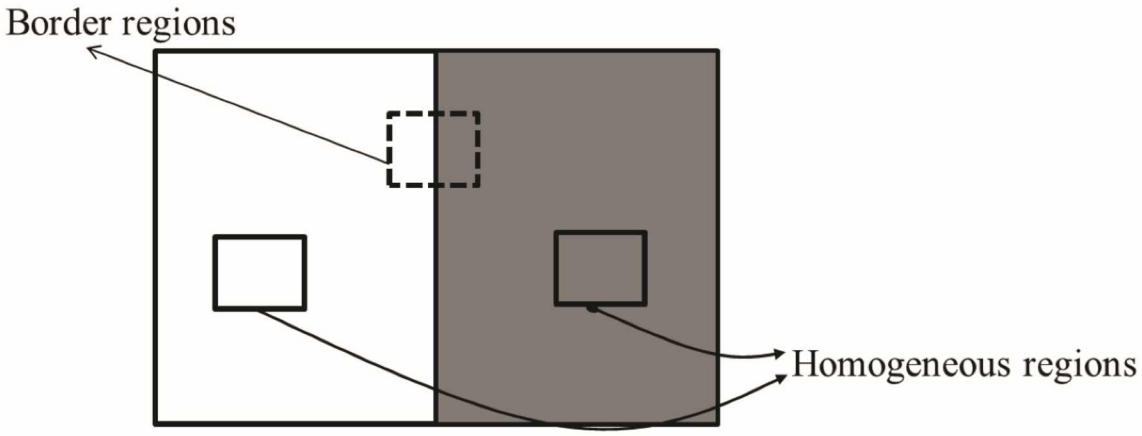

Figure 4.4. Selection of reliable scale. White areas may represent areas of no-change, while gray areas may represent areas of change. Solid box indicates homogeneous regions, while the dashed box indicates a border region.

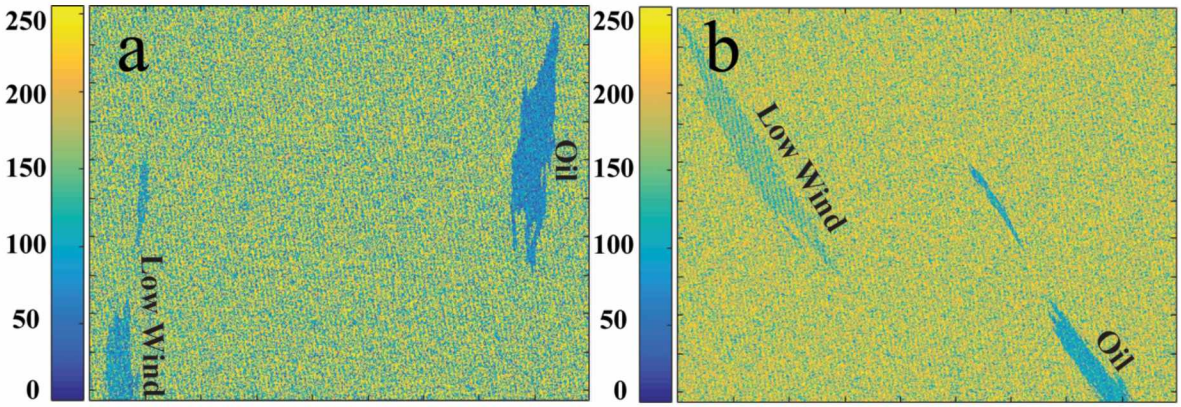

Figure 4.5. Two examples of SAR simulations showing: (a) the L-band acquisition with a wind speed of 10 m/s in the clean ocean environment, a wind speed of 2 m/s in the look-alike environment and area affected by oil spill; and (b) X-band acquisition with a wind speed of 10 m/s in the clean ocean environment, a wind speed of 2 m/s in the look-alike environment and area affected by oil spill. It is worth mentioning that even though there are intensity variations between the L-band and X-band acquisitions, they are normalized after LR (see Figure 4.6).

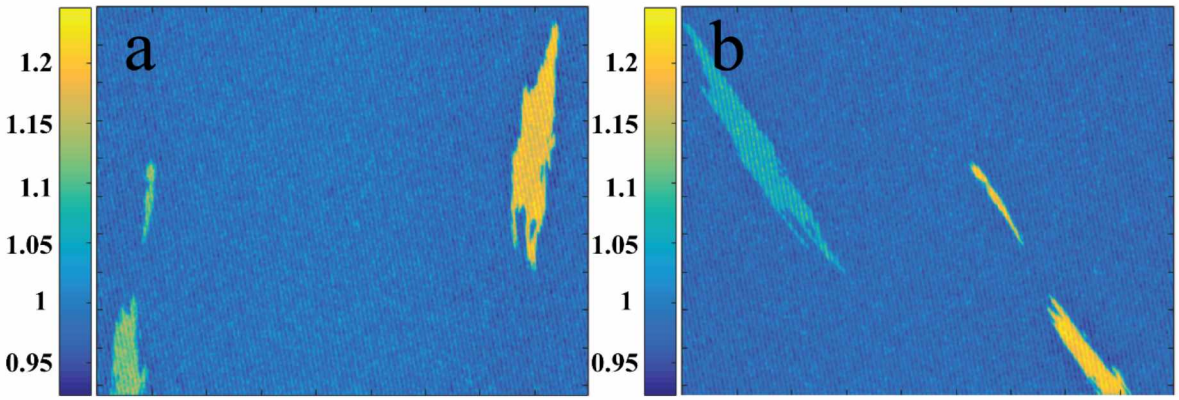

Figure 4.6. Estimated LR for (a) L-band acquisition; and (b) X-band acquisition.

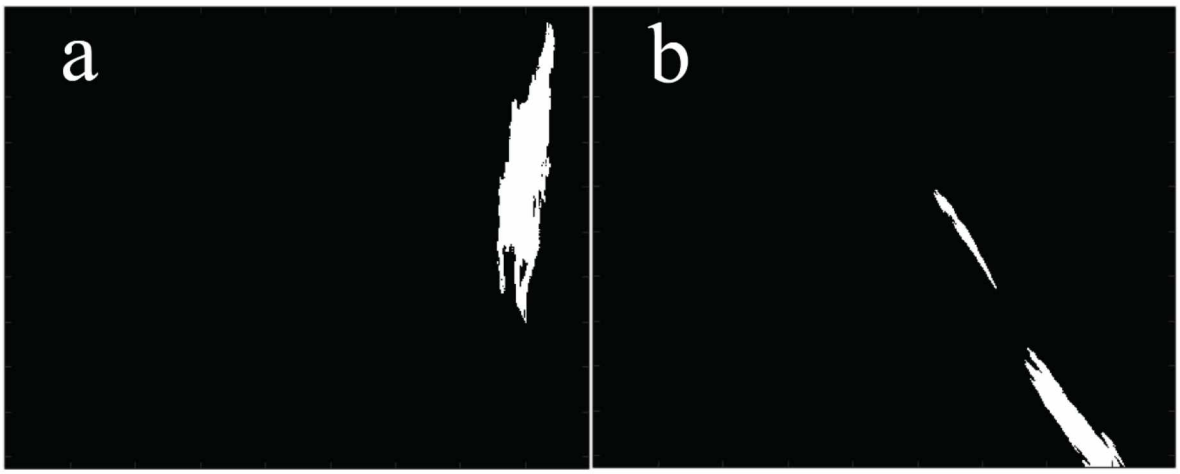

Figure 4.7. Ground truth change map for (a) L-band; and (b) X-band acquisition. White area depicts area affected by surfactant material and black area shows free ocean surface.

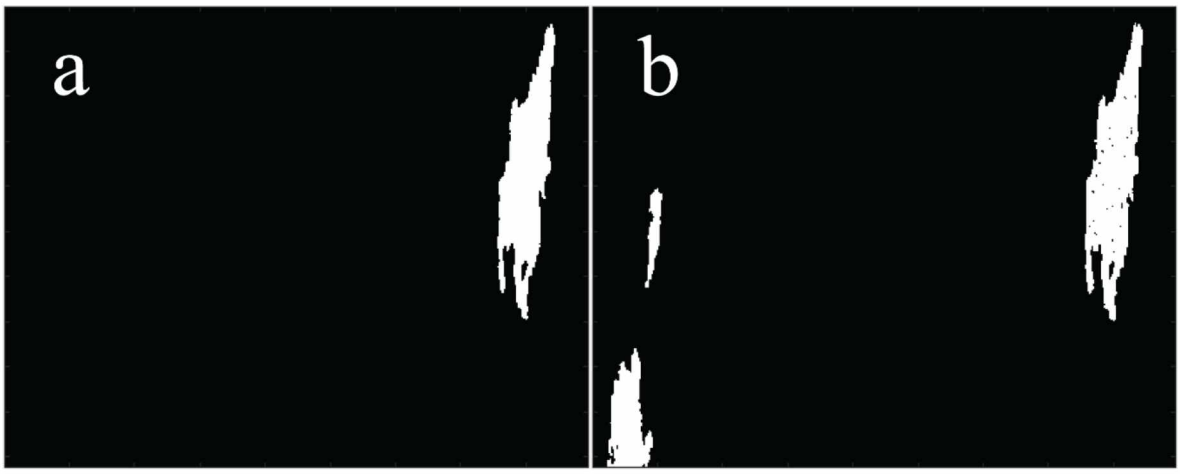

Figure 4.8. Oil spill classification map after applying (a) SLICK; and (b) DSD to the L-band acquisition.

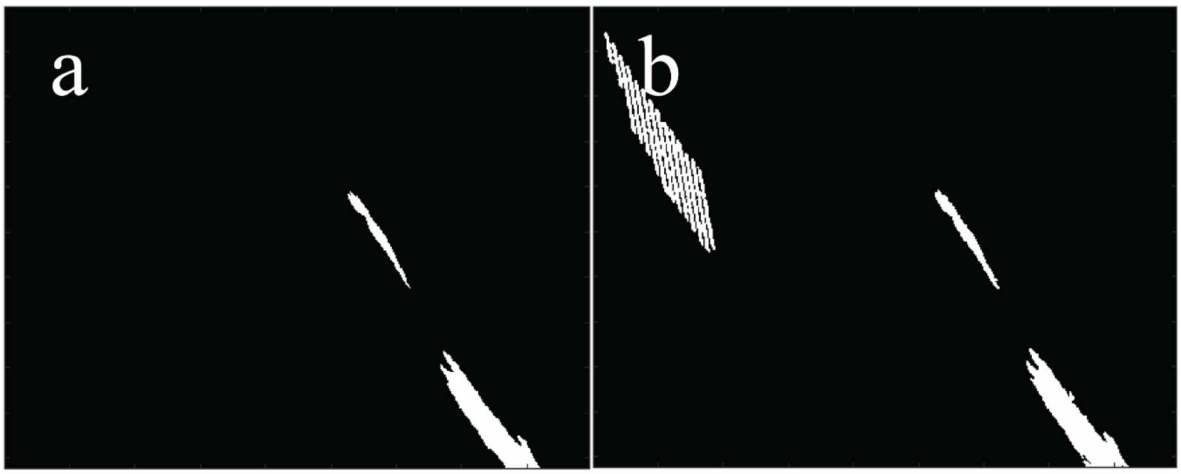

Figure 4.9. Oil spill classification map after applying (a) SLICK; and (b) DSD to the X-band acquisition.

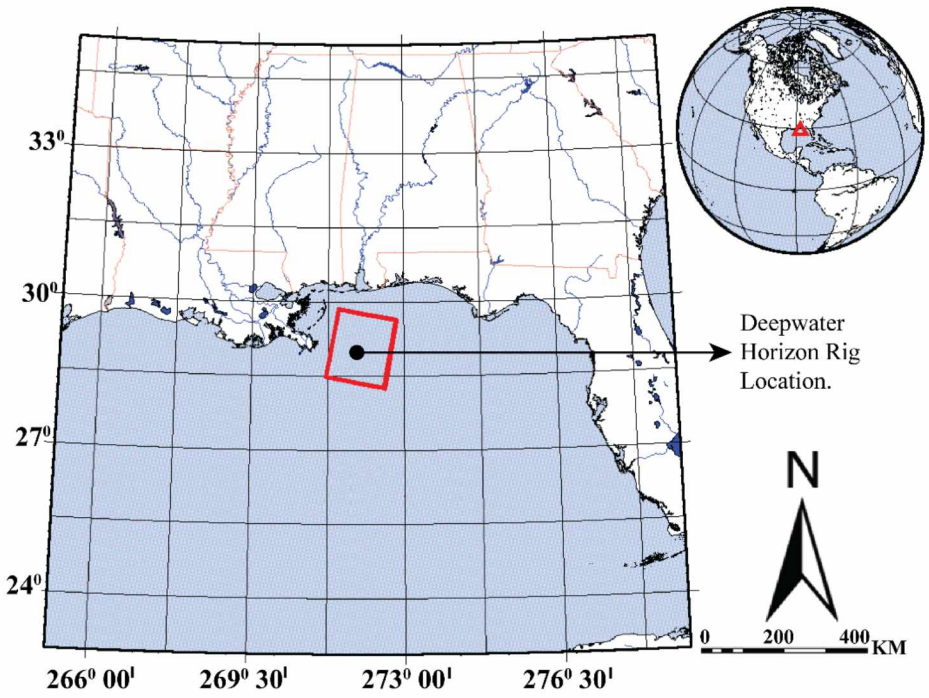

Figure 4.10. Location of the Deepwater Horizon where the red box indicates area of the SAR acquisitions.

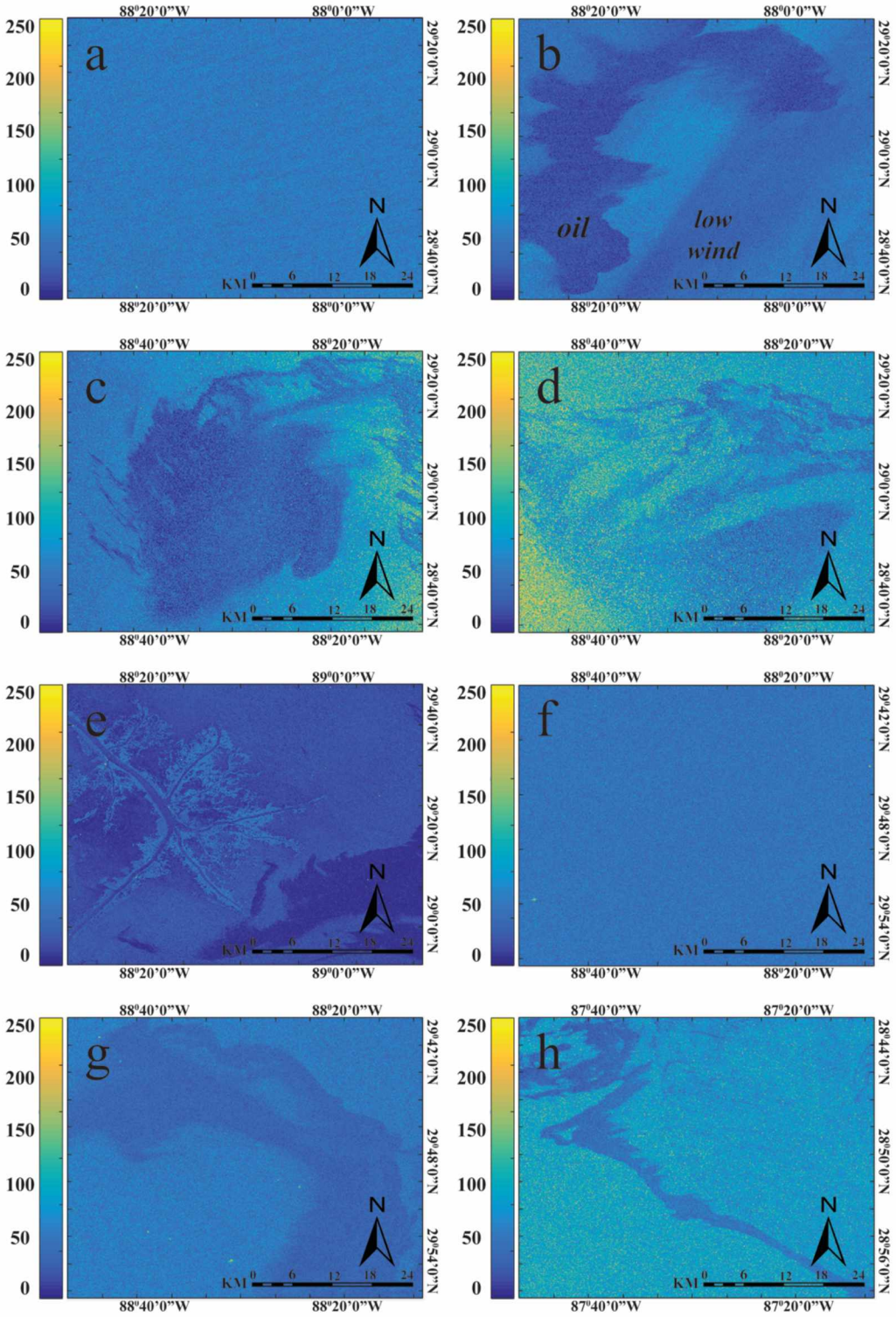

Figure 4.11. TerraSAR-X images acquired on: (a) April 25, 2010; (b) April 25, 2010; (c) April 30, 2010; (d) May 1, 2010; and (e) May 15, 2010. PASAR image acquired on: (f) May 28, 2010; (g) May 28, 2010; and (h) June 26, 2010.

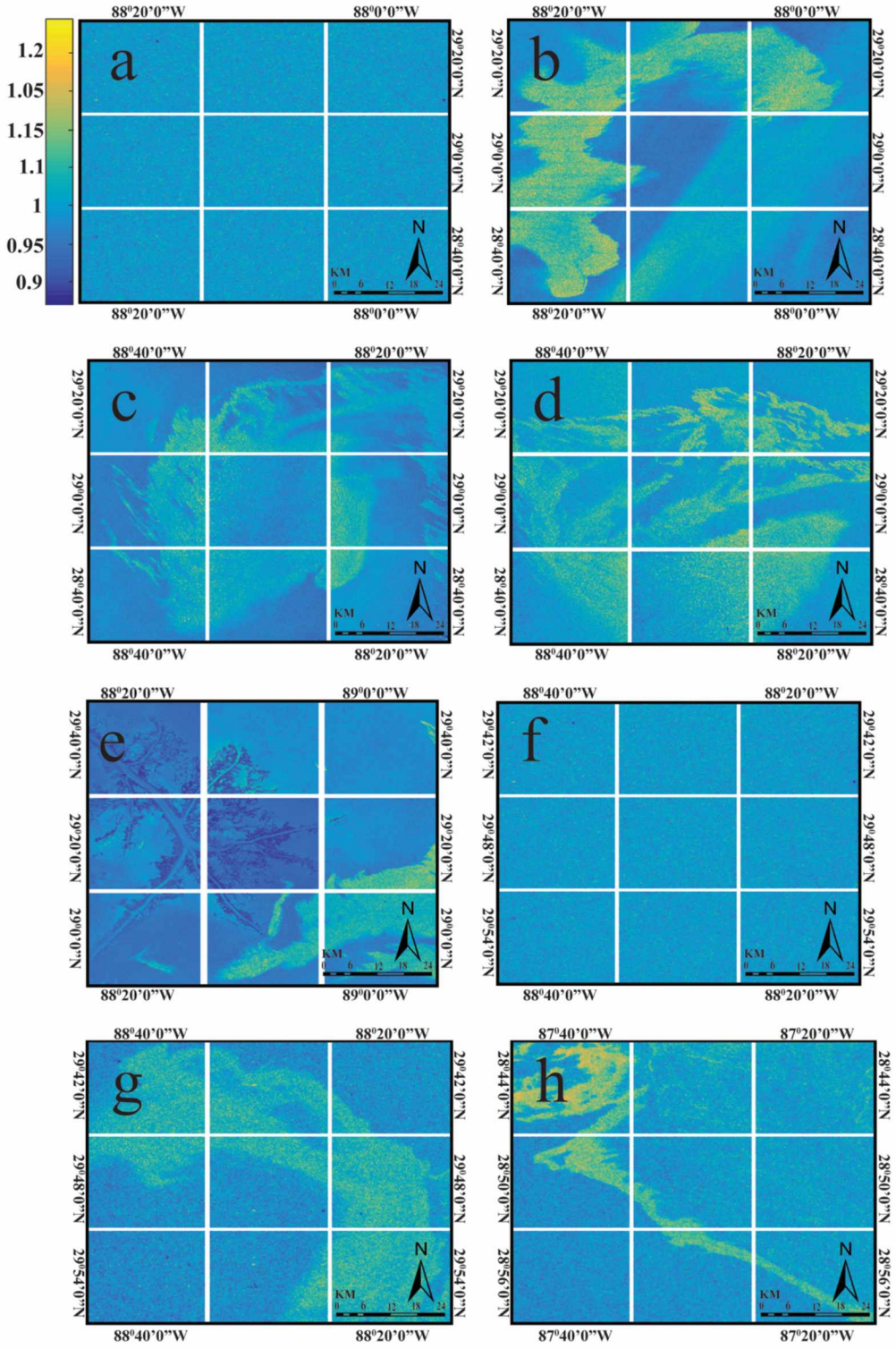

Figure 4.12. LR-transformation of TerraSAR-X images acquired on: (a) April 25, 2010; (b) April 25, 2010; (c) April 30, 2010; (d) May 1, 2010; and (e) May 15, 2010. LR for PALSAR image acquired on: (f) May 28, 2010; (g) May 28, 2010; and (h) June 26, 2010.

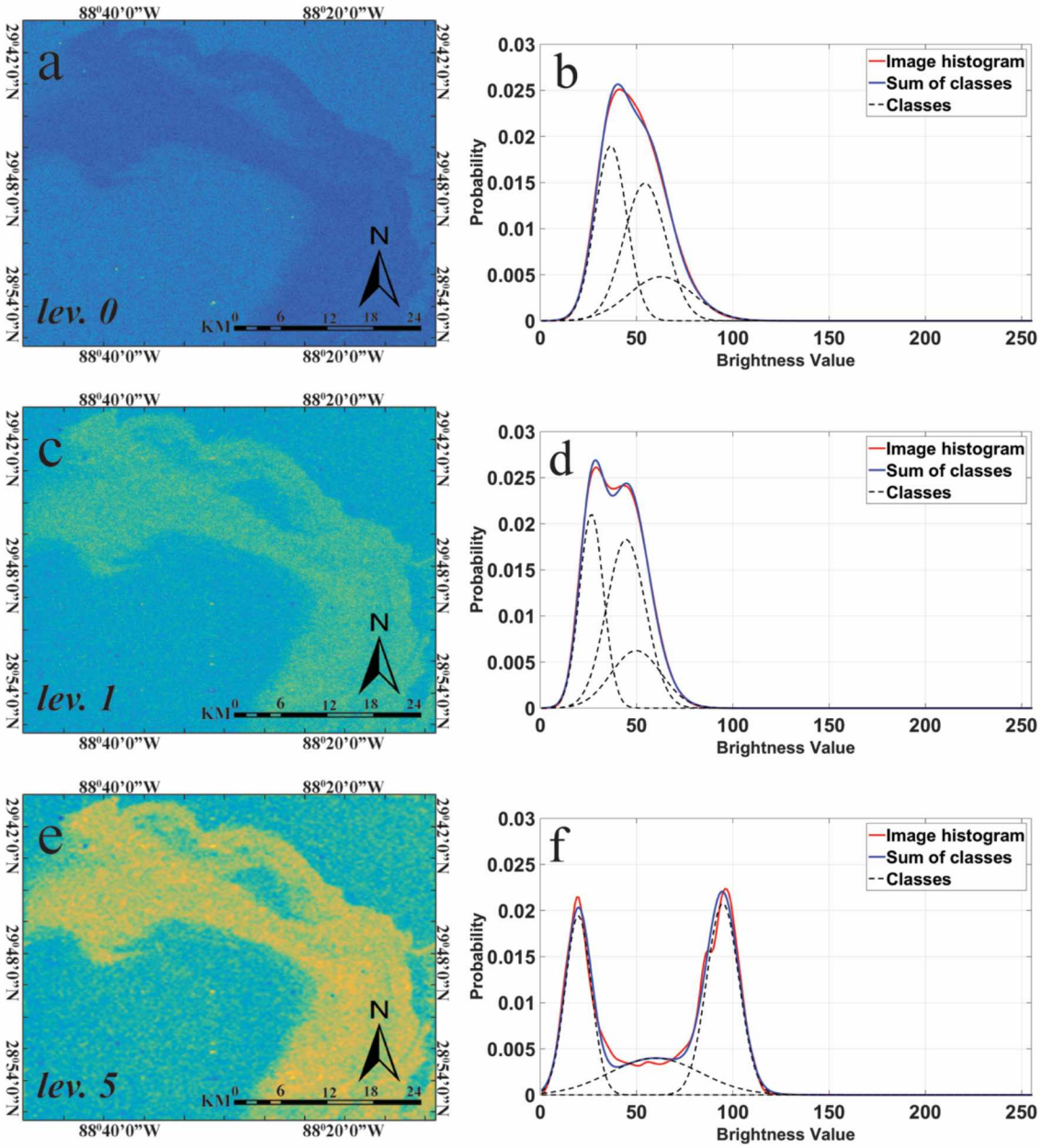

Figure 4.13. The PALSAR image is represented by a, and b shows its unimodal histogram distribution. The same image after LR has been applied with one level (lev. 1) of decomposition is depicted as c, and d denotes its bimodal histogram distribution. The same image after applying LR with five levels (lev. 5) of decomposition is denoted as e, and f shows its multimodal histogram. As we transfer down decomposition levels (lev. 2 to lev. 4) the distribution transforms into the multimodal distribution.

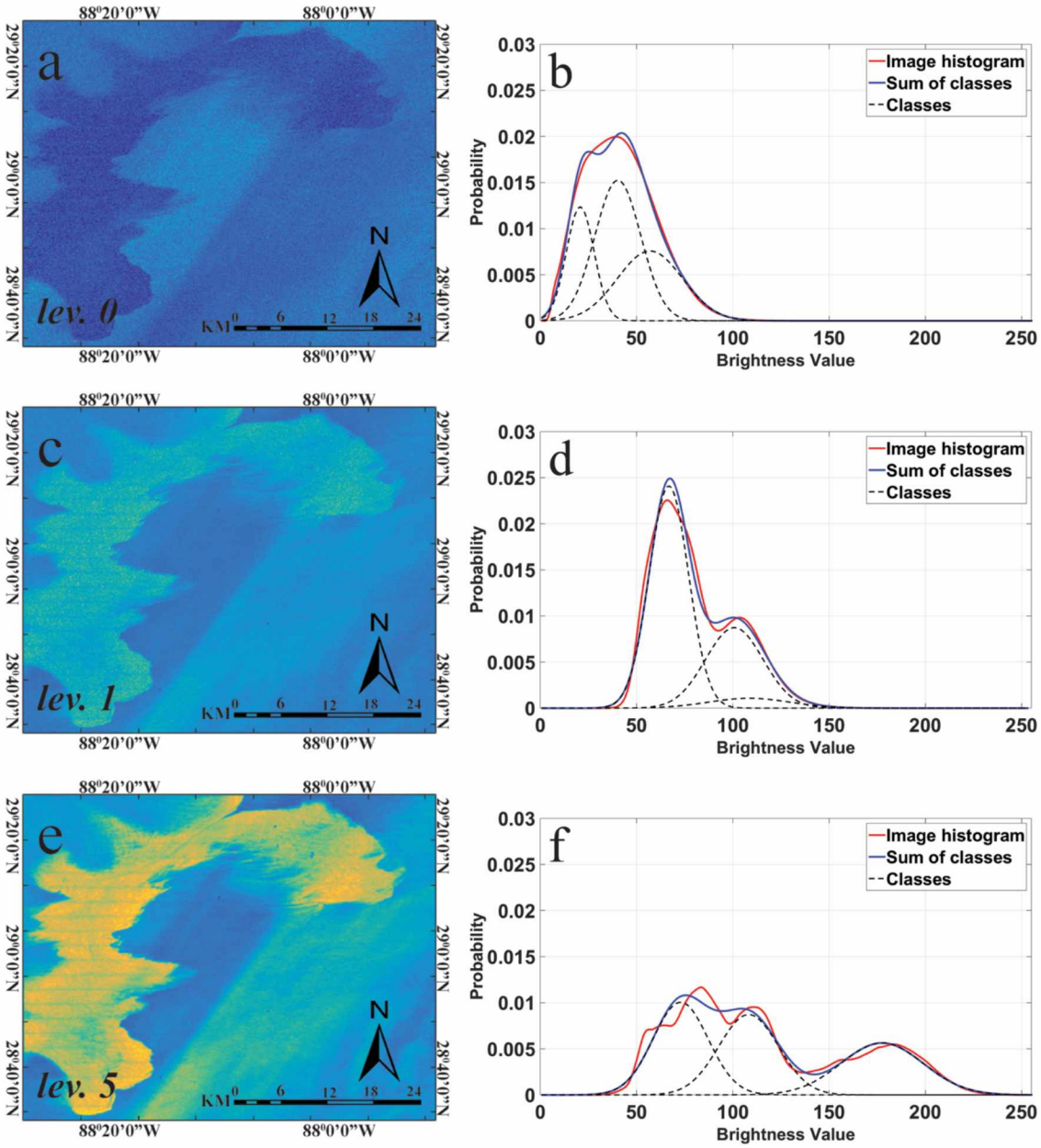

Figure 4.14. The TerraSAR-X image is represented by a, and b shows its unimodal histogram distribution. The same image after LR has been applied with one level (lev. 1) of decomposition is denoted as c, and d shows its bimodal histogram distribution. The same image after applying LR with five levels (lev. 5) of decomposition is denoted as e, and f shows its multimodal histogram.

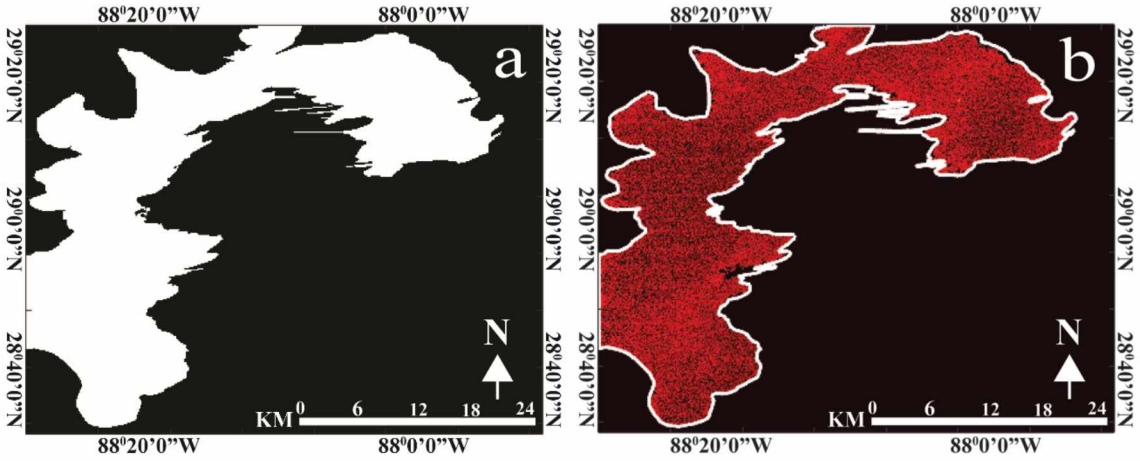

Figure 4.15. a) Ground truth change map, where white area depicts oil spill affected area, while black area shows free ocean surface and b) the overlay of Change detection map resulting from fusion at the decision level applied to AOI 1 with ground truth image.

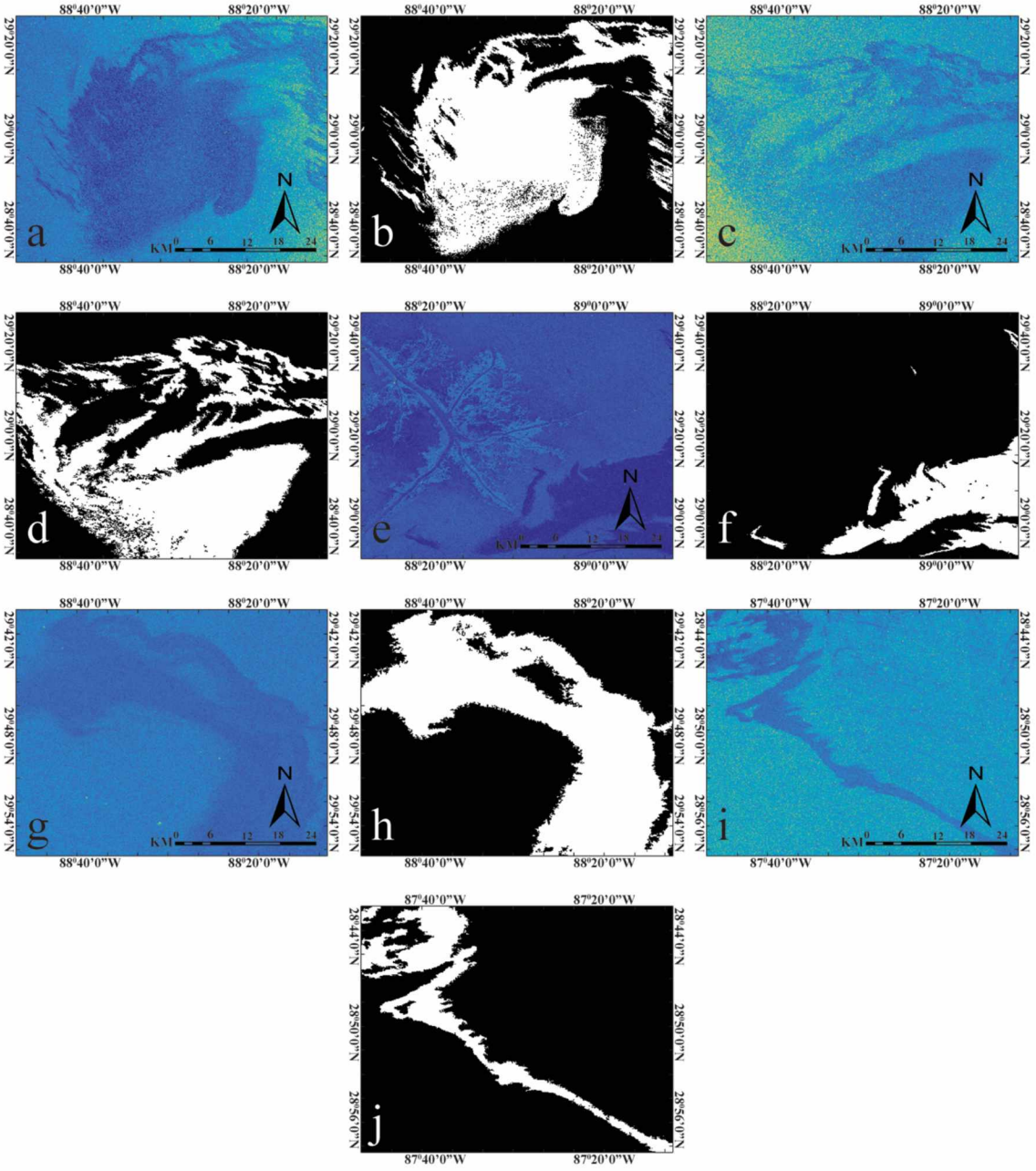

Figure 4.16. Images a, c, e, g and i show the original amplitude images, while image b, d, f, h, and j show each of their corresponding oil spill classification map after applying SLICK approach. The original amplitude images are repeated here for comparison.

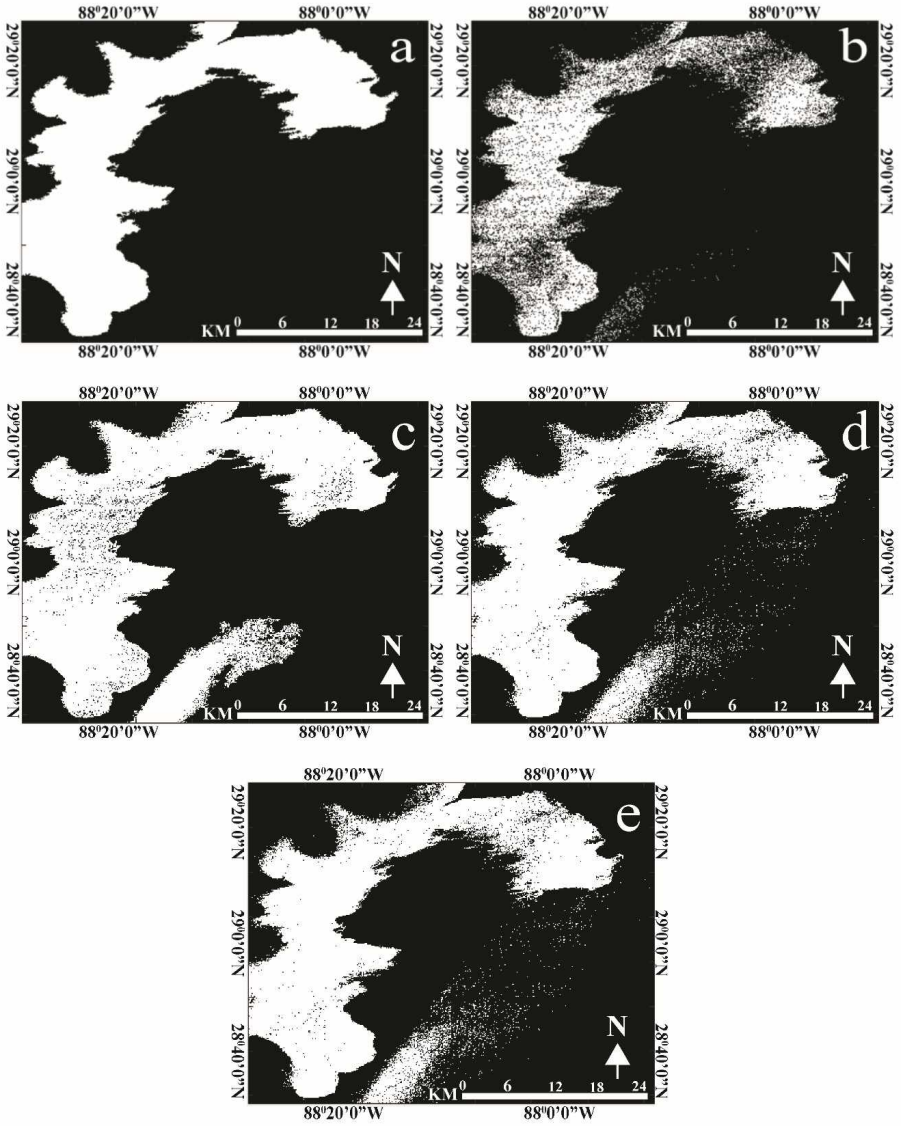

Figure 4.17. Oil spill change detection maps showing (a) adapted approach, (b) reference method A; (c) reference method B; (d) reference method C; and (e) reference method D.

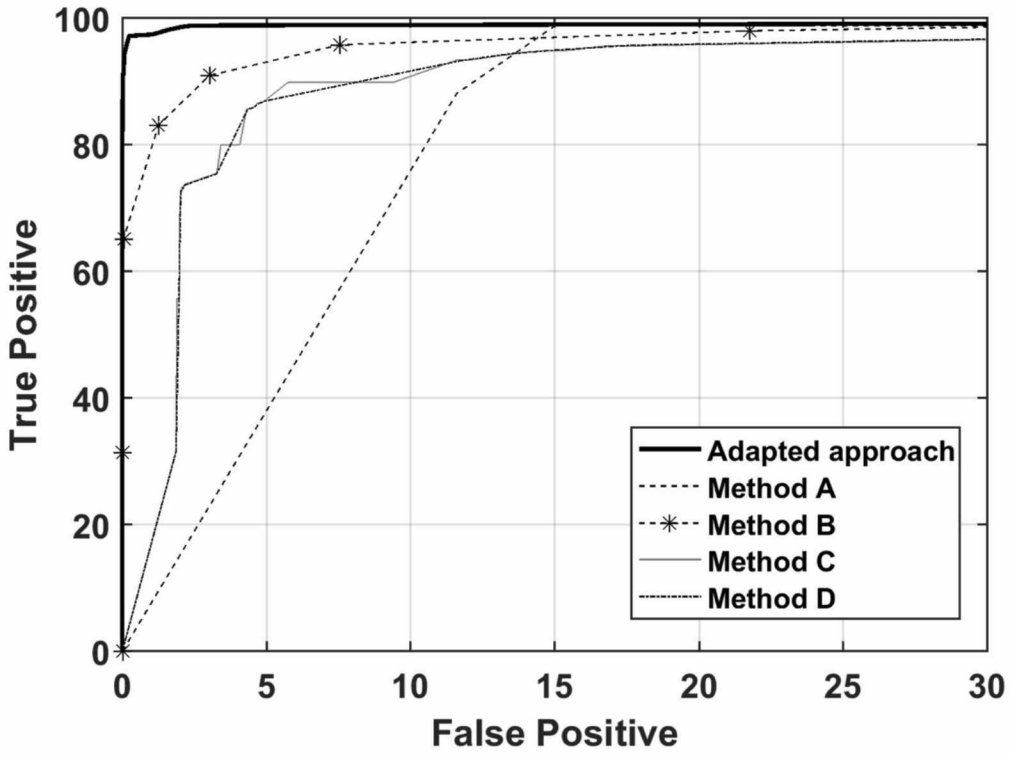

Figure 4.18. The ROC curves of the adapted approach and alternative methods.

Table 4.1. False alarm, missed hit, and kappa coefficient of our adapted approach versus DSD.

	False Alarm (%)	Missed Hit (%)	Kappa Coefficient
L-band change Detection			
Adapted approach	0.11	1.81	0.97
DSD	1.79	1.31	0.76
X-band change Detection			
Adapted approach	0.22	0.24	0.93
DSD	1.90	0.75	0.59

Table 4.2. Combination of image acquisitions used to generate the ratio images for oil spill change detection

Pre-event	Post-event	AOI	Figure	Sensor
25-Apr-2010	25-Apr-2010	AOI 1	4.15(b)	
25-Apr-2010	30-Apr-2010	AOI 2	4.16(b)	
25-Apr-2010	01-May-2010	AOI 3	4.16(d)	TerraSAR-X
25-Apr-2010	15-May-2010	AOI 4	4.16(f)	
28-May-2010	28-May-2010	AOI 5	4.16(h)	PALSAR
28-May-2010	26-Jun-2010	AOI 6	4.16(j)	

Table 4.3. False alarm, missed hit, and kappa coefficient of our adapted approach with different approaches using AOI 1

	False Alarm (%)	**Missed Hit (%)**	**Kappa Coefficient**
Adapted approach	0.07	5.56	0.96
Method A	0.37	40.30	0.66
Method B	8.16	5.63	0.83
Method C	4.16	11.23	0.85
Method D	4.17	11.23	0.85

Table 4.4. Comparison of each change detection method with one another using Wilcoxon Signed Rank Test and p-value of 0.05

	Adapted approach	**Method A**	**Method B**	**Method C**	**Method D**
Adapted approach					
Method A	2.5e-10				
Method B	3.4e-04	2.62e-03			
Method C	3.3 e-11	8.6 e-04	2.3e-01		
Method D	2.4 e-11	1.0 e-03	2.1 e-01	5.6 e-01	

e = exponential

Chapter 5 Detection of Aufeis-related Flood Areas in a Time Series of High Resolution Synthetic Aperture Radar Images using Curvelet Transform and Unsupervised Classification [1]

5.1. Abstract

Synthetic Aperture Radar (SAR) images have been recognized as a valuable data source for mapping ice and open water in cold regions. Compared to other sources, SAR's weather and illumination independence and large area coverage at high spatial resolution support frequent and detailed observations. Accordingly, SAR's has potential in supporting near real-time monitoring of natural hazards, such as a flood detection, if combined with automatization in the image processing. We utilized a change detection approach based on wavelet analysis to map aufeis-related flooding on the Sagavanirktok River in northern Alaska. We here define aufeis flooding as the combination of ice and open water prior to the onset of snowmelt. The flood detection technique was applied to a time-series of multi-temporal SAR images and we included a tile based technique to increase the classification accuracy and to delineate smaller flooded areas. We implemented the curvelet filtering method to preserve the full resolution of the original SAR data while reducing the influence of speckle on flood detection performance. Curvelet filters have a high degree of directionality and give a sparse representation of curved features. Furthermore, we estimated the expected value for each change class using an intensity thresholding technique to perform automatic classification using probabilistic Bayesian inferencing. Finally, we incorporated a time-series analysis technique in our workflow to understand the various type of aufeis-related change in our study area.

This paper provides near real-time monitoring by generating detailed flood parameters such as flood classification probabilities, flood-related backscatter changes, and flood extent. The

generated flood maps show the spatial extent and day-to-day progression of the 2015 aufeis flooding event across a 1004 km^2 area as determined from a series of seven TerraSAR-X datasets. Warm air temperatures appeared to have led to accelerated aufeis growth. The tool can help decision-makers obtain critical information on near-real time aufeis flood extent in order to reduce damages and provide effective emergency relief.

---

[1] Ajadi, O.A.; Meyer, F.J.; Liljedahl A (2017), Detection of aufeis-related flood Areas in a Time Series of High Resolution Synthetic Aperture Radar Images using Curvelet Transform and Unsupervised Classification, Prepared for submission to *IEEE Journal of Selected Topics in Applied Earth Observations and Remote Sensing* 2017.

5.2. Introduction

During recent years, climate change and the increasing frequency of extreme weather events have been widely recognized as a serious environmental problem (National Academies of Sciences and Medicine, 2016). Changes in the climate have led to an increase in natural disaster such as flood, tsunami, and hurricane (Van Westen and Soeters, 2000). Near real-time monitoring and surveillance processes can help provide an overview of a disaster situation, increase response activities, and improve crisis management. Remote sensing is a powerful tool to aid near real time monitoring (Matgen et al., 2011) and especially in remote regions like the Arctic when on-the-ground monitoring is especially complicated due to limited infrastructure.

Spring flooding is a yearly phenomenon in the Arctic as more than half of the annual precipitation is released within a ~10-day period (Kane et al., 2012a). Snowmelt flooding can be further complicated by extensive build-up of ice, so called "river aufeis", through the winter within the river channel itself. The term ''aufeis'' is of German origin and means ''on or upon

ice'' (Grey and MacKay, 1979). Aufeis forms when groundwater seeps and freezes to the ground surface or when river water freezes to the riverbed, forming a mass of ice layers with different ages. Aufeis forms throughout the mid to late winter, but can persist through a portion of the summer (Yoshikawa et al., 2007). Flooding related to aufeis growth may occur in late-winter because the slow (weeks to months) but massive growth of the aufeis ice diverts the winter streamflow (and therefore more aufeis growth) far beyond the original river channel. Flooding related to aufeis growth can also be seen during the spring snowmelt event as the aufeis diverts snowmelt water outside the river channel (Prowse, 1995). In this paper forward, we refer to aufeis flooding or aufeis growth as winter river discharge freezing to the streambed and it includes both ice and any water flowing on top of the ice.

Aufeis flooding poses a serious threat to lives and infrastructure in the Arctic. The aufeis and its overflowing water often overwhelm culverts and stream channels and numerous cases have been cited where aufeis flooding encroaches on roadways, endangering traffic (Carey, 1973). The secondary danger emerges in the spring when the ice-filled stream channels are unable to handle the snowmelt runoff, which increases the snowmelt flooding potential (Prowse, 1995). For example in April of 2015, Alaska's Governor issued a 15 million dollar disaster declaration for aufeis-related late winter and snowmelt flooding on Dalton Highway, North Slope (Brettschneider, 2015). Remote sensing can be a useful tool for near-real time mapping of aufeis growth and to inform disaster management.

Several remote sensing techniques have proven useful in mapping aufeis, including Landsat (Dean, 1984; Hall and Roswell, 1981; Harden et al., 1977) and Synthetic Aperture Radar, SAR (Benson et al., 1997; Yoshikawa et al., 2007) as frozen and thawed water results in different reflection and emittance of electromagnetic radiation. Satellite imagery and aerial photography

have been used to quantify aufeis distribution, spring water temperature, discharge volume, relative age of spring formation, aufeis historical extent, and estimations of winter baseflow (Yoshikawa et al., 2007). The 24/7 capability and regular observation schedule of modern SAR sensors are ideal for near-real time monitoring (Martinis et al., 2009; Matgen et al., 2011; Pulvirenti et al., 2011a) and can therefore reveal a wealth of information about aufeis distribution and change. With the goal to map aufeis flooding in near-real time, we applied an unsupervised change detection to a multi-temporal SAR dataset. The approach has been effective in delineating regions of fire scar at 12.5 m resolution across 45 km domains at sub-daily frequencies (Ajadi et al., 2016).

5.3. Background

This section provides an overview of the state of the art regarding flood detection techniques. It should be noted that a comprehensive review of the enormous amount of published work will not be presented here, but this section will give an idea of the principal research approaches. In the last decade, SAR remote sensing techniques due to their increase in temporal resolution have become a promising tool for flood mapping.

In temperate regions, natural disasters have primarily been mapped using various approaches that utilized SAR images. SAR has been a sensitive sensor for aufeis detection and mapping in high latitudes (Jeffries et al., 1994), river ice breakup monitoring (Floyd et al., 2014), and for observing shallow lake thaw/freeze conditions (Jeffries et al., 1994). The Alaska Satellite Facility at the University of Alaska Fairbanks, provides SAR data to the National Weather Service for river breakup monitoring of the Koyukuk and Sagavanirktok Rivers, Northern Alaska.

In order to reduce human interaction during aufeis SAR-based flood detection, an unsupervised change detection approach have always been employed. Unsupervised SAR-based flood detection methods have been published throughout the last decade on temperate regions and utilizing a binary single-polarization approach (Martinis et al., 2009; Matgen et al., 2011). For example, flood areas have been extracted using a split-based automatic thresholding approach (Martinis et al., 2009). Some authors claimed that the addition of spatial information to the pure spectral information derived from histogram thresholding is superior to pixel-based procedures (Martinis et al. (2009) Matgen et al. (2011)). However, this method depends upon contrasts between flooded and non-flooded regions, which may sometimes be lacking. Flooding has been identified via SAR by searching for areas with low backscatter values, which are associated with open water. Here, the extracted open water bodies are used as "seeds" in a region-growing, iterated, segmentation/classification approach (Giustarini et al., 2013). The method is limited because it is time consuming and it requires a reference image with the same imaging characteristics as the flood image, which may not be available during a crisis event. Flood extent has also been delineated automatically using active contour modeling (Mason et al., 2007), which reduces the SAR speckle noise, but requires a prior knowledge of the image's statistical properties. Further, it is imperfect when the initial contour is far from the object boundary. Another method is the fuzzy logic approach, which integrates theoretical knowledge about the radar return from inundated areas based on three electromagnetic scattering models by simple hydraulic considerations and contextual information (Pulvirenti et al., 2011b). Here the limitations are the manual procedure and the high computational demand.

Automated hybrid methodologies, which combine radiometric thresholding and region-growing of SAR images, offered comparable performance with the previously mentioned

methods for the extraction of flood area, despite not requiring any ground truth data (Matgen et al., 2011). However, the hybrid approach is constrained to only bimodal distribution of backscatter values. More recently, Pradhan et al. (2016) generated a flood extent map using a Taguchi optimization technique, multiresolution segmentation, and rule-based classification. An object-oriented rule-based classification method was used to extract water bodies from TerraSAR-X data during the flooding, while Landsat imagery was utilized prior to the flood event. Water bodies from the Landsat imagery were then subtracted from the TerraSAR-X data and the remaining water represented the flooded area. The dependence of Landsat imagery makes this multi-facetted approach limited as Landsat imagery is complicated by clouds. Other fairly recent work done in flood detection includes automatic thresholding on feature maps using minimum-error procedure (Bazi et al., 2005; Moser and Serpico, 2006), fractal dimensioning of multi-temporal images (Huang et al., 2011), statistical active contouring (Horritt et al., 2001), histogram thresholding or clustering (Inglada and Mercier, 2007), the application of neural networks in a grid system (Kussul et al., 2008), and expectation-maximization algorithms (Byun et al., 2015). All published flood detection methods were applied to only open water and not aufeis flooding, which includes both open water, new or older ice, and snow. Monitoring and mapping the extent of aufeis flooding is therefore more complex than mapping solely open water areas.

5.4. Methodology for Flood Detection

In order to achieve an accurate flood detection result in near real-time, a flood detection approach should possess the following key features: (i) that the generation of the flood maps should be accomplished automatically without setting thresholds and include a high computational performance; (ii) the flood mapping approach should be highly predisposed

against noise; (iii) the approach should be easily transferable to different geographical conditions and should support various SAR frequencies with different resolution; (iv) the approach should be free of a priori assumptions; and (v) the approach should accurately delineate the boundary of flooded regions.

While adapting the approach published in Ajadi et al. (2016), we focused on ensuring the delineation of flood extent with high accuracy in both border and homogeneous regions. To achieve high accuracy, we followed the modified processing steps presented in Figure 5.1. In our modified approach, we included image tiling, curvelet filtering, intensity thresholding, and Bayesian inferencing to those already implemented in Ajadi et al. (2016). The newly included techniques are explained in details in the following subsections, while the previously published technique in Ajadi et al. (2016) is only briefly explained and the reader is referred to that publication for more details.

5.4.1. Standard Pre-processing

For each image acquired, standard pre-processing is performed to suppress all image signals other than surface change that may introduce radiometric differences between acquisitions. All images are radiometrically corrected using a SRTM DEM. The impact of including radiometric correction on the SAR data is not observable in our images, because our study area is flat. Radiometric terrain correction is most effective when dealing with natural environments that are dominated by rough surface scattering. However, to develop a technique that is transferrable to other geographical domains we ensured that this RTC step was included for all SAR data we analyzed. For these target types, the surface scattering properties change slowly with incidence angle, and differences in radar brightness are dominated by geometric effects. For more information about the pre-processing step, the reader is referred to Ajadi et al. (2016).

5.4.2. Data Enhancement

5.4.2.1. Problem Formulation and Image Tiling

To increase the speed for mapping purposes, a tile-based approach is employed. Here, each coregistered SAR image is split into k nonoverlapping subimages of user defined size. The tile-based approach is preferred because smaller flood areas are more easily detected, and have a lower rate of false positives with highly reduced computational complexity. To enhance the curvelet filtering step in Section 5.4.2.2, each k subimages are logarithmically transformed (X_{LR}^{k}), and its multiplicative noise is converted into additive noise. For more information about the logarithmic transformation, the reader is referred to Ajadi et al. (2016). To improve the detectability of flood-induced changes, and to suppress image background structure, the logarithmic transformation subimages from image X_i (post-event image) and the logarithmic transformation subimages from image X_r (pre-event image) which are acquired over the same geographical areas at two different times ($t1\ and\ t2$) are used to generate k ratio subimages.

Observing each k^{th} ratio subimage (X_{LR}^{k}), aufeis areas appear bright with an increased backscatter, while open water appears dark with a decreased backscatter due to specular reflection. For the purpose of flood detection, the histogram of each X_{LR}^{k} was treated as a mixture of three classifications: positive change (ω_{pc}) which are aufeis areas, negative change areas (ω_{nc}) which are open water areas, and unchanged areas (ω_{un}). Our analysis was only done on each X_{LR}^{k} containing at least a bimodal distribution rather than a unimodal distribution.

$$\Delta_{bd} = \Delta_{bd}^{k} \dots\dots\dots\dots\dots, \Delta_{bd}^{K-1} \tag{5.1}$$

where Δ_{bd} are subimages with at least a bimodal distribution. To suppress the now-additive noise contained in each Δ_{bd} subimage, we applied a curvelet transform filtering procedure.

5.4.2.2. Filtering by Curvelet Transform

We took advantage of using a curvelet transform in denoising each Δ_{bd} subimage. A curvelet transform was employed because it gives a sparse representation of curved features, and it preserves curved structures. It also has a very high degree of directionality and few coefficients are used when approximating its singularities. Curvelet was first introduced by Candes and Donoho (1999) and has been used by Starck et al. (2002) among others for image denoising. The curvelet is a multiscale transform with the magnitude of its coefficient depending on the linear feature indexed by location, orientation, and scale parameters. To perform curvelet filtering and to remove point-like noise, we inspect the data for objects having a curvelet coefficient larger than a minimum size determined automatically by noise standard deviation. Even though wavelet transform can also be used for filtering purposes, the curvelet transform is superior because of its sensitivity to linear features. In this paper, we assumed that a noisy sub-image in Δ_{bd} is given by $\Delta_{bd}^{k}(i,j) = \Delta_{ri}^{k}(i,j) + \sigma^{k}$. Where σ^{k} is the noise standard deviation in $\Delta_{bd}^{k}(i,j)$, and $\Delta_{ri}^{k}(i,j)$ is the restored subimage after denoising with curvelet transform. The restored subimage (Δ_{ri}^{k}) is estimated by applying thresholding to each curvelet coefficient in Δ_{bd}^{k} at every scale using σ. The curvelet coefficients are estimated using the fast discrete curvelet transform and implementing the wrapping-based method as shown by Candès et al. (2006). Furthermore, σ was calculated using Median Absolute Deviation (MAD) of the high frequency (horizontal, vertical and diagonal) wavelet coefficients (ω_k) in Δ_{bd}^{k}. The value of σ is estimated as follows:

$$\sigma = \frac{median(|\omega_k|)}{0.6745} \tag{5.2}$$

We employed hard thresholding because soft thresholding tends to create smoothness along edges by removing some edge coefficients. The wrapping-based Fourier sample method with hard thresholding implemented in this paper is summarized into five steps.

Step 1: Is the application of two dimensional fast Fourier Transform (2D FFT) to Δ_{bd}^{k}, which is in the form of a Cartesian array $\Delta_{bd}^{k}[m,n]$ to obtain Fourier coefficients.

$$\hat{\Delta}_{bd}^{k}[m,n], \qquad -\frac{n}{2} \leq m,n < \frac{n}{2} \tag{5.3}$$

where $0 \leq m < M, 0 \leq n < N$, while M and N are the dimension of the array.

Step 2: For each scale (j) and angle (l), a product of $(fft(curvelet))$ and $(fft(image))$ is obtained to form a trapezoidal wedge.

$$\widetilde{W}_{j,l}{}^{k}[m,n].\hat{\Delta}_{bd}^{k}[m,n] \tag{5.4}$$

Step 3: The product is now wrapped around the origin.

$$\hat{\Delta}_{j,l}^{k}[m,n] = wrap\left(\widetilde{W}_{j,l}{}^{k}\hat{\Delta}_{bd}^{k}\right)[m,n] \tag{5.5}$$

where $j = floor\ (log2(min\ (M,N))\ - 4)$, while the range of $m,n\ and\ \theta$ are now $0 \leq m < 2^{j}, 0 \leq n < 2^{j/2}$, and $-\frac{\pi}{4} \leq \theta < \frac{\pi}{4}$ respectively.

Step 4a: Use the calculated σ from Equation (2) to perform hard thresholding on $\hat{\Delta}_{j,l}^{k}[m,n]$ for the coarse scales

$$\hat{f}_{j,l}^{k} = \begin{cases} \hat{\Delta}_{j,l}^{k}[m,n], & if \quad abs\left(\hat{\Delta}_{j,l}^{k}[m,n]\right) > 3 * \sigma^{k} \\ 0, & otherwise \end{cases} \tag{5.6}$$

Step 4b: Use the calculated σ from Equation (2) to perform hard thresholding on $\hat{\Delta}_{j,l}^{k}[m,n]$ for the fine scale

$$\hat{f}_{j,l}^{k} = \begin{cases} \hat{\Delta}_{j,l}^{k}[m,n], & if \quad abs\left(\hat{\Delta}_{j,l}^{k}[m,n]\right) > (3 * \sigma^{k}) + \sigma^{k} \\ 0, & otherwise \end{cases} \tag{5.7}$$

Step 5: Perform inverse fast discrete curvelet transform via wedge wrapping on $\hat{f}_{j,l}^{k}$ to get the denoised subimage Δ_{ri}^{k}.

Applying the six steps highlighted above to all subimages in Δ_{bd} will generate k denoised subimages $\Delta_{ri} = \Delta_{ri}^{k} \dots\dots\dots\dots\dots, \Delta_{ri}^{K-1}$.

5.4.3. Wavelet-Based Flood Detection Algorithm

5.4.3.1. Multi-scale Analysis Combined with Opening by Reconstruction for Flood Detection

In this paper, given the k^{th} denoised subimage in Δ_{ri}, a multi-scale representation of Δ_{ri}^{k} is obtained by applying two-dimensional discrete stationary wavelet transform (2D-SWT). The goal of the multi-scale representation is to achieve a different scale dependent image of varying resolution. The lowest resolution contains some residual noise and a high amount of geometric detail, while the highest resolution contains reduced noise interference, and reduced geometric content. The multiscale images of Δ_{ri}^{k} are inserted into a mathematical morphology framework, where opening by reconstruction is employed, and the result is further normalized to a range of 0 to 255. The multiscale decomposition stack of Δ_{ri}^{k} now contains morphological filtered images (X_{MD}) at each resolution level, as below:

$$X_{MD} = \left\{X_{MD}^{0}.., X_{MD}^{l} \dots\dots\dots.., X_{MD}^{L-1}\right\} \tag{5.8}$$

For more information about the implementation of the multi-scale representation, and the mathematical morphology the reader is referred to Ajadi et al. (2016).

5.4.3.2. Intensity Threshold Segmentation

To perform Bayesian inferencing (Section 5.4.3.3) for classification, an initial estimate (mean, prior, and standard deviation) of each class should be known. Because no prior

knowledge is available for the distribution of classes, we employed the intensity segmentation approach proposed by Otsu (1975) to compute the initial estimate for each class. The intensity segmentation approach uses histogram distributions to calculate the initial estimate needed to compute the likelihood that each pixel belongs to a certain class. The approach finds the threshold that minimizes the weighted within-class variance.

5.4.3.3. Probabilistic Bayesian Inferencing Flood Extent Approach

For each pixel in X_{MD}^{l}, our goal is to calculate the probability that a pixel belongs to a set of predefined classes given its measured backscatter value, and the pixel is given to the class with the highest probability. First, we assumed that the distribution of non-flooded unchanged backscatter (ω_{uc}) and flooded (aufeis and open water) changed backscatter (ω_{c}) in X_{MD}^{l} are a mixture of $three$ density distributions:

$$p(X_{MD}^{l}) = \sum_{n=1}^{2}\left(p(X_{MD}^{l}|w_{c}^{n})P(w_{c}^{n})\right) \; + \; p(X_{MD}^{l}|\omega_{uc})P(\omega_{uc}) \tag{5.9}$$

Given the initial estimate of mean, prior, and standard deviation calculated from the previous section, we can further estimate the posterior probability of a pixel being flooded using Bayes' theorem as follows:

$$P\left(\omega_{i}|X_{MD}^{l}(i,j)\right)_{\omega_{i}\in\{\omega_{pc},\omega_{nc},\omega_{uc}\}} = \frac{p\left(X_{MD}^{l}(i,j)|\omega_{i}\right) * P(\omega_{i})}{p(X_{MD}^{l})} \tag{5.10}$$

where ω_{pc} indicates positive backscatter change (aufeis areas), ω_{nc} represents negative backscatter change (open water areas), ω_{uc} denotes unchanged backscatter, $p\left(X_{MD}^{l}(i,j)|\omega_{i}\right)$ and $P(\omega_{i})$ denotes the likelihood and prior probability of a pixel respectively. For more information about the implementation of Bayes' theorem, the user is referred to Ajadi et al. (2016).

It is worth noting that the choice of employing probabilistic Bayesian inferences was to capture the overall variation of the flood extent, and to generate a flood detection approach with low computational performance.

5.4.3.4. Product Rule Fusion

After the Bayesian inference classification, the final change detection maps were generated by applying a product rule fusion, similar to the approach in Ajadi et al. (2016), to the posterior probabilities (PP) of each decomposed image in X_{MD} at each spatial position. Each pixel is assigned to the class that maximizes the posterior conditional probability as follows:

$$\omega_i = \underset{\omega_i \epsilon \{\omega_{pc}, \omega_{nc}, \omega_{uc}\}}{\operatorname{argmax}} \prod_{i=0}^{K} \{P(\omega_i | X_{MD}^k(i,j))\} = \underset{\omega_i \epsilon \{\omega_{pc}, \omega_{nc}, \omega_{uc}\}}{\operatorname{argmax}} \prod_{i=0}^{K} \{PP^i\} \quad (5.11)$$

5.4.4. Application for High Resolution TerraSAR-X Data at the Sagavanirktok River

5.4.4.1. Study Area

To assess the effectiveness of the modified flood detection approach, we evaluated several TerraSAR-X datasets acquired during a period of flooding on the Sagavanirktok River, near Prudhoe Bay, Alaska in 2015 (Figure 2). On Alaska's North Slope, the Sagavanirktok ("Sag") River (14,900 km^2) is the second largest watershed and it flows northward into the Beaufort Sea, Arctic Ocean. The headwaters of this ~270 km long river are located in the Brooks Range, where mountain peaks reach 2475 m. Over 50% of the watershed lies in the mountains (Kane et al., 2014) and there is an abrupt decline in slope as the river reaches the foothills (Keller et al., 1961). Annual air temperatures average -10.5 °C in the coastal plain to -7.7 °C in the foothills (Kane et al., 2014) with air temperatures during the nine months long winter reaching down to -40 °C. The annual precipitation ranges from 140 mm (coastal plain) to 340 mm (mountains)

(Kane et al., 2014). Summer precipitation varies significantly with much greater amounts in the mountains and foothills regions, while end-of-winter snow accumulation is fairly uniform (Kane et al., 2012b). Annual peak flow may be snowmelt or rainfall generated (Kane et al., 2014). North Slope aufeis starts to develop in October and increases dramatically in late winter, while aufeis releases water during the summer months that is estimated to represent 30% of total annual groundwater discharge for the nearby Kuparuk River (Yoshikawa et al., 2007). Aufeis is relatively extensive in the headwaters of the Sag River where an area between 10^2 to 10^3 km^2 melts each summer (Benson et al., 1997). Large buildups of river aufeis are regularly observed near Franklin Bluffs within the Sagavanirktok River channel in late winter ((Toniolo et al., 2017).

Meteorological variables such as daily air temperature were obtained to help interpret the overall formation of aufeis. The daily air temperature data were acquired from the National Oceanic and Atmospheric Administration (NOAA) Deadhorse 3 station, with station ID USW00026565, latitude 70°09'42.5"N and longitude 148°27'51.8"W (Figure 5.2). Additional information about the daily air temperature data is available at www.ncdc.noaa.gov.

5.4.4.2. SAR and Reference Data

The German space agency (DLR) maintained TerraSAR-X and acquired several images beginning in early April 2015 to early May 2015 (Table 5.1 and Figure 5.3). The images acquired are in strip map mode, with a single HH polarization. Using HH polarization is more promising for use in flood mapping than VV polarization or cross polarization because it is less sensitive to small scale roughness of waves on the water surface (Henry et al., 2006). The pixel spacing in each image is 1.25 m x 1.25 m with incidence angles ranging from 24° to 41°.

Twelve different independent log-ratio images (observation periods 1–12 in Table 5.2) were generated from the seven TerraSAR-X images, and these log-ratio images were used to analyze both the progression of the flood event during the observation periods and the performance of our modified change detection approach. The first six log-ratio images with longer temporal intervals were generated using the earliest image acquisition as our pre-flood image and the remainder as post-flood images (observation periods 1–6 in Table 5.2). The last six log-ratio images, each with shorter temporal intervals, used the next earliest acquired image as a pre-flood image and the succeeding image as the post-flood image (observation periods 7–12 in Table 5.2).

5.4.5. Description of Approach

To increase detection speed and accuracy, each pre-event and post-event image was split into eight equal sub-images ($k = 8$). For each observation period, eight log-ratio sub-images were generated from the pre-event and post-event subimages. Each log-ratio subimage was filtered using a curvelet approach, with noise filtered out using hard thresholding, and σ calculated at 0.3. Next, each of the eight, filtered, log-ratio sub images were decomposed into three resolution levels using a 2D-SWT with the bi-orthogonal wavelets family. For each of the three-resolution levels, we calculate the posterior probability of one “unchanged”, one "negative changed" and one “positive changed” class, resulting in three posterior probabilities per pixel. Finally, product rule fusion is used to merge the posterior probabilities of all the three-resolution levels to produce a single change map (M). The complete flood detection map (CD) for each observation period is generated by combining the corresponding eight change maps (M).

$$\underset{i=1,\ldots..12}{CD(i)} = \{\underset{k=1,\ldots..8}{M^1 \ldots \ldots M^k}\} \tag{5.12}$$

5.5. Results and Discussion

The modified flood detection approach produced no noise in delineating areas into aufeis and open water. The results of applying our modified flood detection approach to observation periods 1 - 6 with long temporal intervals (Table 5.2) is shown in Figure 5.4. Visually observing Figure 5.4a, an accumulation of aufeis on the western channel of the Sagavanirktok River is extending onto the Dalton Highway. As time passes (progression from Figure 5.4b to Figure 5.4d), the accumulation of aufeis increases and open flood water emerges from the eastern channel of the Sagavanirktok River (Figure 5.4e and Figure 5.4f).

The growth in total flooded areas (both aufeis and open water) during the observation periods 1 - 6 ranges from 32.8±5 km^2 (April 13-15) to 104.1±5 km^2 (Apr 26-May 5) (Figure 5.5). The growth was gradual except for a large increase in late April-early May. The high spike in the flooded area seen in May was because of warm temperatures leading to more open water flooding.

The results of applying our modified flood detection approach to observation periods 7 - 12 with short temporal intervals (Table 5.2) is shown in Figure 5.6. The short temporal interval results shown here help to better understand the often-rapid transition between the formation of open water and successive aufeis development (Figure 5.6). Qualitatively, when analyzing Figures 6a to 6f, a fluctuation in the distribution of aufeis to open water can be seen.

Based on results generated in Figure 5.6, the flooded area (both aufeis and open water) covered by observation periods 7 - 12 ranges from 32.8±5 km^2 (April 13-15) to 47.4±5 km^2 (May 5-May 7) (Figure 5.7). According to results shown in Figure 5.7, the flooded areas (both aufeis and open water) over time have small variations with peak flooded area in May. The drop down in area on April 19 was because few areas changed between April 15 and April 19.

For example, to show the fluctuation of aufeis and open water, a photo was acquired by UAF on May 15, 2015 along the Dalton highway, with a clear distribution of aufeis (Figure 5.8a). By May 17, the entire area previously covered with aufeis has now been covered with open water (Figure 5.8b).

Comparing a plot of average daily air temperature (Figure 5.9) to aufeis and open water distribution in Figure 5.6a to Figure 5.6f we observed a relationship. For example, the decrease in temperature from April 13 to April 15, 2015 in Figure 5.9 was consistent with the formation of aufeis in Figure 5.6a due to freezing temperature. The increase in temperature from April 15 to April 19, 2015 (Figure 5.9) led to reduction in aufeis distribution (Figure 5.6b). This warmer temperature resulted in the emergence of open water. Furthermore, the increase in warmer temperature from April 19 to April 24, 2015 (Figure 5.9), steered the generation of more open water (Figure 5.6c), while the decreases in temperature seen from April 24 to April 26, 2015 (Figure 5.9), resulted in a new distribution of aufeis as a result of the freezing temperatures (Figure 5.6d). From April 26 to May 5, 2015 there was an increase in air temperature (Figure 5.9) which led to a new occurrence of open water as shown in Figure 5.6e. Finally, the slight temperature decrease from May 5 to May 7, 2015 seen in Figure 5.9, led to a new episode of aufeis as shown in Figure 5.6f.

To show the distribution of flow in areas of aufeis over time, we combined all the areas of aufeis in Figure 5.6 together and displayed it in Figure 5.10. It can be seen that the distribution of flow over time is moving from the western to the eastern channel of the Sagavanirktok River (Figure 5.10). Monitoring the direction of flow is essential to Alaska department of transportation, because knowing the direction will help to prioritize response efforts.

To appreciate the local fluctuation from aufeis to open water, the reader is referred to the

southern part of the flooded maps in Figure 5.6. For this area, a mask identifying a region that has experienced several aufeis episodes over the observed time frame is shown (Figure 5.11). The average backscatter of the masked area in each of our SAR acquisitions is shown in Figure 5.12. A relationship is highlighted between the average change in backscatter intensity (Figure 5.12) and daily average air temperature (Figure 5.9) when plotted together (Figure 5.13).

We speculate the steady increase in brightness from April 19 to April 26 is because of the gradual thickening of the aufeis area. Similar observations to strengthen our findings were also expressed by Jeffries et al. (1994) at Barrow Alaska.

5.5.1. Reliability of the Probabilistic Flood Map Approach

According to field work done by UAF (Toniolo et al., 2015) at the time, we noticed some additional areas of aufeis were detected in Figure 5.4e. These additional areas resulted from channels that were constructed to remove water from the road. They appear bright in the SAR images acquired in late April due to the piling of snow next to the narrow channels of water. In this paper, we do not have a ground truth mask to perform a quantitative analysis. However, we compared visually a flood map generated from the probabilistic flood map approach using the panchromatic band of a Landsat-8 image to a TerraSAR-X image. We choose the panchromatic band of Landsat-8 because of its 15m spatial resolution. For comparison, we used the dataset from observation period 10. We selected only observation period 10 as the Landsat-8 image at the same approximate date has minimal cloud cover. Flood maps generated from observation period 10 using TerraSAR-X and Landsat 8 are shown in Figure 5.14a and Figure 5.14b respectively. When qualitatively comparing TerraSAR-X and Landsat-8 classified results, the active SAR sensor showed little to no misclassification and this was mostly due to its high spatial resolution and its high capability in detecting surface roughness and water bodies. Using the

TerraSAR-X data, shadow and layover did not have a significant influence as most of the area is flat. However, there were some misclassifications in the flood map generated by Landsat-8 due to: (a) the influence of the minimal cloud cover in the Landsat-8 scene; (b) the high spatial resolution of the Landsat-8 panchromatic band. It should be noted that the Landsat-8 image was acquired in the afternoon, while the TerraSAR-X image was acquired in the morning. The difference in the image time acquisition could also have affected the result. In all, the flood maps generated by our adapted approach in Figure 5.14a and Figure 5.14b showed similar distribution of aufeis and open water. These similarities to some extent show that our adapted approach can be used for efficiently mapping aufeis related flooding.

5.6. Conclusion

Flood maps are critical for the assessment of natural hazards and in monitoring flood distribution. The use of optical sensors is often limited during flooding because of local cloud cover. In this paper, we modified an effective change detection approach that was initially published in Ajadi et al. (2016) and applied it to the problem of aufeis flood mapping in the Arctic regions of Alaska. The inclusion of the tiling technique to the original Ajadi et al. (2016) method increased our modified algorithms likelihood of detecting small flooded areas, by limiting the chances of detecting false positives and decreasing the computational time. Because of our interest in preserving the geometric details of flooded areas, we filtered each SAR image using a curvelet filtering method that adapts to the noise characteristics to reduce the noise within the data while preserving edges in the image. The inclusion of a probabilistic Bayesian inference takes the image uncertainty into account, and uses the backscatter distribution to estimate the probability of each pixel belonging to a particular class. We showed the performance of our modified approach by processing a series of seven TerraSAR-X data

covering the Sagavanirktok River flooding in northern Alaska in spring 2015. Using our modified approach, we mapped both the extent and progression of the Sagavanirktok River flooding event.

The reliability of the probabilistic flood map was assessed by (1) photos taken at Dalton highway showing distribution of aufeis with open water; (2) comparison of the expected changes with air temperature; and (3) comparing the distribution of aufeis and open water generated between TerraSAR-X imagery and Landsat 8 imagery. In all, the probabilistic flood map approach was able to delineate the flooded areas (both aufeis and open water) from the TerraSAR-X imagery and the Landsat-8 imagery.

Future work will explore integrating the probability maps generated from amplitude-based change detection with coherence maps generated from phase-based techniques to correctly delineate change features, especially in situations where the land cover ground conditions are complex. The integrated result will also be combined with field observations and hydrological models to further understand the high fluctuation of aufeis, and the estimation of discharge volume.

5.7. Acknowledgments

The TerraSAR-X data were provided by the German Aerospace center (DLR) under proposal LAN3293.

5.8. References

Ajadi, O. A., Meyer, F. J., and Webley, P. W., 2016, Change Detection in Synthetic Aperture Radar Images Using a Multiscale-Driven Approach: Remote Sensing, v. 8, no. 6, p. 482.

Bazi, Y., Bruzzone, L., and Melgani, F., 2005, An unsupervised approach based on the generalized Gaussian model to automatic change detection in multitemporal SAR images: IEEE Transactions on Geoscience and Remote Sensing, v. 43, no. 4, p. 874-887.

Benson, S. L. C., Shapiro, L., and Dean, K., 1997, Aufeis in the Ivishak River, Alaska, mapped from satellite radar interferometry: Remote Sensing of Environment, v. 60, no. 2, p. 131-139.

Brettschneider, B., 2015, Nenana ice classic 2015: breakin' up is hard to do: Alaska Climate Dispatch.

Byun, Y., Han, Y., and Chae, T., 2015, Image fusion-based change detection for flood extent extraction using bi-temporal very high-resolution satellite images: Remote Sensing, v. 7, no. 8, p. 10347-10363.

Candès, E., Demanet, L., Donoho, D., and Ying, L., 2006, Fast discrete curvelet transforms: Multiscale Modeling & Simulation, 5, no. 3, 861–899.

Candes, E. J., and Donoho, D. L., 1999, Curvelets: A surprisingly effective nonadaptive representation for objects with edges, Stanford University California.

Carey, K., 1973, Icings Developed from Surface and Groundwater: US Army Cold Regions Research and Engineering Laboratory.

Dean, K. G., 1984, Stream-icing zones in Alaska, Department of Natural Resources, Division of Geological & Geophysical Surveys.

Floyd, A. L., Prakash, A., Meyer, F. J., Gens, R., and Liljedahl, A., 2014, Using synthetic aperture radar to define spring breakup on the kuparuk river, northern alaska: Arctic, p. 462-471.

Giustarini, L., Hostache, R., Matgen, P., Schumann, G. J.-P., Bates, P. D., and Mason, D. C., 2013, A change detection approach to flood mapping in urban areas using TerraSAR-X: IEEE Transactions on Geoscience and Remote Sensing, v. 51, no. 4, p. 2417-2430.

Grey, B., and MacKay, D., Aufeis (overflow ice) in rivers 1979, *in* Proceedings Proceedings, Canadian Hydrology Symposium, v.79, p. 108-128.

Hall, D. K., and Roswell, C., 1981, The origin of water feeding icings on the eastern North Slope of Alaska: Polar Record, v. 20, no. 128, p. 433-438.

Harden, D., Barnes, P., and Reimnitz, E., 1977, Distribution and character of naleds in northeastern Alaska: Arctic, v. 30, no. 1, p. 28-40.

Henry, J. B., Chastanet, P., Fellah, K., and Desnos, Y. L., 2006, Envisat multi-polarized ASAR data for flood mapping: International Journal of Remote Sensing, v. 27, no. 10, p. 1921-1929.

Horritt, M., Mason, D., and Luckman, A., 2001, Flood boundary delineation from synthetic aperture radar imagery using a statistical active contour model: International Journal of Remote Sensing, v. 22, no. 13, p. 2489-2507.

Huang, S., Cai, X., Chen, S., and Liu, D., 2011, Change detection method based on fractal model and wavelet transform for multitemporal SAR images: International Journal of Applied Earth Observation and Geoinformation, v. 13, no. 6, p. 863-872.

Inglada, J., and Mercier, G., 2007, A new statistical similarity measure for change detection in multitemporal SAR images and its extension to multiscale change analysis: IEEE transactions on Geoscience and Remote Sensing, v. 45, no. 5, p. 1432-1445.

Jeffries, M., Morris, K., Weeks, W., and Wakabayashi, H., 1994, Structural and stratigraphie features and ERS 1 synthetic aperture radar backscatter characteristics of ice growing on shallow lakes in NW Alaska, winter 1991–1992: Journal of Geophysical Research: Oceans, v. 99, no. C11, p. 22459-22471.

Kane, D. L., Youcha, E. K., Stuefer, S., Toniolo, H., Schnabel, W., Gieck, R., Myerchin-Tape, G., Homan, J., Lamb, E., and Tape, K., 2012a, Meteorological and Hydrological Data and 70 Analysis Report for Foothills/Umiat Corridor and Bullen Projects: 2006–2011: University of Alaska Fairbanks, Water and Environmental Research Center, Report INE/WERC 12.01, Fairbanks, Alaska, p. 260.

Kane, D. L., Youcha, E. K., Stuefer, S. L., Myerchin-Tape, G., Lamb, E., Homan, J. W., Gieck, R. E., Schnabel, W. E., and Toniolo, H., 2014, Hydrology and Meteorology of the Central Alaskan Arctic: Data Collection and Analysis, Final Report: University of Alaska Fairbanks, Water and Environmental Research Center.

Kane, D. L., Youcha, E. K., Stuefer, S. L., Toniolo, H., Schnabel, W. E., Gieck, R. E., Myerchin-Tape, G., Homan, J., Lamb, E., and Tape, K., 2012b, Meteorological and Hydrological Data and Analysis Report for the Foothills/Umiat Corridor and Bullen Projects: 2006-2011: University of Alaska Fairbanks, Water and Environmental Research Center.

Keller, A. S., Morris, R. H., and Detterman, R. L., 1961, Geology of the Shaviovik and Sagavanirktok rivers region, Alaska: USGS.

Kussul, N., Shelestov, A., and Skakun, S., 2008, Grid system for flood extent extraction from satellite images: Earth Science Informatics, v. 1, no. 3-4, p. 105-117.

Martinis, S., Twele, A., and Voigt, S., 2009, Towards operational near real-time flood detection using a split-based automatic thresholding procedure on high resolution TerraSAR-X data: Natural Hazards and Earth System Sciences, v. 9, no. 2, p. 303-314.

Mason, D. C., Horritt, M. S., Dall'Amico, J. T., Scott, T. R., and Bates, P. D., 2007, Improving river flood extent delineation from synthetic aperture radar using airborne laser altimetry: IEEE Transactions on Geoscience and Remote Sensing, v. 45, no. 12, p. 3932-3943.

Matgen, P., Hostache, R., Schumann, G., Pfister, L., Hoffmann, L., and Savenije, H., 2011, Towards an automated SAR-based flood monitoring system: Lessons learned from two case studies: Physics and Chemistry of the Earth, Parts A/B/C, v. 36, no. 7, p. 241-252.

Moser, G., and Serpico, S. B., 2006, Generalized minimum-error thresholding for unsupervised change detection from SAR amplitude imagery: IEEE Transactions on Geoscience and Remote Sensing, v. 44, no. 10, p. 2972.

National Academies of Sciences, E., and Medicine, 2016, Attribution of extreme weather events in the context of climate change, National Academies Press.

Otsu, N., 1975, A threshold selection method from gray-level histograms: Automatica, v. 11, no. 285-296, p. 23-27.

Pradhan, B., Tehrany, M. S., and Jebur, M. N., 2016, A New Semiautomated Detection Mapping of Flood Extent From TerraSAR-X Satellite Image Using Rule-Based Classification and Taguchi Optimization Techniques: IEEE Transactions on Geoscience and Remote Sensing, v. 54, no. 7, p. 4331-4342.

Prowse, T., 1995, River ice processes, Highlands Ranch, Colorado, USA, Water Resources Publication, p. 29-70.

Pulvirenti, L., Chini, M., Pierdicca, N., Guerriero, L., and Ferrazzoli, P., 2011a, Flood monitoring using multi-temporal COSMO-SkyMed data: Image segmentation and signature interpretation: Remote Sensing of Environment, v. 115, no. 4, p. 990-1002.

Pulvirenti, L., Pierdicca, N., Chini, M., and Guerriero, L., 2011b, An algorithm for operational flood mapping from Synthetic Aperture Radar (SAR) data based on the fuzzy logic: Natural Hazard and Earth System Sciences, v. 11, no. 2, p. 529.

Starck, J.-L., Candès, E. J., and Donoho, D. L., 2002, The curvelet transform for image denoising: IEEE Transactions on Image Processing, v. 11, no. 6, p. 670-684.

Toniolo, H., Stutzke, J., Lai, A., Youcha, E., Tschetter, T., Vas, D., Keech, J., and Irving, K., 2017, Antecedent Conditions and Damage Caused by 2015 Spring Flooding on the Sagavanirktok River, Alaska: Journal of Cold Regions Engineering, v. 31, no. 2, p. 05017001.

Toniolo, H., Youcha, E. K., Gieck, R. E., Tschetter, T., Engram, M., and Keech, J., 2015, Sagavanirktok River Spring Breakup Observations 2015 Final Report.

Van Westen, C., and Soeters, R., 2000, Remote sensing and geographic information systems for natural disaster management: Roy, P..; van Westen, CJ and P. Champati Ray (Eds.): Natural Disasters and their mitigation. A Remote Sensing and GIS Perspective. Indian Institute of Remote Sensing. National Remote Sensing Agency, India, p. 31-76.

Yoshikawa, K., Hinzman, L. D., and Kane, D. L., 2007, Spring and aufeis (icing) hydrology in Brooks Range, Alaska: Journal of Geophysical Research: Biogeosciences, v. 112, no. G4.

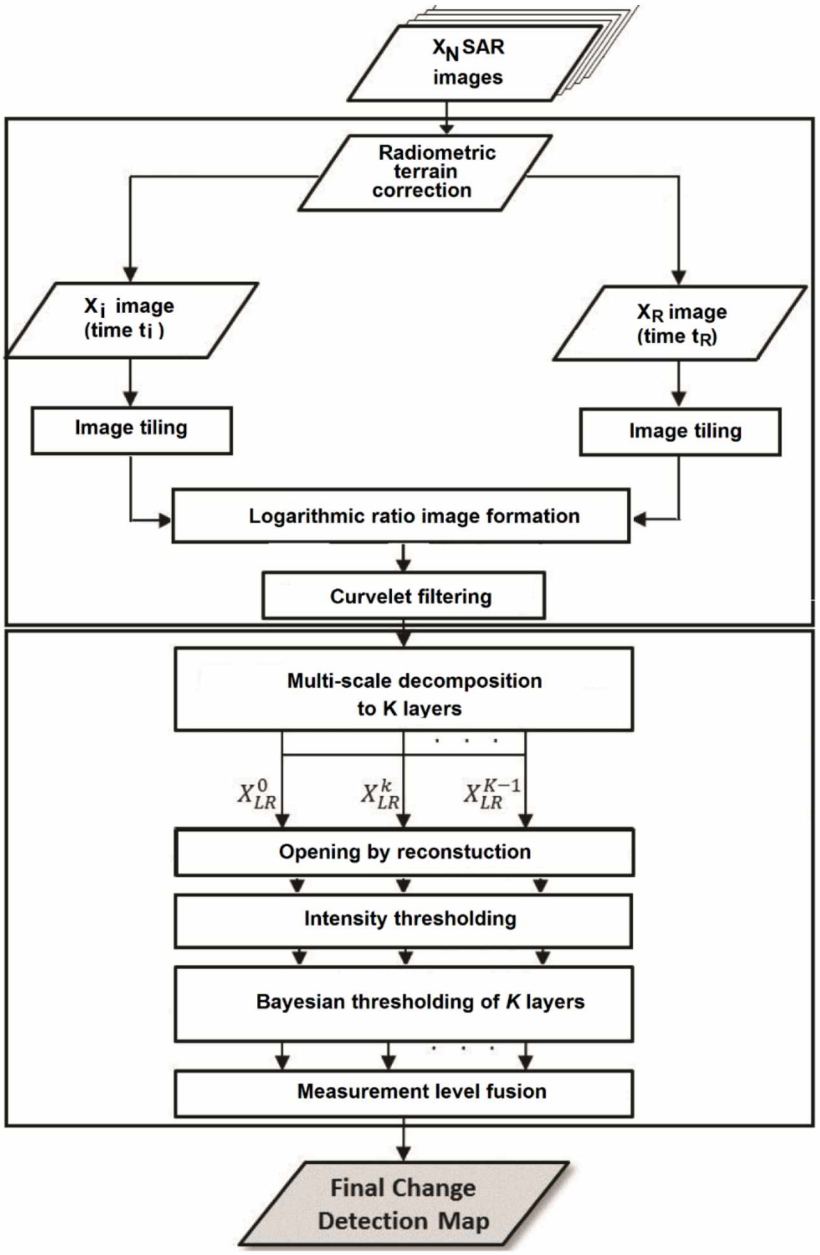

Figure 5.1. Workflow of our SAR analysis. Here $\boldsymbol{X_N SAR}$ are all the SAR images, $\boldsymbol{X_i}$ is the pre-event image at time $\boldsymbol{t_i}$ and $\boldsymbol{X_R}$ is the post-event image at time $\boldsymbol{t_R}$. The multiscale decomposition $\mathbf{X_{LR}^0}$ is the original log-ratio image, $\mathbf{X_{LR}^k}$ is the $\boldsymbol{k^{th}}$ decomposed image, $\mathbf{X_{LR}^{K-1}}$ is the lowest decomposed level, and $\boldsymbol{k}$ is the level of decomposition. The first box contains the pre-processing step and data enhancement, while the second box contain the core of the flood detection (Ajadi et al., 2016).

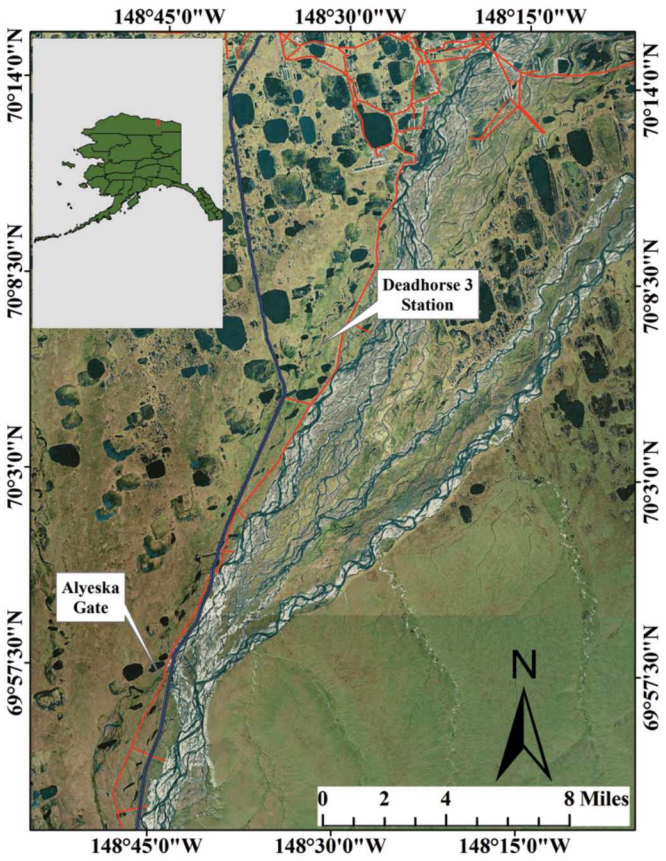

Figure 5.2. (a) Study area that encompass the path of the Sagavanirktok River. The red line is the Dalton Highway, and the blue line indicates the trans-Alaska Pipeline.

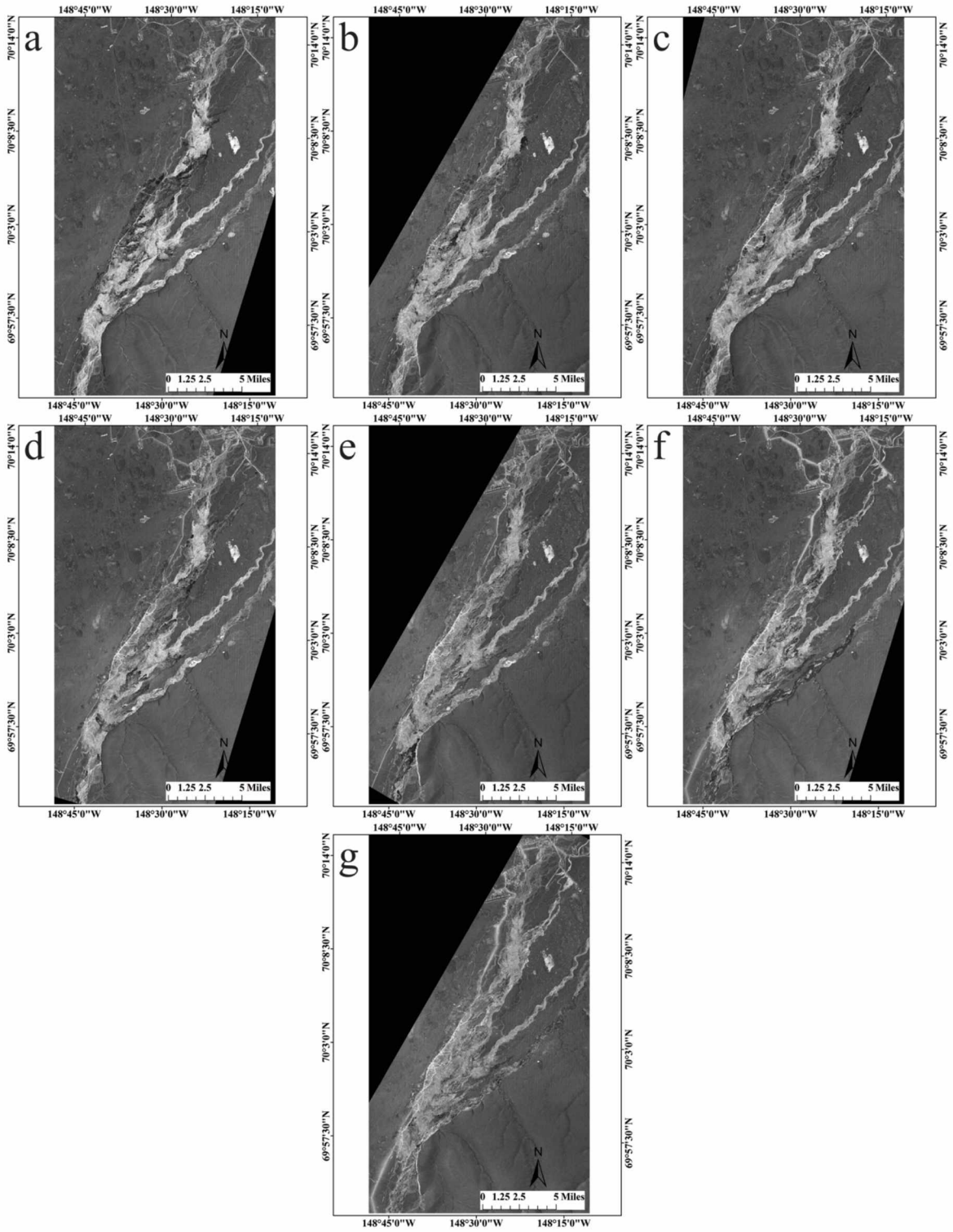

Figure 5.3. TerraSAR-X images of the study area acquired on: (a) April 13; (b) April 15; (c) April 19; (d) April 24; (e) April 26; (f) May 05; and (g) May 07 of 2015. The black regions represent areas with no data from the overpass for the defined geographical region.

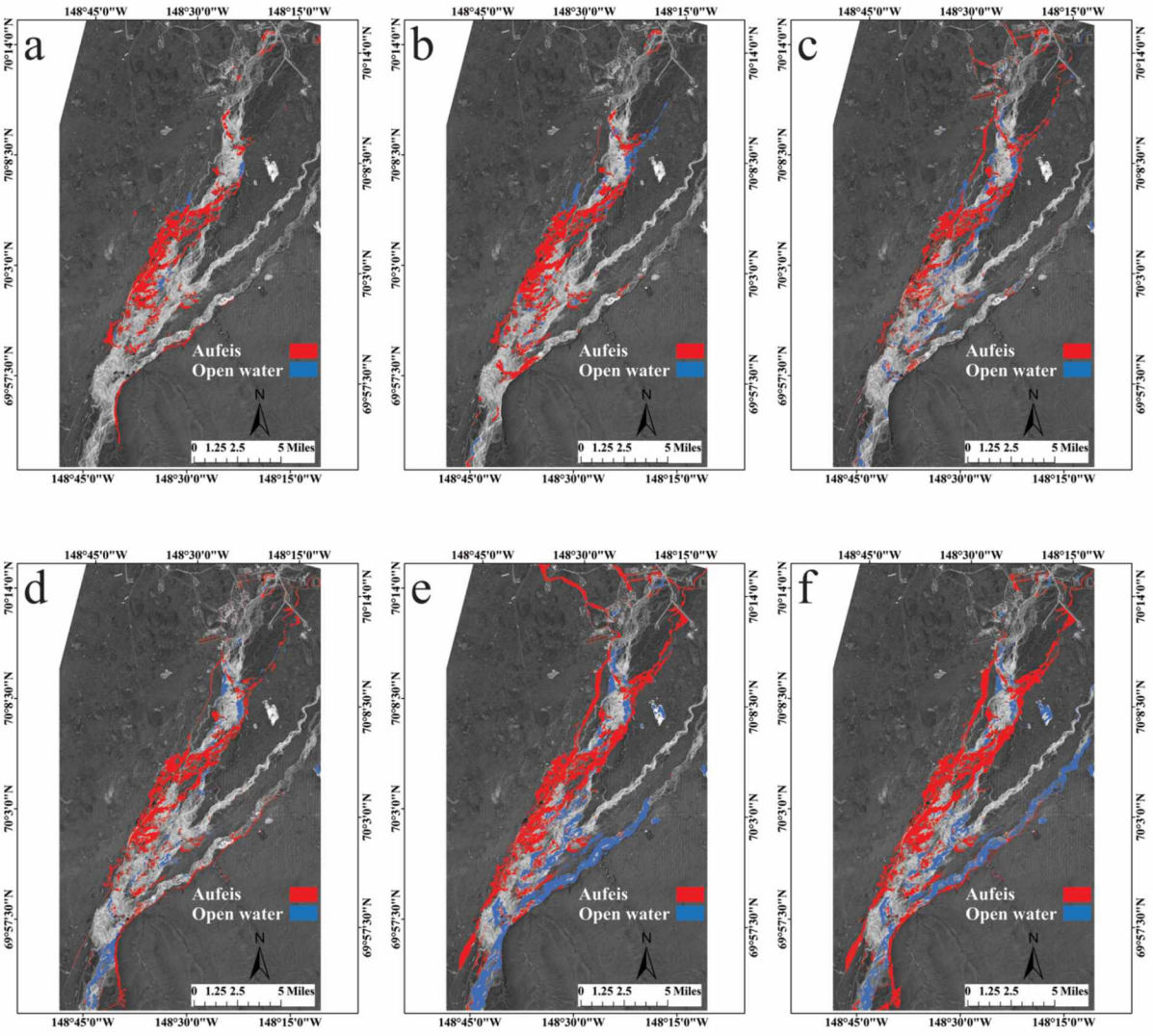

Figure 5.4. Flood detection maps after applying our modified approach to (a) observation period 1 (April 13-15); (b) observation period 2 (April 13-19); (c) observation period 3 (April 13-24); (d) observation period 4 (April 13-26); (e) observation period 5 (April 13-May 5); and (f) observation period 6 (April 13-May 7). See Table 5.2 for a description of the image pairs used for each observation. Note that observation period is the combination of pre- and post-event images used to generate a log-ratio image.

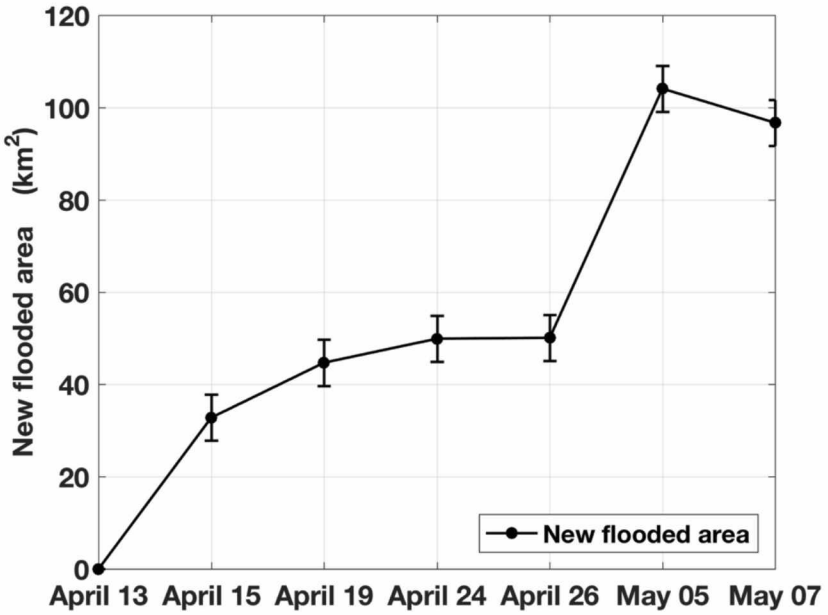

Figure 5.5. Growth in flooded area (both aufeis and open water) during observation periods 1 through 6 (Table 5.2). Error bar shows the uncertainty (±5) for each flooded area.

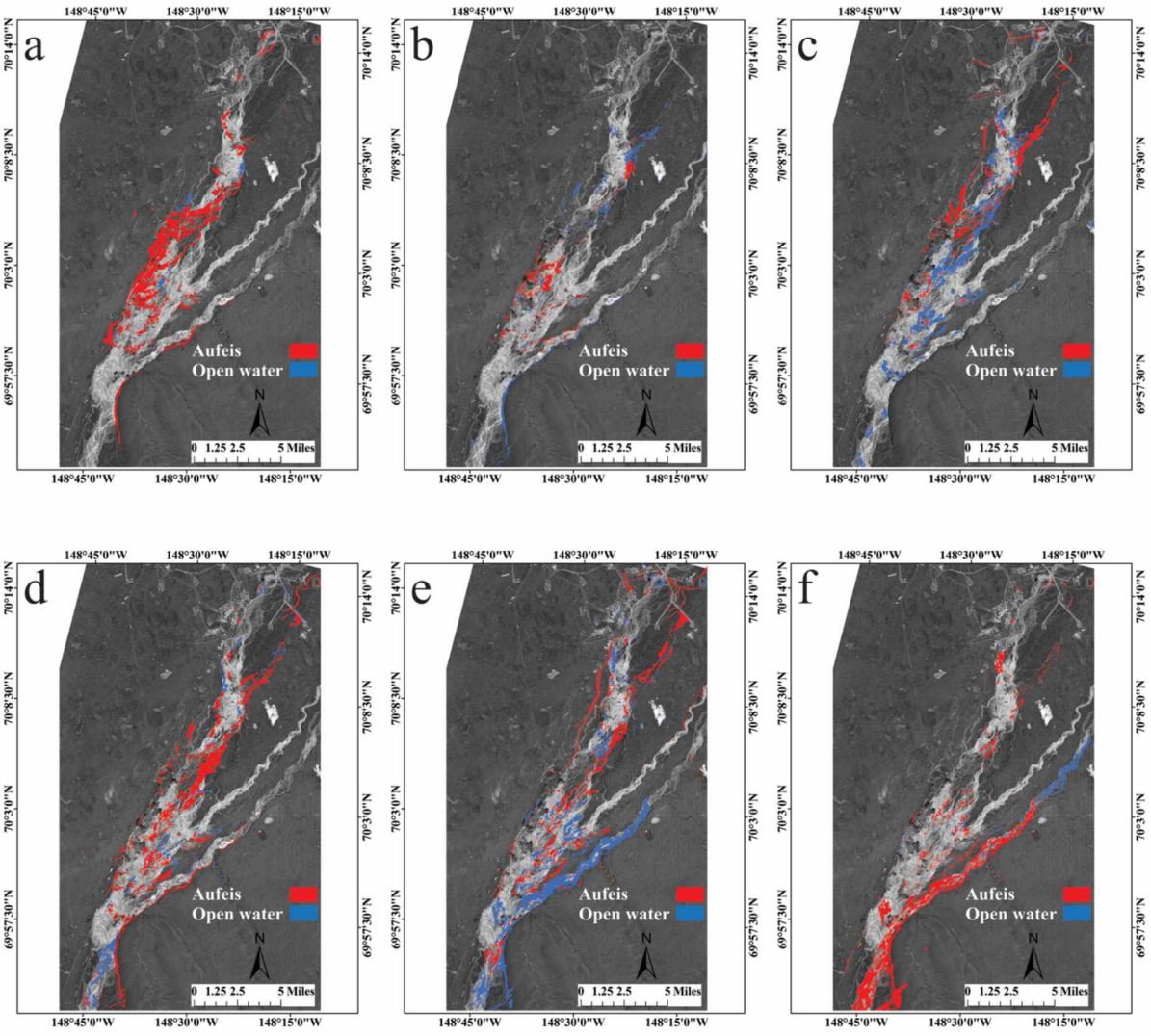

Figure 5.6. Flood detection maps after applying our modified approach to (a) observation period 7 (April 13-15); (b) observation period 8 (April 15-19); (c) observation period 9 (April 19-24); (d) observation period 10 (April 24-26); (e) observation period 11 (April 26-May 5); and (f) observation period 12 (May 5-7). See Table 5.2 for a description of the image pairs used for each observation period.

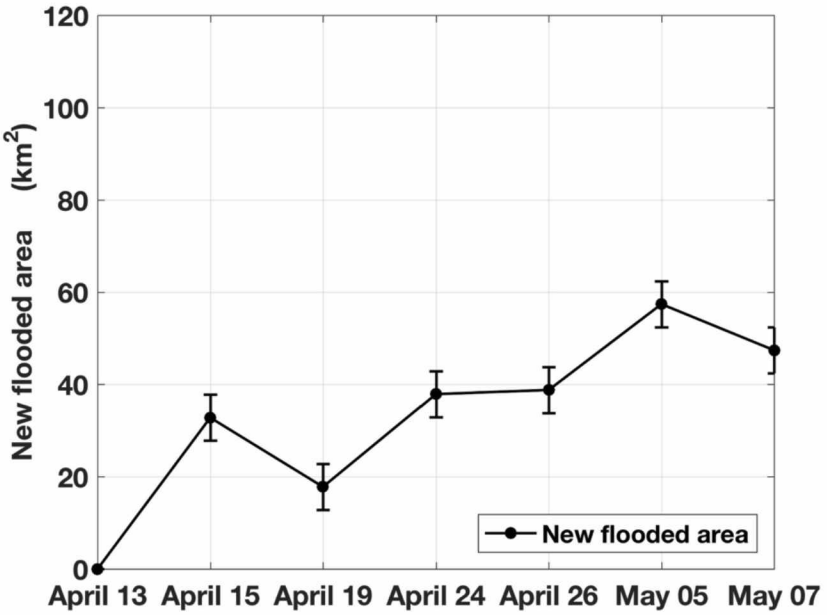

Figure 5.7. Flooded area (both aufeis and open water) covered by observation periods 7 – 12. Error bar shows the uncertainty (±5) for each flooded area.

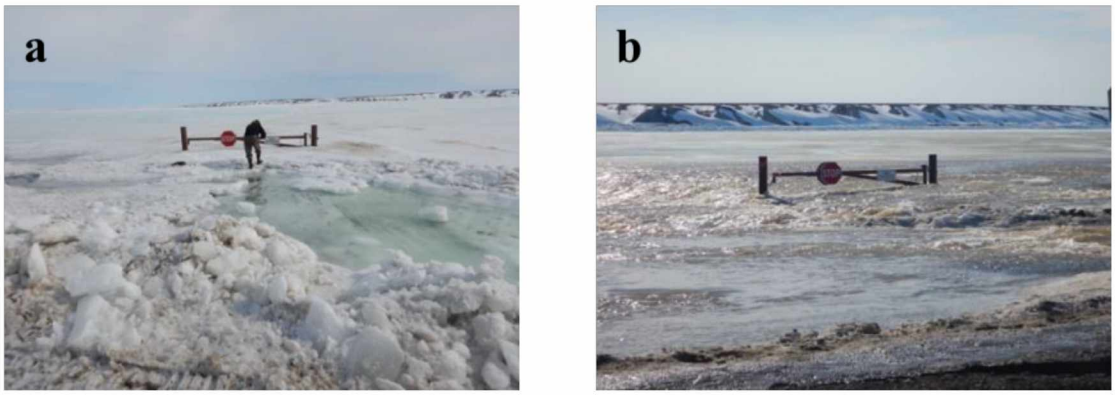

Figure 5.8. Photo taken on (a) May 15, 2015 and (b) May 17, 2015 at the Alyeska gate along the Dalton Highway. Images reprinted from (Toniolo et al., 2015). See Figure 5.2 for location.

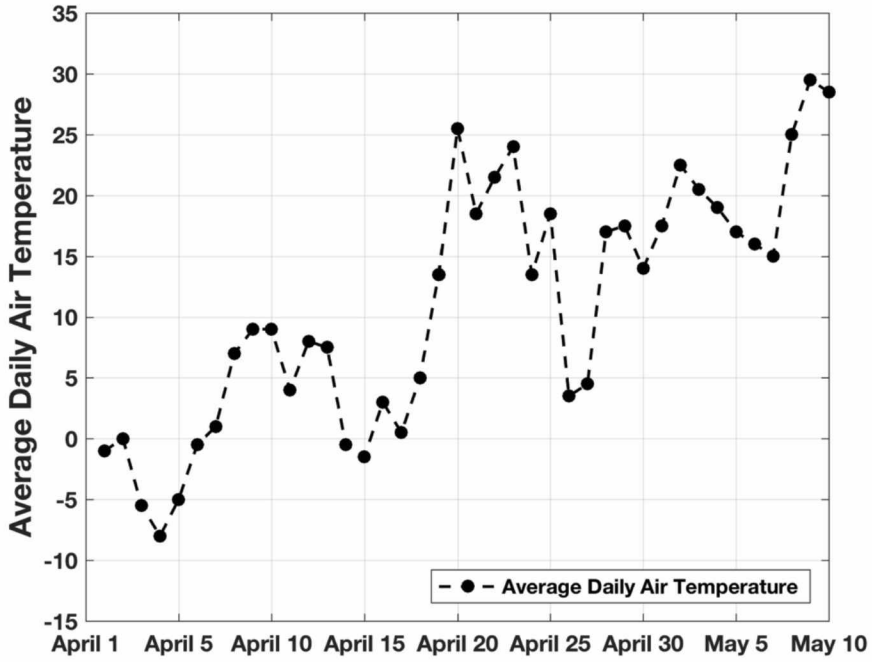

Figure 5.9. Average daily air temperature at Deadhorse 3 station from April 1 – May 10, 2015.

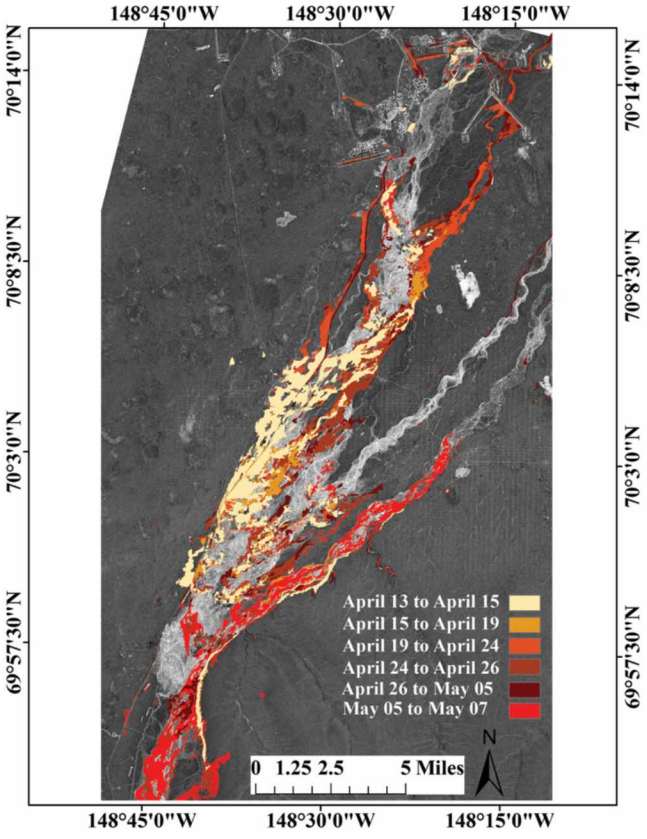

Figure 5.10. Combined visualization of aufeis distribution from early April until early May, 2015.

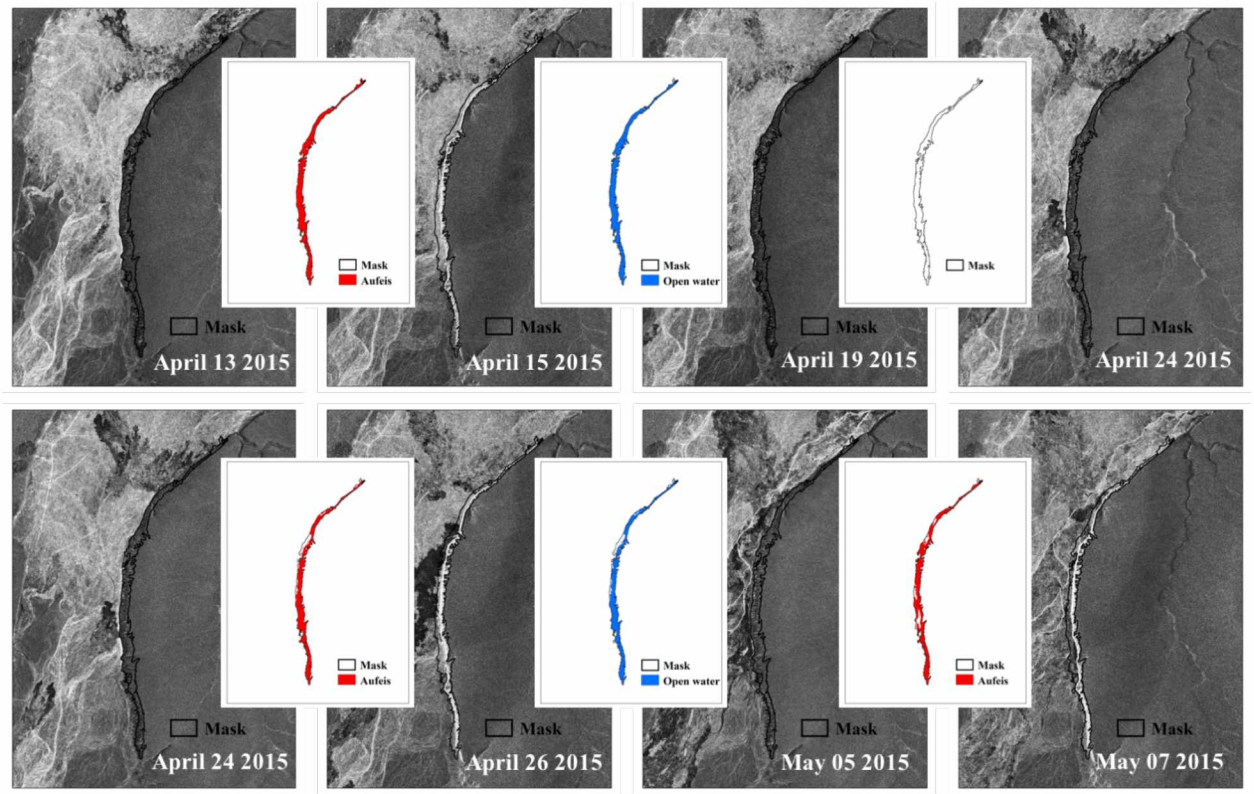

Figure 5.11. Example of a mask identifying a region that has experienced several aufeis episodes over the observed time frame.

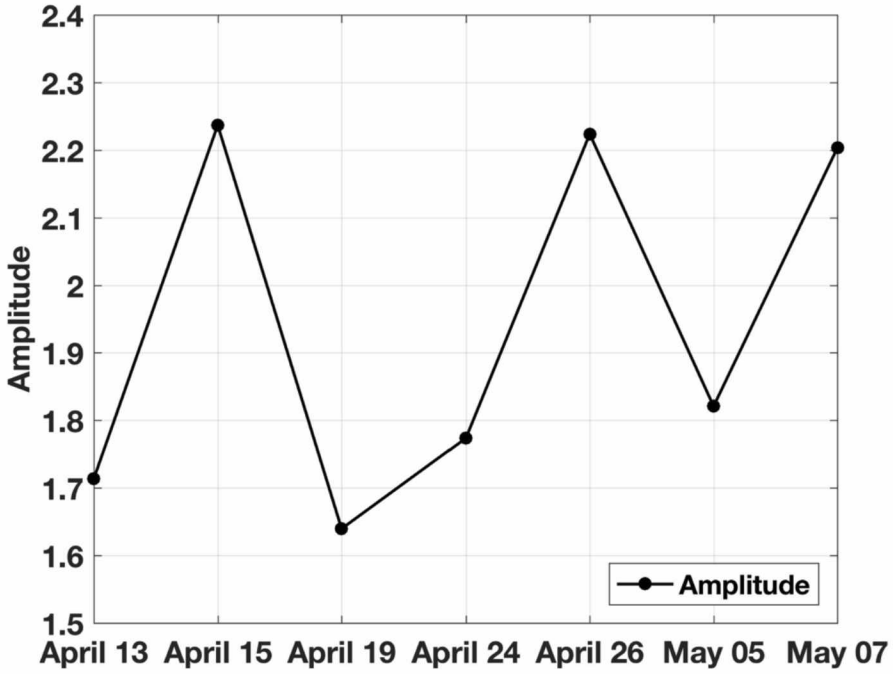

Figure 5.12. Average change in backscatter intensity as a function of time from April 13 – May 7, 2015.

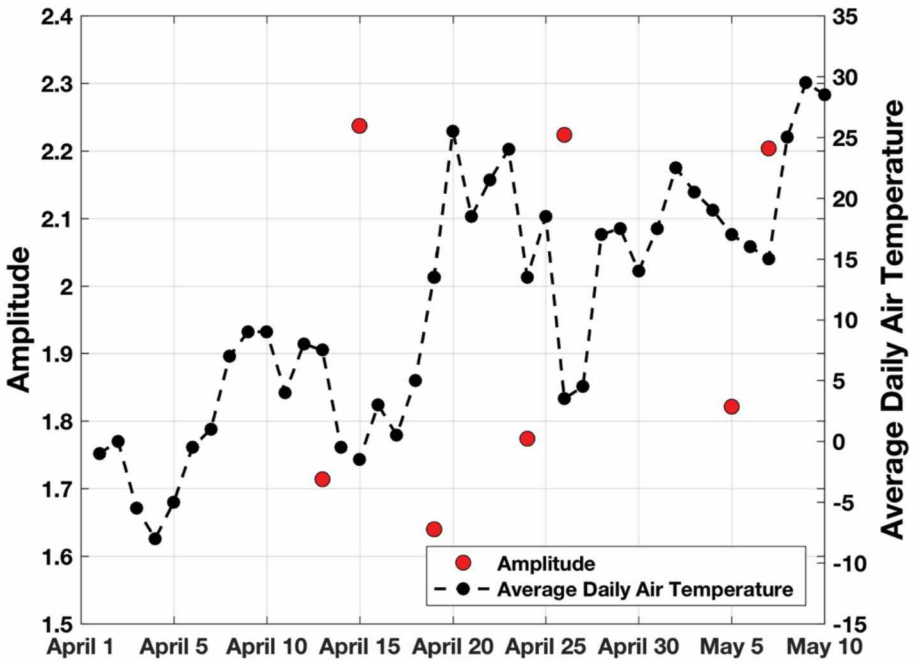

Figure 5.13. Average change in backscatter intensity and average daily air temperature as a function of time from April 1 – May 10, 2015.

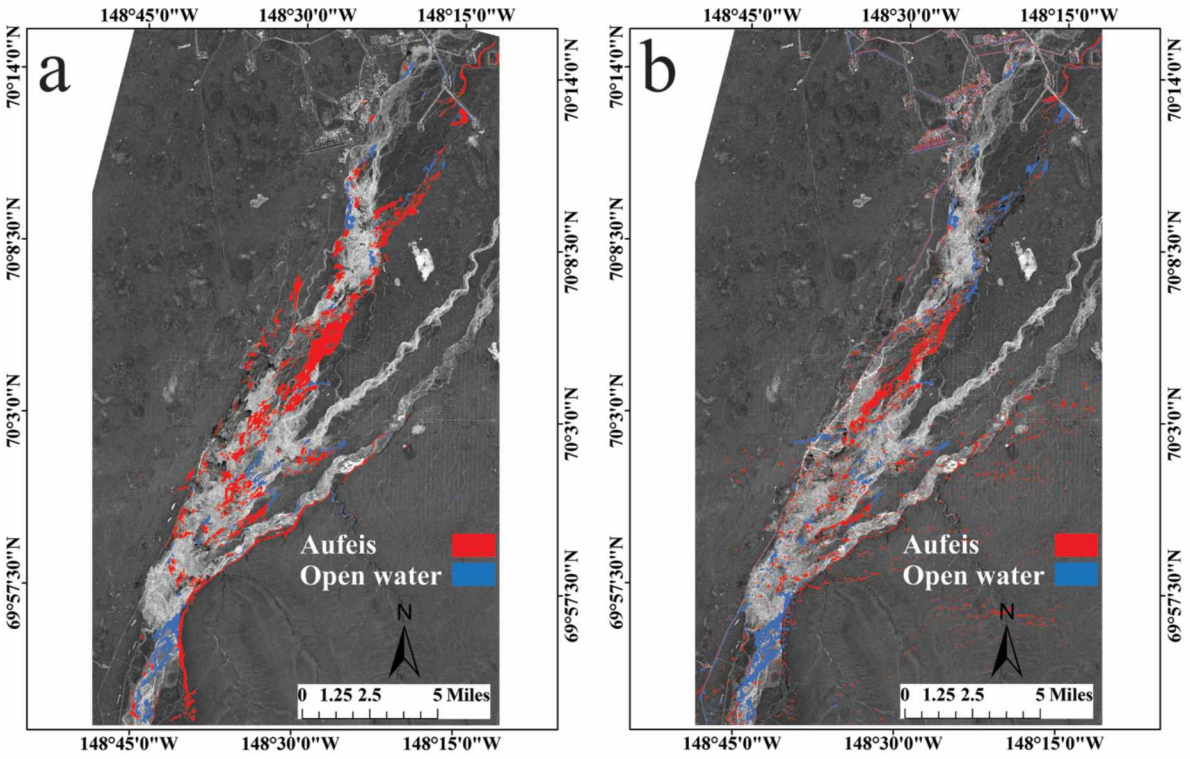

Figure 5.14. Flood maps generated from (a) TerraSAR-X imagery and (b) Landsat 8 imagery for observation period 10.

Table 5.1. Details of TerraSAR-X data acquired over the Dalton Highway and Sagavanirktok River.

Date	Flight Direction	Local Standard time	Incidence Angle	Polarization	Look Direction
April-13-2015	descending	08:42:06	35°	HH	Right
April-15-2015	descending	09:41:57	24°	HH	Left
April-19-2015	descending	08:33:32	41°	HH	Right
April-24-2015	descending	08:42:07	35°	HH	Right
April-26-2015	descending	09:41:59	24°	HH	Left
May-05-2015	descending	08:42:08	35°	HH	Right
May-07-2015	descending	09:42:01	24°	HH	Left

HH is Horizontal transmitted and Horizontal received polarization.

Table 5.2. Combination of image acquisitions used to generate the ratio images.

Pre-event Image	**Post-event Image**	**Observation #**		**Flooded Area km^2**	**Figure showing results**
April-13-2015	April-15-2015	Observation 1	Long Interval	32.8±5	Figure 5.4a
April-13-2015	April-19-2015	Observation 2		44.7±5	Figure 5.4b
April-13-2015	April-24-2015	Observation 3		49.9±5	Figure 5.4c
April-13-2015	April-26-2015	Observation 4		50.1±5	Figure 5.4d
April-13-2015	May-05-2015	Observation 5		104.1±5	Figure 5.4e
April-13-2015	May-07-2015	Observation 6		96.7±5	Figure 5.4f
April-13-2015	April-15-2015	Observation 7	Short Interval	32.8±5	Figure 5.6a
April-15-2015	April-19-2015	Observation 8		17.8±5	Figure 5.6b
April-19-2015	April-24-2015	Observation 9		37.9±5	Figure 5.6c
April-24-2015	April-26-2015	Observation 10		38.8±5	Figure 5.6d
April-26-2015	May-05-2015	Observation 11		57.4±5	Figure 5.6e
May-05-2015	May-07-2015	Observation 12		47.4±5	Figure 5.6f

Chapter 6 Conclusion and Future work

6.1. Conclusions

Recently, different organizations and governments have made the monitoring of natural and human-based disasters an important task (Mata-Lima et al., 2013). As a result, an awareness on the capability of satellite data as a tool for mapping disasters has been evolving among civil-protection and relief organizations. Over the years, spaceborne SAR sensors have shown numerous advantages, such as their ability to operate under different weather conditions and ability to cover large areas, over personnel on the ground or manned/unmanned flights to monitor disaster areas. In addition, due to the increasing number of spaceborne SAR sensors with short revisit times (e.g., Sentinel-1A and B), a vast collection of SAR data are now available for near real-time disaster detection and monitoring. Nonetheless, SAR data have remained difficult to analyze and hard to integrate into fully automatic operational services. A major obstacle in this regard is the practical difficulty of developing efficient, unsupervised change detection techniques.

Motivated by the need to improve current change detection technology, especially for SAR data applicable to disaster monitoring, this dissertation focused on the development of unsupervised change detection techniques to exploit time series of SAR datasets. The important characteristics of the developed techniques are: due to their focus on SAR amplitude information, they can be virtually applied to all SAR data; the sampling frequency of natural hazards is maximized by the inclusion of pre-processing steps such as RTC processing or Lipschitz Regularity transformation; the core of the techniques is designed to be highly adaptive and, hence, applicable to a broad range of environmental conditions or disciplines with little modification; change detection is achieved automatically with fully adaptive thresholding; and finally, through

the integration of multi-scale techniques and modern resolution-preserving filtering technology, the resolution and geometric details in a SAR image are largely preserved while the signal-to-noise ratio of change detection is drastically improved.

In Chapter 3, an automatic change detection approach was presented that is optimized for detecting changes embedded in stationary background (e.g., forest fire burn areas; progressing lava flows, etc.). The approach is efficient in classifying change signatures from pairs of SAR images. Employing radiometric terrain correction (RTC) in the proposed approach facilitates the removal of radiometric differences between SAR images acquired from different geometries. The removal of radiometric differences increases the temporal sampling of surface changes. The use of log-ratio operations resulted in effective suppression of background information, enhanced change information, enabled high detection performance, and preserved change signature details. The performance of speckle filtering was improved by the integration of modern, non-local means filtering, and two-dimensional stationary wavelet transform (2D-SWT) techniques. The non-local means algorithm provided a good alternative to traditional adaptive filters. It displayed a great ability to reduce the impact of speckle, while preserving the geometric structures in the image.

When combined with 2D-SWT, the residual noise was removed and the visibility of change in the image was greatly improved. The implementation of 2D-SWT which decomposed the image into different hierarchical levels helped to analyze and classify each pixel at different resolution levels, each characterized with a different tradeoff between spatial resolution and signal-to-noise. Furthermore, when mathematical morphology was integrated into the expectation maximization (EM) algorithm, the classification performance improved. The geometric details along the heterogeneous (border) regions were enhanced and accurately

detected when product rule fusion was employed. Quantitative and qualitative analyses of the results in Chapter 3 showed that the proposed approach gave a high overall accuracy in both homogeneous and heterogeneous areas. In addition, the computational time for this approach was shown to be low, making it a highly desirable approach for near real-time monitoring. For example, we analyzed an image of size 3584 x 5056 pixels affected by wildfire and fire scar boundaries were detected with a 99.9% accuracy in 2.5 minutes using a mackintosh MacBook pro.

In Chapter 4, we adapted the change detection approach to perform effectively when applied to scenes of continuously varying background. This modification was necessary to enable the detection of oil spills on constantly changing ocean surfaces. The Scale-space LIpschitz-based Change tracKing (SLICK) approach was developed for oil spill detection from SAR images based on multi-scale, time-frequency theory. To preserve spatial resolution, normalize the reflectivity properties of ocean water, and maximize the visibility of oil in water, the approach estimates the local regularity of images through the evaluation of Lipschitz regularity (LR). The LR technique is calculated from the progression of wavelet coefficient across scales and is well-suited for an unsupervised change detection approach. Testing the SLICK approach on simulated and actual data resulted in a very high detection rate (kappa coefficient of 0.95 and above) with minimal false positives and false negatives. In all, this approach gave a better result when compared with several published alternatives. This approach showed its effectiveness in heterogeneous SAR images where the training of features can be difficult and time consuming.

Chapter 5 introduced a time series concept into the change detection approach. Due to the increase of satellite systems with high revisit frequencies, a large amount of SAR data are available for flood mapping activities. In this Chapter, the change detection approach from

Chapter 3 was adapted to the problem of aufeis flood mapping. Using a pre-processing approach like that described in Chapter 3, curvelet filtering was added to address the changing geometric features occurring along the edges of the flooded area. Since the goal was to delineate flood areas in both heterogeneous and homogeneous areas, identifying flood edges is important. The inclusion of curvelet filtering removed noise, preserved edges, and facilitated flood area detection with high geometric precision. Applying the modified approach to TerraSAR-X data covering Sagavanirktok River flooding in northern Alaska during Spring 2015 generated several probabilistic flood maps. These maps were combined in the latter processing stages using measurement level fusion to generate final three class binary flood maps. It should be noted that this method does not assume that each class has the same prior probability. Moreover, the generation of time series flood maps gave an awareness of the complex nature of the Sagavanirktok River flooding.

These three-algorithms are well suited for operational applications because they are computationally efficient (generate change detection maps in less than 5 minutes), fully automatic, and do not require the use of any external datasets. In addition, they automatically adapt to different types of single-frequency, single-polarization SAR images.

6.2. Future work and Improvements

Even though our results from the three hazardous event types showed great potential when using the described change detection approach, in future work it would be desirable to improve the presented change detection approach such that neighboring pixels are analyzed together during classification rather than analyzing each pixel independently. Also, combination of multiple SAR sensors to increase temporal sampling should be considered. Different modality of SAR (coherence and incoherence information) should be considered as well, which in turn will

increase the accuracy of the final change detection result. In terms of flood mapping, it will be desirable to integrate flood extent estimation (Figure 6.1) with a hydraulic model (Figure 6.2).

A potential extended workflow of a future automatic flood mapping system is shown in Figure 6.1. According to this workflow, an improved change detection approach would rely on three stages. The first stage would combine posterior probability flood maps generated from advanced image processing procedures such as i) Hidden Markov Random fields (HMRF) (Zhang et al., 2001) and ii) Support vector machines (SVM) (Schölkopf and Smola, 2002) with results from iii) InSAR coherence analysis (Dellepiane et al., 2000). The HMRF approach could fully utilize the approach in Ajadi et al. (2016) as prior information and update its posterior probability using the contextual information of neighboring pixels.

In the second stage, the temporal behavior of flood phenomena would be examined. A probabilistic time-series that follows the evolution of the flooding event would be generated. Joint probabilistic flood information generated from the first stage would now be used to estimate new probabilistic flood maps using a least squares solution (Berardino et al., 2002). This approach would provide dense probabilistic flood time-series maps and increase the temporal sampling rate by using all the SAR acquisitions (e.g. TerraSAR-X and Sentinel-1). Classification maps would be generated such that, each pixel in each of the estimated probabilistic flood time-series maps is assigned to the class that maximizes the posterior conditional probability.

In the last stage, each classification map should be dilated using a region growing approach (Giustarini et al., 2013) and the slope map generated from a digital elevation model (DEM) could serve as the tolerance parameter. Finally, a decision tree classifier utilizing each of the newly

generated classification maps and an altitude map generated from a DEM could be used to remove false positives in the final flood extent time-series.

6.2.1. Integration with Hydraulic Model

While this dissertation exclusively focused on remote sensing data analysis, an integration of remote sensing data processing with geophysical models should be attempted in the future, to take advantage of the many synergies that exist between these two fields. Modern hydraulic models can provide probabilistic flood forecasts that could be integrated into the remote sensing data analysis as a statistical prior. This would improve the treatment of false alarms and lead to an overall performance improvement for remote sensing-based flood mapping techniques. At the same time, remote sensing data analysis can also provide valuable boundary condition data for assimilation into hydraulic models. The following thoughts summarize concepts that can be employed to further data-model-integration:

As hydraulic models utilize and produce estimates of water volume, flood maps derived from remote sensing data have to be converted to volume information to facilitate data-model integration. Hence, flood depth maps need to be estimated for every initial flood extent layer by intersecting flood extent maps with an underlying DEM. Each flood extent boundary pixel would be converted into a point shapefile and a pixel value should be attached to each point shapefile using its location to extract the corresponding pixel value from a DEM. Using the network of point shapefiles, a Triangulated Irregular Network (TIN) should be created. Exploiting TIN interpolation, a flood water surface should be generated. Horizontal flood water surface should be assumed and flood depth representing water level estimation can then be calculated by subtracting a DEM from the flood water surface.

The estimated water level should be used for hydraulic model calibration (improving the fit between model prediction and observations). Since flow direction is mainly parallel to the channel, the two-dimensional (2-D) flow related to riverbanks overtopping should be approximated with a one-dimensional (1-D) representation. In order to have an up-/downstream relationship, evenly distributed cross sections along the estimated water level should be generated from the upstream section and ending at the downstream section. To reduce estimation uncertainty, all the water level estimate at the left and right cross sections of the flood extent boundary should be hydraulically constrained. The constraint should be enforced such that, maximum water level estimate decreases downstream, while minimum water level estimate increases upstream. The Hec-RAS (Brunner, 2004) hydraulic model which requires knowledge of the boundary conditions and manning friction coefficients should be used for data-model calibration. The downstream boundary condition should be produced from the relationship between estimated water level and discharge (rating curve). The parameters of the manning friction coefficients (one for the channel bed and one for the floodplain) should be randomly generated by employing the Monte Carlo simulations (Schumann et al., 2007). To facilitate data-model calibration, the model output of every iteration should be compared with water level estimate using the root mean square error (rmse) and the model output with the lowest rmse should be selected.

6.3. References

Ajadi, O. A., Meyer, F. J., and Webley, P. W., 2016, Change Detection in Synthetic Aperture Radar Images Using a Multiscale-Driven Approach: Remote Sensing, v. 8, no. 6, p. 482.

Berardino, P., Fornaro, G., Lanari, R., and Sansosti, E., 2002, A new algorithm for surface deformation monitoring based on small baseline differential SAR interferograms: IEEE Transactions on Geoscience and Remote Sensing, v. 40, no. 11, p. 2375-2383.

Brunner, G., 2004, Theoretical basis for one-dimensional flow calculations: HEC-RAS, river analysis system, hydraulic reference manual, version 3.1, v. 2.

Dellepiane, S., Bo, G., Monni, S., and Buck, C., 2000, SAR images and interferometric coherence for flood monitoring, *in* Proceedings Geoscience and Remote Sensing Symposium, IGARSS 2000. IEEE 2000 International, v. 6, p. 2608-2610.

Giustarini, L., Hostache, R., Matgen, P., Schumann, G. J.-P., Bates, P. D., and Mason, D. C., 2013, A change detection approach to flood mapping in urban areas using TerraSAR-X: IEEE transactions on Geoscience and Remote Sensing, v. 51, no. 4, p. 2417-2430.

Mata-Lima, H., Alvino-Borba, A., Pinheiro, A., Mata-Lima, A., and Almeida, J. A., 2013, Impacts of natural disasters on environmental and socio-economic systems: what makes the difference?: Ambiente & Sociedade, v. 16, no. 3, p. 45-64.

Schölkopf, B., and Smola, A. J., 2002, Learning with kernels: support vector machines, regularization, optimization, and beyond, MIT press.

Schumann, G., Matgen, P., Hoffmann, L., Hostache, R., Pappenberger, F., and Pfister, L., 2007, Deriving distributed roughness values from satellite radar data for flood inundation modelling: Journal of Hydrology, v. 344, no. 1, p. 96-111.

Zhang, Y., Brady, M., and Smith, S., 2001, Segmentation of brain MR images through a hidden Markov random field model and the expectation-maximization algorithm: IEEE Transactions on Medical Imaging, v. 20, no. 1, p. 45-57.

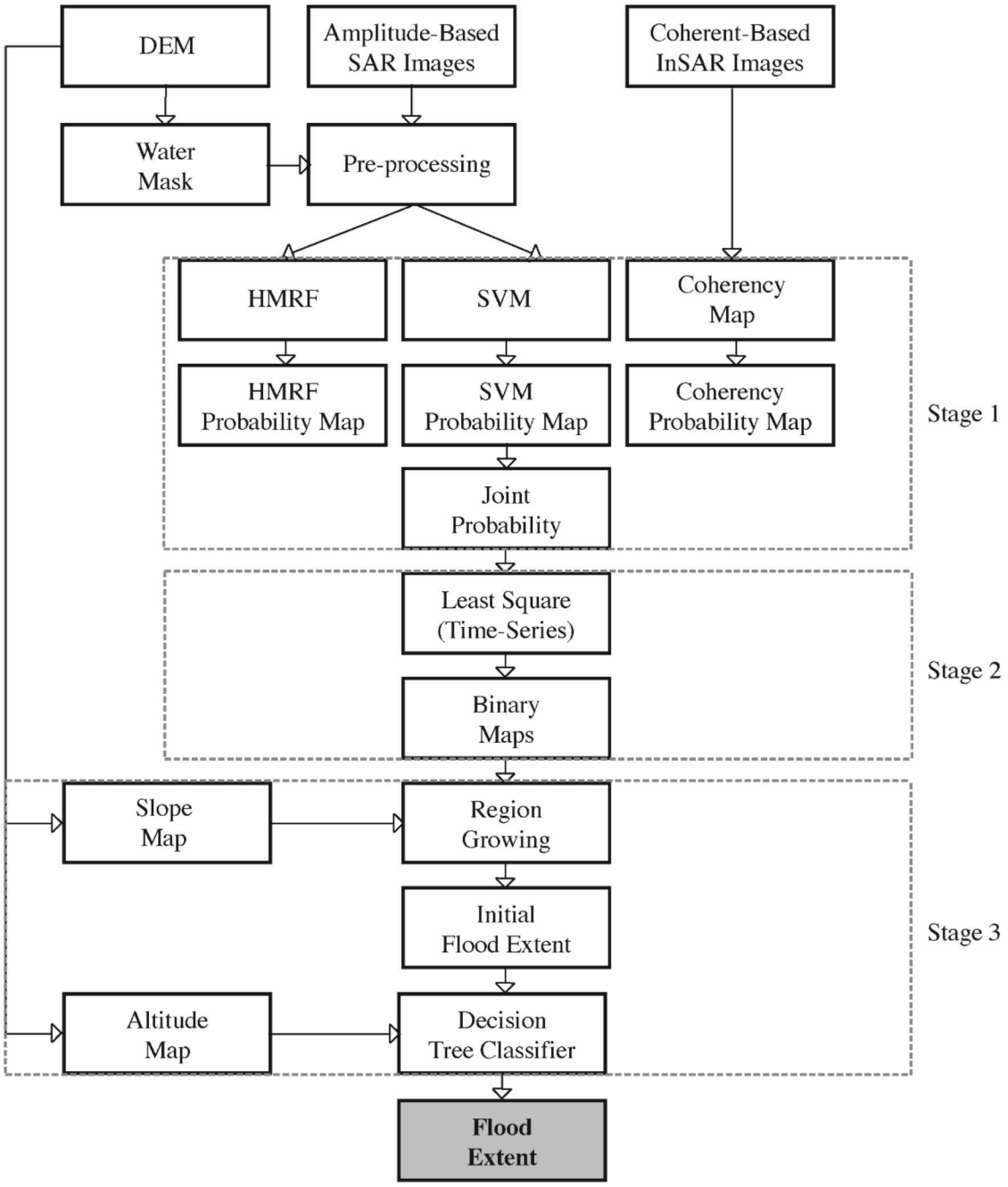

Figure 6.1. Proposed approach of future work for flood extent estimation. HMRF stands for hidden markov random field and SVM stands for support vector machine.

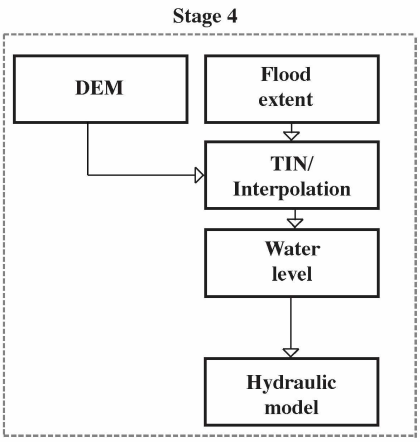

Figure 6.2. Integration of water level with hydraulic model. TIN refers to as Triangulated Irregular Network.